NONLINEAR TIME-SERIES ANALYSIS OF IN VITRO AND HUMAN ELECTROENCEPHALOGRAPHIC RECORDINGS FOR SEIZURE ANTICIPATION AND IN VITRO SEIZURE CONTROL

by

Houman Khosravani

A thesis submitted in conformity with the requirements
for the degree of Master of Science
Graduate Department of Physiology
University of Toronto

Nonlinear Time-series Analysis of *in vitro* and Human Electroencephalographic Recordings for Seizure Anticipation and *in vitro* Seizure Control

Houman Khosravani

Master of Science · 2002 ·
Department of Physiology,
University of Toronto, Canada

· ABSTRACT ·

Nonlinear time-series analyses allows for characterization of the behaviour of complex systems, both physical and biological. We present a simple method, Recursive Peak Time (RPT) analysis, based on peak detection, recursive plotting, and nonlinear mapping for time-series processing of epileptiform electrophysiological recordings. We applied this method to epileptiform extracellular fields (*in vitro*) and human depth-electrode electroencephalographic recordings. RPT analysis revealed anticipatory signal changes 44 s and 29 s (on average) prior to seizures recorded from extracellular fields and human electroencephalographic respectively. Transient and intermittent pathological hypersynchronous activity of neuronal populations characterizes epileptic seizures. Using an *in vitro* model of recurrent spontaneous seizures and nonlinear time-series analyses, using peak information from RPT, we described the dynamical regimes present leading to seizure-like activity as transient stabilization of meta-stable states. Transition to seizure was averted using brief low-frequency (0.5 Hz) periodic perturbations, which altered the system's dynamics by forcing another, non-seizure, meta-stable state.

Dedications & Acknowledgments

(in no particular order…only in disorder!)

"If our small minds, for some convenience, divide...this universe into parts - physics, biology, geology, astronomy, psychology, and so on - remember that nature does not know it!" - RPF

"Everyone should at one time in their life look through a telescope and also a microscope" - HK

Glossary

NTSA	Nonlinear Time-series analysis.
SLE	Seizure-like Events, activity as recorded from rat brain hippocampal slices, perfused with low [Mg^{+2}] artificial cerebrospinal fluid, exhibiting recurrent, spontaneous seizure-like activity – this is an in vitro model of human status epilepticus.
Seizure Prediction	The ability to precisely forecast the time of an impending seizure.
Seizure Anticipation	The ability to identify a time window in the future (or an approximate time within that window), where there exists a high probability of seizure occurrence.
Dynamical	Refers to the state changes of a system over time.
Deterministic System	Future states of the system can be exactly predicted using the initial conditions and mathematical rules (i.e. equations) for certain control parameters. However, alteration of parameters can result in unpredictable, even chaotic behaviour, which are still deterministic (bounded in state-space). One of the great breakthroughs in dynamical systems theory was the demonstration that simple deterministic systems can exhibit complex behaviour (e.g. Lorenz system).

Stochastic System	A system for which future states can be determined using probabilistic methods if ones knows the initial conditions and the equations that govern the system's behaviour.
Nonlinear System	A system in which the superposition principle does not apply. States change over time in accordance with nonlinear differential or difference equations that involve one or more variables. These systems under certain conditions, may exhibit behaviour such as: sensitive dependence on initial conditions, self-organizing behaviour, frequency entrainment, and intermittency.
Dissipative System	A system for which the state-space volume is contracted, such as when in the vicinity of an attractor (including a chaotic attractor). In these systems energy is not conserved, and in general, time-independent Hamiltonians do not exist. Whenever there exists dissipation in a system, equations of motion change under time reversal – the evolution of the system is not reversible. An example of a dissipative system is a damped oscillator; dissipative systems can have significantly more complex evolutionary regimes than simple decay, for example in cases where there exists dampening in tandem with mechanisms maintaining motion.

Chaos	Dynamical state of a deterministic nonlinear system that looks stochastic. Characterized by continuous broadband Fourier spectrum. Possible only in a three-or-more dimensional nonlinear system of differential equations or a one-or-more dimensional nonlinear discrete map (e.g. the logistic map – a nonlinear difference equation). Mathematical definition: at least one positive Lyapunov exponent exists.
State-space	Representation of possible states for a system in a geometrical space (also called phase-space), where evolution of these states over time gives rise to a trajectory within that space. Note that state-space is not limited to three-dimensions but to the number of state-variables.
Reconstructed State-space	The space, constructed solely from measurements (experimental observables) that serves as a proxy for the full multivariate dynamical system state-space.
Attractors	Regions within state-space to where states of the system evolve and remain confined until the structure of the system itself changes (thus reflected in the structure of the state-space) or when an external perturbation is delivered.
Dimension	A numerical value related to the number of "axes" required to construct the state-space (embedding dimension) or related to the number of variables required to span an attractor within the state-space (dimension of the attractor). When dimension value is non-integer, it is referred to as "fractal dimension".
Trajectory	The path that a signal vector (of implicit space dimension) follows through state-space.

Lyapunov Exponent	A numerical value that describes the average rate at which the trajectories of adjacent states in state-space diverge or converge over time.
Intermittency	The tendency for a given pattern of behaviour (state) to come and go over time. A characteristic property of nonlinear systems without the requirement of external perturbations. Typically, the phenomenon of intermittency refers to spontaneous transitions from laminar (periodic) epochs to chaotic ones and back.
Stationarity	Used here in the context of stationary processes or stationarity in signals. In its weakest form requires that all parameters of the studied system relevant for dynamics to be fixed and constant during the measurement period (and the same should it be reproduced). If the process under observation is a probabilistic one, it will be characterized by probability distributions for the variables involved. For a stationary process, these probabilities may not depend on time.
Return Map	A visible plot in either two or three dimensions where values in a column of data (one-dimensional data set) are plotted in a recursive manner, where one value is plotted against a subsequent value in the record with some integer delay (t). For a delay of $t = 1$, each value is plotted against the next. For larger delays, every t^{th} value is plotted recursively.

Contents

List of Figures

List of Tables

I Introduction

1.1 Motivation and Relevance

Epilepsy is prevalent in up to ~1% of the population and about 25% of epileptics suffer from seizures that are intractable to presently available anticonvulsants. To date all treatments are subject to major side effects, risks and/or have limited efficacy (Guberman and Bruni, 1999). Current methods for seizure treatment include: (1) Anticonvulsants, of which there are over a dozen in clinical use. All have significant side effects, sometimes fatal, and often impair the quality of life of the patient. (2) The Ketogenic Diet can significantly ameliorate intractable seizures in some paediatric cases, but it is not very palatable and is difficult to administer. (3) Surgical techniques can be successful in up to 90% of carefully selected patients. Unfortunately the selection procedure excludes many patients with intractable seizures. Surgery is a major invasive procedure with serious risk potential and poor efficacy for extra-temporal intractable seizures. (4) Vagal Stimulation is a relatively new technique involving indirect stimulation of the brain and is reported to result in a decrease of seizures in approximately 1/3 of patients. Its mechanism of action is unknown and can potentially have detrimental long-term effects that have not been studied. (5) Deep Brain Stimulation (DBS) techniques, such as Sub-thalamic nucleus (STN) stimulation, is a recent approach for controlling intractable seizures (Benabid *et al.*, 2000) with limited success to date. This is due to a lack of clinical and scientific understanding with regards to what stimulation paradigms and locations are most effective. In most cases the stimulation is repetitive and stimulators are chronically 'on' with no 'intelligent' means of modulating their instantaneous activation. (6) Transcranial Magnetic Stimulation (TMS) is a non-invasive method that acts on gross anatomical regions of the brain. In epileptic patients it has been used to measure seizure activity by actually lowering the threshold for activation (Hallett, 2000). Some therapeutic benefit has been reported for

low frequency repetitive TMS (Tergan *et al.*, 1999). However such findings are highly experimental and are not well established in the literature.

The defining characteristics of seizures are pathological hypersynchronous activation of brain regions that interferes with normal function. This activity can be localized or can spread to become generalized. Seizures can have several routes of onset and many different mechanisms of generation (McNamara, 1994 & 1999, Iasemidis and Sackellares, 1996). There can be multiple foci for the generation of seizures, both at the gross anatomical and at the cellular/neuronal population levels. The dynamics of how epileptogenesis arises from local neuronal populations or circuits and anatomically spreads to the point of being a clinically relevant seizure event is not known. These mechanistic scenarios set up an arena for complex interactions between neuronal populations, both within and between local neuronal circuits, allowing for the observed diversity in clinical seizure states. Furthermore, neuronal systems are known to respond with sensitivity to slight stimuli and environmental changes, illustrating their nonlinear properties. Based on the characterized nonlinear properties of neuronal populations and the clinical presentation of epileptic phenomenon, epilepsy is regarded as a "dynamic disease" (Da Silva and Pijn, 1999), where a pathological loss of complexity in the brain gives rise to abnormal synchronous activity that comprises a seizure. It should be noted that characteristics of a seizure are distributed over space and time. To date, the best way of analyzing these forms of complex and diverse activity is by nonlinear dynamical systems analyses (Iasemidis and Sackellares, 1996), using electrical recordings from relevant anatomical structures prone to epileptogenesis.

Intelligent data analysis often requires one to extract meaningful conclusions about a complex system using time-series measurements from a single sensor. Dynamical systems analyses are a set of tools applied in the neurosciences, for the characterization of electrical signals from neuronal elements and/or populations. Nonlinear dynamics provides a framework in which complex systems may be analyzed for fundamental properties relatable to state transitions. This framework exploits a system's behavioural characteristics to gain an understanding of the system so as to subtly manipulate it. A possible important attribute of nonlinear complex systems is their sensitive dependence on initial conditions. In other words, alterations or

perturbations originating from within or when delivered from an external source to a nonlinear system (i.e. the brain), give rise to responses (effects) that can be extremely potent and at times much greater in magnitude than the initial (cause) perturbation. Thus, using nonlinear dynamics as a tool to study the brain at various levels is a natural extension of the very workings of the brain that is intrinsically nonlinear (both at neuronal and population levels) and highly diverse in its modes of activity. It is precisely this nonlinear property of neuronal systems that allows for the use of precise small perturbations (i.e. minimal stimulation) as a method to control the behaviour of the system (Bergé *et al.*, 1984; Shinbrot *et al.*, 1993; Kantz & Schreiber, 1997), including the prevention of seizure activity.

Neuronal population activity has been investigated using nonlinear techniques, for both *in vivo* and *in vitro* scenarios. In the context of epilepsy, there have been many studies that have used nonlinear techniques, mostly studies of human EEG recordings (Babloyantz and Destexhe, 1986; Pijn *et al.*, 1991 & 1997, Elger and Lehnertz, 1998; Martinerie *et al.*, 1998), with recent work conducted on brain slice preparations (Schiff, 1994). Currently, it is widely accepted that seizures are characterized by a pathogenic synchronization of neuronal populations based on some cause(s).

1.2 Research Aims & Thesis Outline

1.2.1 Research Objectives

1. To develop a quantitative methodology that is capable of identifying neuronal population events, in the form of peaks, within recordings made from extracellular fields and EEG (electroencephalography from intracranial electrodes analogous to extracellular fields). The aim here is to develop a method based on a set of criteria for peak detection that are data dependent, thereby allowing for optimization of detection parameters to the data.

2. To evaluate the use of nonlinear time-series analyses techniques, specifically those dealing with return maps generated from inter-peak intervals, for characterizing, from a dynamics perspective, transitions between the pre-ictal (before seizure) and ictal (seizure) epochs.

3. Based on knowledge gained from dynamical analysis of *in vitro* seizure-like events (SLEs), a heuristic investigation of the efficacy of different stimulation paradigms will be performed with rudimentary considerations of both spatial and temporal aspects of single-site stimulation (i.e. perturbation). Specifically, to test whether stimulation could force the system into an alternate state, similar to the inter-ictal regime of activity, thereby averting the seizure state.

1.2.2 Thesis Outline & Summary

This thesis can essentially be categorized in two parts. Below is a description of these two themes with a brief summary of each:

1. *Development of the Recursive Peak Time (RPT) analysis technique for peak detection and visualization of seizure activity based on return maps of interpeak-intervals. Use of the RPT method for the visualization and analysis of in vitro (low $[Mg^{+2}]$ recurrent spontaneous seizures) and intracranial EEG (human epileptic patients) seizure recordings.*

<u>Brief Summary</u>

We present a simple method, Recursive Peak Time (RPT) analysis, based on peak detection, recursive plotting, and nonlinear mapping for time-series processing of electrophysiological recordings. We demonstrate RPT as a tool for visualizing and quantifying electrographic signal changes that occur prior to electrographic seizure onset. Visualization techniques utilize a simple subset of state-space relations founded in nonlinear dynamical theory. RPT analysis of slice and EEG recordings revealed common and characteristic temporal trends that were used to anticipate

seizures by ~ 44 s (n = 27 seizures, 8 hippocampal slices) and ~ 29 s (n = 20 seizures, 2 patients) respectively. Simplicity and potential for implementation into a real-time monitoring system make this form of time-series visualization and analysis attractive as a diagnostic tool complementing other available methodologies.

2. *Characterization of transitions between pre-ictal and ictal states using nonlinear systems theory, in the low [Mg^{+2}] recurrent spontaneous seizure model (in vitro). Experimentally deducing the effect of single-site pacing stimulation on altering the spontaneous activity by changing initial conditions prior to seizure state.*

<u>Brief Summary</u>

The sudden and transient hypersynchrony of neuronal firing that characterizes epileptic seizures can be considered as the transitory stabilization of metastable states present within the dynamical repertoire of a neuronal network. Using an *in vitro* model of recurrent spontaneous seizures in the rat horizontal hippocampal slice preparation, we present an approach to characterize the dynamics of the transition to seizure, and to use this information to control the activity and avoid the occurrence of seizure-like. The transition from the interictal activity (between seizures) to the seizure-like event is aborted by brief (20-50 seconds) low-frequency (0.5 Hz) periodic forcing perturbations, applied via an extracellular stimulating electrode to the mossy fibres, the axons of the dentate neurons that synapse onto the CA3 pyramidal cells. This perturbation results in the stabilization of an interictal-like low-frequency firing pattern in the hippocampal slice. The results derived from this work shed light on the dynamics of the transition to seizure and will further the development of algorithms that can be used in automated devices to stop seizure occurrence.

1.3 Background

1.3.1 Electrophysiological Time-series Analysis: Linear, Nonlinear, and RPT

Time-series analysis of electrophysiological signals is a useful tool for investigating epileptiform activity (Kantz & Schreiber, 1997; Miller, 2000). The temporal characteristics of signals, especially those recorded from activated neuronal populations, are important for the understanding of information processing mechanisms in the nervous system. Paroxysmal, hyperexcitable, and hypersynchronous activation of neuronal populations give rise to seizures, which have complex presentations and numerous routes of onset (McNamara, 1994 and 1999, Iasemidis and Sackellares, 1996). Relating the features observed in electrophysiological recordings (e.g. slow and sharp waves) to underlying system dynamics relevant to seizure generation is an active and controversial area of research. A seizure in the context of an epileptic disorder can be categorized into three broad stages of manifestation: (1) the preseizure or pre-ictal period where electrographic activity patterns are altered from normal and may contain information about a forthcoming seizure (Litt & Lehnertz, 2002). (2) The seizure or ictal stage, typically characterized by large-amplitude, rhythmic electrographic discharges (initially small amplitude, high frequency in humans when recording from depth electrodes) (3) The interictal period, which includes the post-ictal state, is the epoch between two seizures. During this stage electrographic activity returns to 'normal' with interictal markers of an epileptic brain (e.g. spikes and sharp waves).

Recordings such as extracellular fields from *in vitro* preparations and EEG (both scalp and intracranial), measure ensemble activity and are suitable for assessing neuronal activity at the population level (Faber and Korn, 1989; Steriade, 2001). Time-series analysis has been used to examine electrographic changes with particular emphasis on characterizing the transition to seizure (Gotman, 1999). Computer-aided signal analysis has been applied, mostly to EEG, for seizure detection (Gotman, 1999), seizure anticipation (Elger and Lehnertz, 1998; Litt *et al.*, 2001; Martinerie *et al.*, 1998; Babloyantz and Destexhe, 1986; Iasemidis and Sackellares, 1996; Pijn *et al.*, 1997), and

also for dynamical characterization of *in vitro* seizure models (Aitken *et al.*, 1995; Lian *et al.*, 2001; Schiff *et al.*, 1994), see Table 1.1.

Early algorithms for EEG analysis were seizure detectors (Gotman, 1982; Gotman, 1990), based on pattern recognition that identified seizure onset at several levels of confidence (Qu and Gotman, 1997). These methods were viewed as major advancements in automated detection techniques for epilepsy monitoring purposes (Pauri *et al.*, 1992). An approach developed by Osorio *et al.* (1998) uses combination of wavelet and linear filters to detect the clinical onset of seizures with minimal latency, zero false-positives and false-negatives.

Other currently available methods include the use of Artificial Neural Networks (ANNs) that are good for pattern recognition with an excellent capacity for generalization towards different signal types and characteristics (Garbor *et al.*, 1996; Webber *et al.*, 1996).

Reference	Principle Approach & Data Type	L	N	Anticipation
Casdagli et al., 1997	Correlation integral (sum), intracranial and subdual EEG		*	< 1 min.
Gabor et al., 1996	Self-organizing map (SOM) and Artificial Neural Network (ANN), pattern recognition, surface EEG	*		~ 0, seizure detection
Gotman , 1982	Decomposition of the EEG into elementary waves, surface and intracranial EEG	*		~ 0, seizure detection
Iasemidis et al., 1990	Lyapunov exponents, subdural EEG		*	~ 10 min.
Le Van Queyen et al., 2001	State-space embedding similarity, running comparison with non-seizure reference window, intracranial EEG		*	~ 5 min.
Lehnertz & Elger, 1998	Correlation dimension, human intracranial EEG		*	~ 5 min.
Martinerie et al., 1998	Modified version of correlation dimension, human intracranial EEG		*	2-6 min.
Moser et al., 1999	Lyapunov exponents, EEG		*	~ 5 min.
Osorio et al., 1998	Wavelet signal decomposition, intracranial EEG	*		~ 0, seizure detection
Petrosian et al., 2000	Wavelet signal decomposition and recurrent neural networks (RNN), intracranial and surface EEG		*	~ 1 min.

Table 1.1. A subset of studies conducted relevant to seizure detection and anticipation, mostly for EEG. These studies range from ~1 to 10 min. of seizure anticipation time. Of particular interest are the group of studies using nonlinear (N) analyses. Overall, note their significantly better performance as compared to linear (L) studies of similar magnitude. It is important to note that within each class of analysis (e.g. nonlinear), particular algorithms and methods have their own biases, shortcomings, computational burden, and practical statistical significance based on sample size. The cumulative effect of these factors can only be appreciated when the referenced studies are closely examined and contrasted. There is a balance between specificity and sensitivity that becomes relevant when comparing the efficiency and practicability of methodologies.

In general, there are two classes of time-series analyses: (1) Linear methods that interpret structure in the data by characterizing the dominant frequencies (e.g. Fourier spectral techniques) and linear temporal spectral trends (e.g. auto/cross correlation and standard coherence). These techniques, albeit extremely useful, are not entirely adequate for measurements made from complex biological systems, for they do not have the capacity to address nonlinear relations within datasets (Kantz & Schreiber, 1997). Application of linear methods to signals generated by nonlinear systems may result in spurious conclusions, such as random (noise-like) appearance of time-series when indeed determinism is present, see Fig. 1.1, (Kugiumtzis *et al.,* 1994 ;Vandenhouten *et al.,* 2000) (2) Nonlinear Time-Series Analyses (NTSAs) uncover both linear and nonlinear trends in data by first re-constructing the state-space of the system from the measurements and then characterizing system behaviour in the context of stable/unstable states (topographic-like description) and state-space invariants, such as Lyapunov exponents. This geometric-based approach describes a system's behaviour from a macroscopic or global perspective where transitions between states in a system, as governed by the 'topography' and invariant properties, result in observed measurements. Nonlinear systems are characteristically sensitive to variations in initial system conditions and can exhibit exponential divergence (or convergence) of states over time.
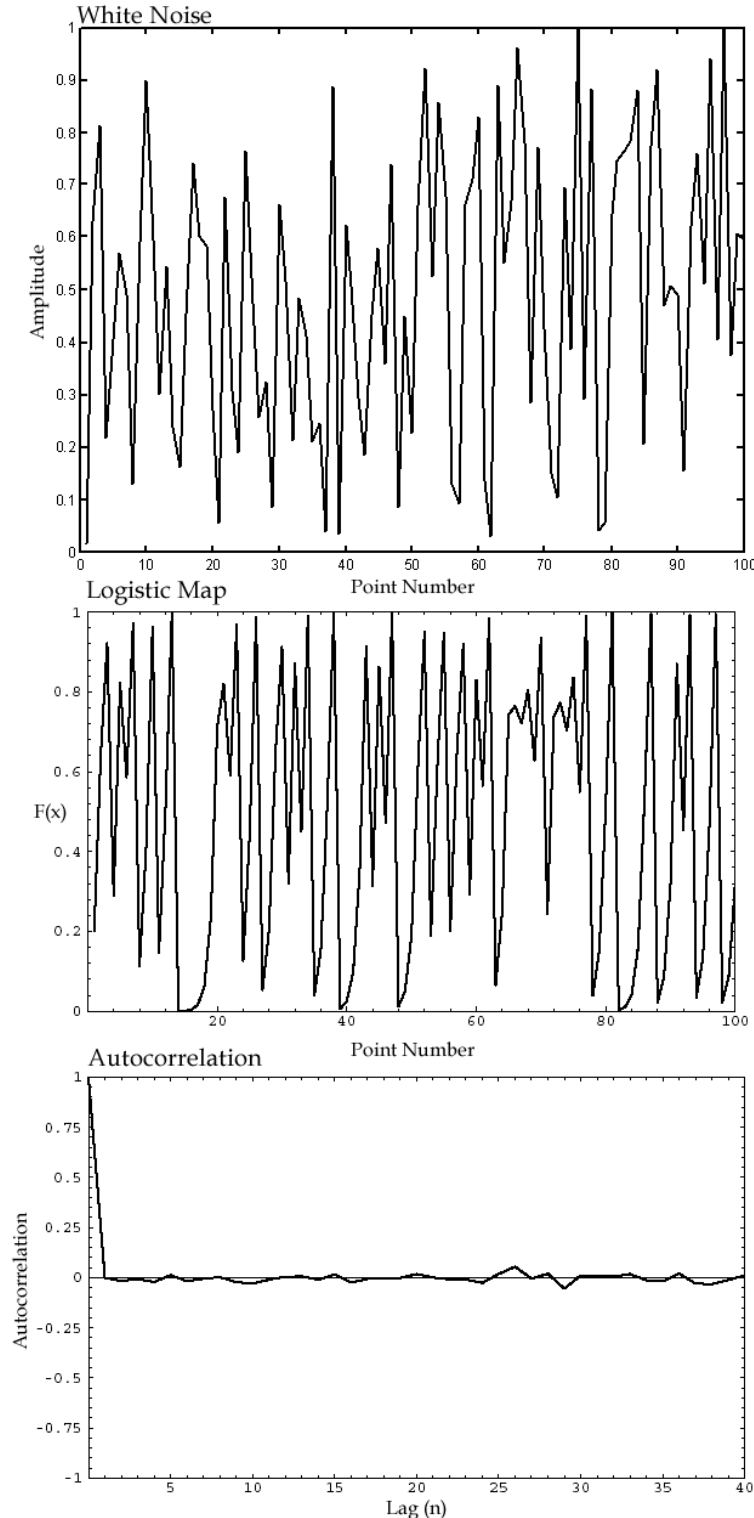
Figure 1.1. When chaotic time-series are analyzed using autoregressive moving average (ARMA) models, deterministic chaotic systems appear to be stochastic. Above, the autocorrelation function for the Logistic Map [$x_{n+1} = ax_n(1-x)$] with a = 4.0. Analysis of a chaotic signal (logistic map) results in the same auto-correlation function as for White Noise, a random signal.

Nonlinear analyses are intrinsically more suitable for describing the diversity observed in electrophysiological signals recorded from biological systems (Berge *et al.*, 1984). When applied cautiously, NTSA methods can demonstrate lessened sensitivity towards the presence of noise in recordings and 'averaging' effects caused by signal processing in windowed segments as traditionally employed in linear time-series analyses to compensate for signal stationarity (Kantz & Schreiber, 1997). Raw one-dimensional measurements (e.g. voltage recording from a single site) do not reveal the true structure of a system's state-space. The dynamics and state-space geometry of a system can only be appreciated when the dimension of the space is adequately large to encompass the entire system behaviour without projection effects.

In general, measurements from biological systems are gathered discretely, while in reality, systems change continuously over time. In other words, experimental observables correspond to discrete scalar or vector values that do not provide us with analytical (e.g. differential equation) expressions for the dynamics of the system. If we possess the nonlinear differential equations that fully describe the system and govern its dynamics, then the state-space would simply be a multivariate space with dimension equal to the number of state variables in the equations. The dynamics of the system would then be captured by continuous trajectories in that space, which represent changes of state over time. In our case, given our experimental observables, we must re-construct the state-space from the observed time-series by seeking an embedding space of adequately large dimension.

The raw one-dimensional un-embedded measurement is a truncated and projected version of the dynamics and needs to be 'unfolded' in a state-space with sufficient degrees of freedom to adequately describe a system's behaviour. As a conceptual example, consider a figure-eight ribbon, first in 2D, where points on the curve are at absolute distances from one another. Then in 3D, in a closed ribbon figure-eight. In the later case, based on the viewing angle two points may seem to be geometrically near when indeed they may be distant in the true space of the ribbon. Using an embedding technique one can reconstruct the state-space of a system from a one-dimensional time series (Mañé, 1981; Takens, 1981; Kantz & Schreiber, 1997) by

expanding the signal into a space where temporal correlations due to projection and apparent 'nearness' are absolved (see Fig. 1.2).

We can express the process of embedding with the following mathematical considerations. For an interpretation of Takens' (1981) original work, in terms of signal-processing, let us consider an unknown nonlinear dynamical system whose evolution in discrete time is described by a difference equation:

$$x(n+1) = F(x(n)) \qquad \text{(Eqn. 1)}$$

where *x(n)* is the *d*-dimensional state vector of the system at a time *n* (defined by the sampling frequency), and *F(·)* is a vector-valued function. We assume here that the sampling period is normalized to unity. Let the time-series, {*y(n)*}, observable at the output of the system be expressed in terms of the state vector *x(n)* as the following:

$$y(n) = h(x(n)) + w(n) \qquad \text{(Eqn. 2)}$$

where *h(·)* is a scalar-valued function, and *w(n)* denotes additive noise. The addition of the noise term, *w(n)*, takes into account the combined effects of imperfections and imprecisions in the observable *y(n)*. This was not explicitly stated in Takens' (1981) consideration of the method. This does not invalidate the results of the embedding-space theorem but it does allow for a degree of scatter between points when embedded in the reconstructed state-space. Equations (1) and (2) describe the state-space behaviour of the dynamical system. According to Takens' theorem, the geometrical structure of the multivariate dynamics of the system can be 'unfolded' from the observable *y(n)* with *w(n)* = 0 in a *D*-dimensional space constructed from the following new vector:

$$y_R(n) = \left[y(n), y(n-t), ..., y(n-(D-1)t) \right]^T \qquad \text{(Eqn. 3)}$$

where *t* is a positive integer called the *normalized embedding delay* (due to our previous unity assumption with regards to sampling). Thus, given the observable *y(t)* for varying discrete-time *n*, which pertains to a single component of an unknown dynamical system,

a dynamic reconstruction is possible using a D-dimensional vector $y_R(n)$ provided that the embedding space is $D \geq 2d + 1$, where d is the dimension of the state-space (or phase-space) of the system.
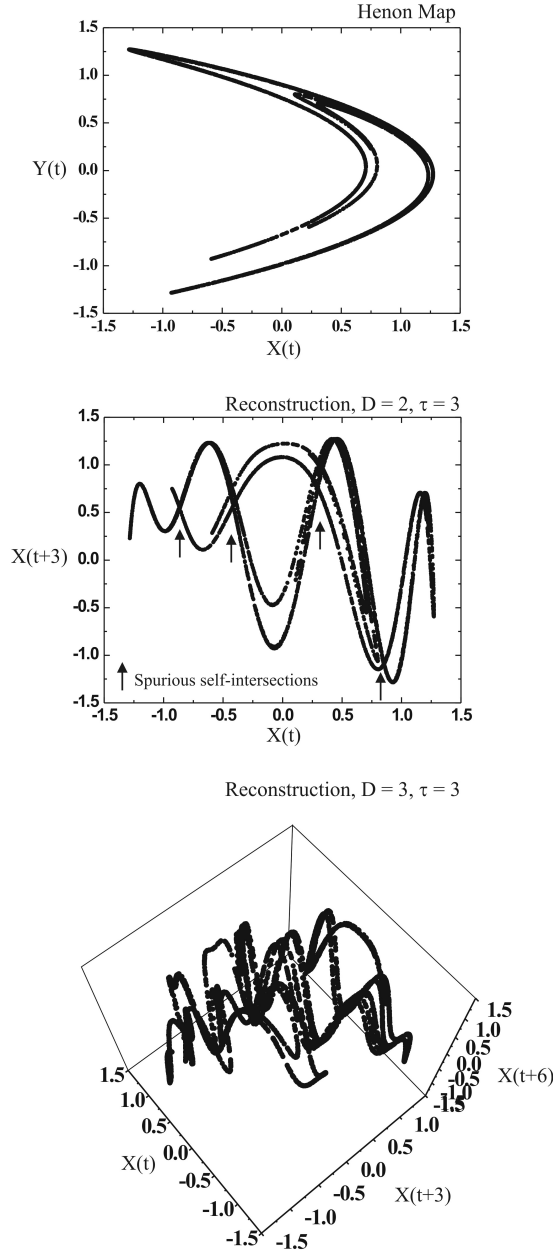
Figure 1.2. Illustration of the effect of embedding dimension using the Hénon attractor [$H(x,y)=(y+1-ax^2,bx)$] . In the top part of the figure 5000 points of the attractor are plotted in its native space using the state variables and parameters $a = 1.4$, $b = 0.3$. In this case we have analytical expressions for each of the two state variables (x and y) describing the system. Middle section, an embedding using 2D for a single 'observable', in this case x, with delay of $t = 3$. This causes spurious intersections of trajectories that are resolved by a higher embedding dimension, as shown in the lower panel by 3D embedding.

The outlined procedure is known as *delay-embedding theorem.* The condition of $D \geq 2d + 1$ is sufficient but not necessary for dynamic reconstruction. The procedure for finding a suitable *D* is called *embedding,* and the minimum (integer) value for *D* is the *embedding dimension.* If *D* is non-integer, a *fractal dimension,* then there may exist a *strange attractor* and the system can be chaotic. Almost any set of *D* coordinates is equivalent by the embedding theorem. Each set represents a different way of unfolding the attractor from its projection onto the observables and with different values of *D* (closer to the theoretical suggested dimension) one is able to make different deductions about different dynamical regimes present in the system. In our study we use the simplest embedding space of *D* = 2, and generate a so-called *first-return map* that reliably maintains most of the dynamical properties of the system and allows for the analysis of stability of fixed points (states) that exist in the state-space (Berge *et al.,* 1984; Kantz & Schreiber, 1997). The powerful implication of this theorem is that the evolution of points in $y_R(n) \rightarrow y_R(n+1)$ in the reconstruction space follows that of the original state-space dynamics of $x(n) \rightarrow x(n+1)$. Thus, many of the important properties of the unobservable state-space *x(n)* can be captured or reproduced without ambiguity in the reconstructed state-space defined by $y_R(n)$. Unfortunately, the delay-embedding theorem does not provide an explicit way of deducing the correct normalized embedding delay *t.* Nonetheless, quantitative methods exist for the determination of *t.* This relies on the fact that the delay *t* should be large enough so that *y(n)* and *y(n - t)* become essentially independent (temporally) so that they can serve as coordinates in the embedding space, however not too independent so as to lose all correlation. This requirement is best satisfied by using a value for *t* that corresponds to the first minimum of the mutual information (nonlinear self-dependence quantifier; Kantz & Schreiber, 1997) between *y(n)* and *y(n - t).* A lower-order approximation would be to use the first minimum of the autocorrelation function. An appropriate choice for *D* comes from use of state-space quantifiers such as Lyapunov exponents and correlation dimension. This approach involves incremental expansion of the embedding space by integer steps, and the calculation of the 'global ' state-space quantifier at each step until a plateau is reached in their value indicating appropriate separation of points in the state-space (Kantz &

Schreiber, 1997). Another less reliable method, false nearest neighbours, attempts to accomplish a similar task (Kennel *et al.*, 1992).

Measures designed to quantify state-space relations and properties therein such as maximal Lyapunov exponents, correlation dimension, and entropy methods have been applied to time-series from physiological systems (Kantz & Schreiber, 1997). In the context of epilepsy, correlation dimension studies of EEG have been able to demonstrate persistent epochs of lower dimension values leading to and appearing maximally negative during the seizure state. The idea here is that state-space quantifiers such as dimension represent the degrees of freedom (dimensions) required to describe the dynamics of a system by adequately unfolding observables in to an embedding space. In the simplest of terms, a measure of the 'capacity' for information.

The notion that persistent epochs of lower dimension value define pathological activity, stems from the fact that 'normal' brain activity is highly complex in waveform when contrasted to activity recorded during seizure, which is more periodic and self similar. The observed decrease in dimension is believed to represent a sort of 'neuronal complexity loss' at the population-level as compared to the non-seizure or interictal states (Babloyantz and Destexhe, 1986; Pijn *et al.*, 1991 and 1997).

Dimensional studies (Elger and Lehnertz, 1998; Martinerie *et al.*, 1998; Le Van Quyen *et al.*,2001) may have the capacity to anticipate seizures. Nonetheless, it is clear that electrographic changes may occur many hours prior to seizure manifestation (Litt *et al.*, 2001). In general, application of state-space invariant quantifiers, such as Lyapunov exponents and dimensional measures, are limited when dealing with experimental data and often are susceptible to false interpretation due to spurious scale-dependent temporal correlations, non-stationarity of signals, and finite record length (Kantz & Schreiber, 1997; Paluš, 1996; Thelier & Rapp, 1996).

One important question, which has yet to be answered, is whether the brain of an epileptic person can at all be considered to exhibit normal dynamics during epochs of non-seizure or interictal activity, save the clear existence of pathology. Indeed the term interictal plainly means that for an epileptic person, even during times of non-seizure activity, they are in a period between seizures – recall that epilepsy is defined by recurrent spontaneous seizures.

We describe a simple visualization technique, based on interpeak-intervals, that characterizes electrographic signal changes during pre-ictal and transition to ictal states. This method can discriminate between interictal, pre-ictal, and ictal states and may be adopted for serial implementation with other NTSA algorithms that can utilize interpeak-intervals as input data for state-space reconstruction (Castro and Sauer, 1997; Gong *et al.*, 1998; Slutzky *et al.*, 2001). A detailed discussion is presented with regards to the detection of significant peak/spike events, and the technique's advantages and limitations when applied to *in vitro* extracellular fields and patient EEG recordings. This methodology, Recursive Peak-Time (RPT) analysis aims to extract relevant timing-information with regards to neuronal population dynamics in the period leading to and during seizure activity. Peak detection criteria are based on the amplitude and width of peak-like waveforms and most importantly are optimized for a given signal's characteristics. This method does not require prior knowledge about the signal and is not computationally intensive, making it suitable for 'real-time' implementation. Its purpose is not to distinguish between specific signal features (e.g. spike-and-wave complexes vs. slow waves), but to provide an overall means of visualizing system behaviour for interpretation with relevant nonlinear time-series measures. We use interpeak-intervals (IPIs) as state variables. This also significantly decreases the computational burden of subsequent analysis since the total number of points is drastically reduced as compared to using the raw voltage signals. There is no loss of information as a result of converting an amplitude time-series into an interval time-series, specifically when interpeak-intervals (or interspike-intervals) are used (Sauer, 1994; Sauer, 1995). Since our method uses a peak-detection algorithm, which in based on threshold-crossing detection, then a time-delay embedding of interpeak-intervals can be considered as a Poincaré section of the original dynamical system (Sauer, 1994; Sauer, 1995; Le Van Quyen *et al.*, 1997). In summary, use of Poincaré section offers three advantages: (1) the number of coordinates is reduced, which decreases computational burden and does not require a full embedding procedure to capture essential dynamics, (2) time is discretized within the state-variable, and (3) data can now be represented as a set of difference equations and not differential equations, which equally can describe continuous trajectories (see Fig. 1.3).

System State-space   Poincaré Section

Z(t)

Poincaré
section/surface

Y(t)   X(t)

Period 1 trajectory   **Period 1 in section**

Z(t)

Y(t)   X(t)

Period 2 trajectory   **Period 2 in section**

Z(t)

Y(t)   X(t)

Chaotic trajectory   **Chatotic section**
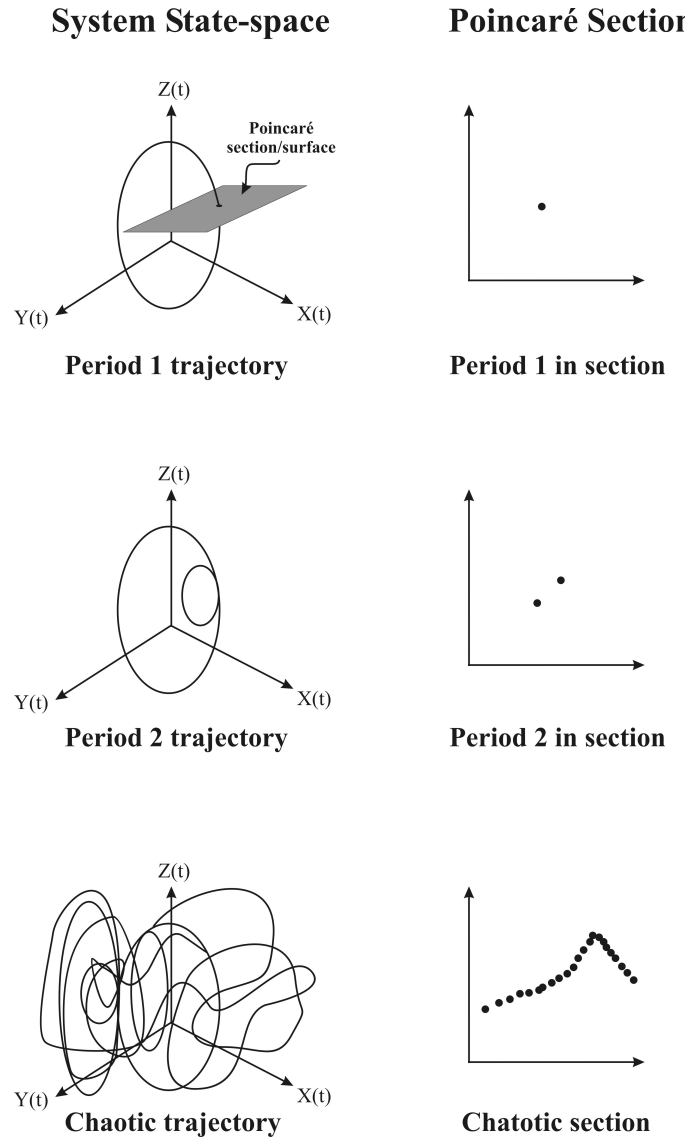
Figure 1.3. An illustration of dynamic behaviours in state-space and their equivalent Poincaré sections. The Poincaré section is a slice through the trajectories of the attractor in state-space, resulting in a smaller space that retains essential dynamics. All Poincaré sections are equivalent on the same attractor regardless of their plane. Experimental data often represents some from of a section due to limitations involved in measuring all state variables in an unknown system.

A useful and simple tool for gaining insight into the dynamics of complex dissipative systems is through recursive or return maps (Berge *et al.*, 1984; Schiff *et al.*, 1994; Braun *et al.*, 1997; Perez Velazquez *et al.*, 1999). Return maps are typically presented as two-dimensional plots of state-variable(s) at one time step plotted against the state-variable value at a future time step. The state variable is deduced from experimental observables, for example interpeak-interval in our case, and successive intervals are plotted recursively to compose the return plot. The plotting can be made with a fixed time-lag (t) in the points, as in the case of the embedding theorem, for example every second interval would be plotted recursively and so on. The simplest of such plots is with delay set to unity, $t = 1$, called the first-return map. This one-dimensional mapping has been effectively used for the characterization of many dynamical systems, for it is demonstrated to retain the dynamics of fixed system states as their Poincaré section (fixed points, will later be discussed in more detail). This does not mean that the attractor obtained in the new space is identical to that in the original space, but merely that the new representation of the attractor system retains the same topological properties that may suffice for studying essential attributes. In a dissipative system such as the brain, the state-space volume is contracted under the dynamics (Berge *et al.*, 1984; Kantz & Schreiber, 1997) and hence low order return maps offer a projection of a higher dimensional system while preserving the overall dynamical properties (Berge *et al.*, 1984; Le Van Quyen *et al.*, 1997).

We analyzed 27 records containing continuous interictal, pre-ictal, and ictal (seizure-like event, SLE) activity as recorded from eight hippocampal brain slices perfused in low [Mg_{+2}]. Further, we contrasted interictal/pre-ictal and ictal recordings with EEG recordings obtained by intracranial depth-electrodes from two patients with mesial temporal lobe epilepsy (undergoing epilepsy monitoring). Retrospective analysis was always able to detect the start of the seizures and showed that recurrent, transient epileptogenic waveforms are detectable a few minutes in advance of the seizure state. These waveforms were visualized by mapping pairs of IPIs in return plots onto a geometric adaptable nonlinear surface, allowing for 'amplification' or suppression of temporal trends within return plots in relation to epileptiform waveforms. An epileptic seizure may be considered as transient stabilization of a subset of pathological periodic

states, selected from a repertoire of states within the brain's spectrum of dynamic behaviour (Perez Velazquez *et al.,* 1999). This analysis provides a robust method for characterizing population events through a time-resolved return map visualization that can be used in conjunction with other NTSA quantifiers (e.g. Lyapunov exponents, correlation dimension, and nonlinear maps) for state-space characterization.

1.3.2 Dynamics of Transition: from Pre-ictal to Ictal and Implications for Seizure Control

The brain can be conceptualized as a set of dynamic networks of interacting ensembles of cells, whose activity includes synchronized behaviour. The characterization of the dynamical regimes that govern the transition from interictal activity to hypersynchronous ictal events (seizures) provides not only insights into the network mechanisms of collective neuronal network oscillations and synchronous activity, but also raises the possibility of controlling this transition. Most of the current research in epilepsy and mechanisms of neuronal synchrony emphasize the molecular and cellular aspects. However, given our understanding of the integrative functions of the brain, the global and collective dynamics that lead to pathological hypersynchronous activity of neuronal networks is poorly understood. The development of nonlinear time-series analyses has fostered the application of these methods for the understanding of the underlying dynamics of complex biological systems (Elbert *et al.* 1994) and in some cases, for the control of their activity (Christini & Collins, 1996; Garfinkel *et al.* 1992). Considering evidence that spontaneous interictal brain activity can be paced *in vitro* employing chaos control techniques (Schiff *et al.* 1994), as well as evidence from other systems where similar methods were used by taking advantage of the system's nonlinear dynamics (Shinbrot *et al.,* 1993; Christini *et al.,* 2001), we hypothesize that the transition from interictal to ictal activity can be controlled by adequately placed and timed minimal perturbations.

Nonlinear time-series analyses of voltage traces from epileptic patients, as well as from animal epilepsy models, has revealed that seizure activity represents a nonlinear process with dynamics distinct from interictal or pre-ictal states (Pijn *et al.*, 1991; Lehnertz & Elger, 1995; Elger & Lehnertz, 1998; Lopes Da Silva & Pijn, 1999; Litt & Lehnertz, 2002). State transitions from interictal to ictal events have been inferred from the geometrical properties of the attractors reconstructed from the original voltage recordings, specifically from correlation dimension and Lyapunov exponents (Iasemides & Sackellares, 1996; Lian *et al.*, 2001). However, as mentioned previously, the need for stationarity and length of the recordings makes the interpretation of these quantifiers difficult (Rapp, 1994). We recently used interpeak-interval delay plots to investigate the transition to seizure in human epilepsies (Perez Velazquez *et al.*, 1999), using quantitative mathematical analyses that do not have data requirements as stringent as the methods mentioned above. These studies suggested that intermittency is a dynamical regime underlying human seizures, which together with other experimental and theoretical evidence, further indicates that sudden changes in physiologic variables bring specific brain networks near a bifurcation point at which the transition to seizure takes place (Lopes Da Silva & Pijn, 1999). Considering this information, it is conceivable to propose that the transition to seizure can be arrested by specific perturbations dictated by the known dynamics of the epileptogenic areas.

In this study, we sought to characterize the dynamics of the transition from interictal to ictal activity and to use this knowledge to control the activity thereby preventing seizure occurrence. We use an *in vitro* seizure-like model that is characterized by spontaneous recurrent interictal activity that develops into seizure-like events (SLEs), considered to be a model of status epilepticus (Rafiq *et al.*, 1993, 1995). The transition from interictal to ictal activity was marked by the sudden and transient stabilization of a high-frequency hypersynchronous steady state. Brief direct electrical stimulation halted the transition from pre-ictal to ictal activity, by forcing the stabilization of an interictal-like steady state, as opposed to the hypersynchronous ictal state.

II Methods

2.1 Sources of Data

2.1.1 Hippocampal Slice: Preparation

Hippocampal brain slice recordings were obtained from male Wistar rats (17-25 days old). Animals were anaesthetized with halothane and decapitated. The brain was quickly dissected and maintained in ice-cold artificial cerebrospinal fluid (ACSF) for 4-5min. Horizontal slices were cut according to the procedure described by Rafiq *et al.* (1993 and 1995). Briefly, the dorsal cortex of each hemisphere was cut parallel to the rostral/caudal axis and glued dorsal side down to an aluminium block, with caudal end towards the blade. The block was secured at ~ 12-14° angle, and hippocampal-parahippocampal brain slices of ~ 450mm in thickness were sectioned using a vibratome. Slices were kept at room temperature in oxygenated 'normal' ACSF (95% O_2, 5% CO_2) for at least one hour before recording. Normal ACSF was composed of the following (in mM): NaCl 125; KCl 5; NaH_2PO_4 1.25; $MgSO_4$ 2; $CaCl_2$ 2; $NaHCO_3$ 25, and Glucose 10. The pH was ~ 7.4, with osmolarity in the range of 300 ± 5 mOsm. For recording, spontaneous seizure-like events (SLEs) were induced by perfusing the slice with ACSF containing 0.5mM Mg^{+2} (Dreier and Heinemann, 1991).

For recording purposes, slices were transferred to a superfusion chamber maintained at ~35 °C (Medical Systems Corp., Model PDMI-2, Harvard Apparatus, St. Laurent, Quebec, Canada).

2.1.2 Hippocampal Slice: Recording and Stimulation

Extracellular responses were recorded with a NaCl-filled (150 mM) borosilicate glass pipette located in stratum pyramidale of the CA1 region (see Fig. 2.1). Signals were recorded, amplified, and filtered (1 kHz low-pass, single pole Bessel on amplifier) with an Axoclamp 2A amplifier (200B, Axon Instruments, Foster City, CA, USA) in bridge mode. Output from the Axoclamp was then low-pass filtered at 625 Hz with an 8-pole Bessel (50x gain onboard) filter before application of additional gain for total of 1000-2000x , depending on the intensity of responses from the slice. Generally, we attempted to fill at least 20% of the dynamic range of the A/D for the lowest amplitude responses. Data was stored in real-time on videotape using a digital data recorder VR-10 (Instrutech Corp., NY, USA) at 44 Khz for later playback, or was digitized directly onto computer using the AxoTape software at 2 KHz. For RPT analysis, continuous recordings on videotape were retrieved by re-digitization from the videotape into the computer using the AxoTape software, with a sampling rate of 2 kHz.
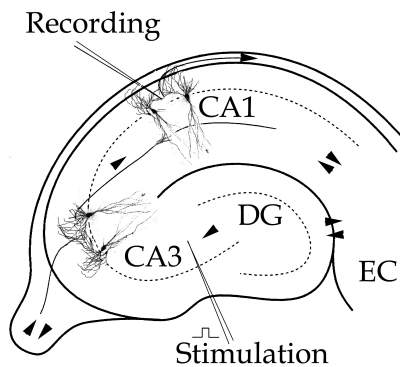
Figure 2.1. A schematic diagram of a horizontally cut rat hippocampal slice. CA3, CA1 and DG (Dentate Gyrus). Recordings were made from the CA1 layer. Stimulation was delivered to the Mossy Fibres, which are collaterals running from DG cell layer innervating the CA3 layer. This diagram is a gross over-simplification of the intra-hippocampal circuitry for it does not include the complex interneuronal network and is absent of the parahippocampal structures such as the EC (Entorhinal Cortex), which has reciprocal connections between (mainly) DG and CA1 cell layers. In our experiments, we selected slices that retained EC and parts of Subiculum (not shown above). Arrowheads represent some of the other known 'information' pathways.

Extracellular orthodromic electrical stimulation (100 μs pulse width) was delivered via a bipolar stimulating enamel-insulated nichrome electrode, using a Grass square pulse stimulator (S88K, Astro-Med Inc., West Warwick, USA). The intensity of the stimulation was fixed for each experiment but varied between slices, adjusted to the value that evoked a field potential event recorded in the CA1 area when stimulating the mossy fibres (see Fig. 2.1). Design, experimentation, and analysis of the period pacing seizure control experiments were performed by mutual equal collaboration between Houman Khosravani and Dr. José L. Perez Velazquez (Brain and Behaviour Program, Hospital for Sick Children, Toronto, Canada), who played a critical role in the project.

2.1.3 EEG Recordings

Intracranial EEG recordings of seizures were obtained from implanted depth electrodes in two human patients: one with unilateral mesial temporal lobe epilepsy, the other with a bilateral temporal lobe seizure disorder – both undergoing pre-surgical EEG monitoring. Electrode implantation was performed by Dr. Andres Lozano (Staff Neurosurgeon, Toronto Western Hospital, University Health Network, Toronto, Canada). Continuous, interictal and ictal epochs of EEG were digitized at 200 Hz (Stellate Systems - Montreal, Canada). Electrographic seizure onset was determined by Dr. Richard Wennberg (Staff neurologist-electroencephalographer and epileptologist, Toronto Western Hospital, University Health Network, Toronto, Canada), who is an expert in the field and has specialized training in intracranial EEG interpretation. All EEG data was collected with approval of the University Health Network Board of Research Ethics. It is important to distinguish between electrographic seizure onset and clinical seizure onset. The former refers to the time point at which definitive EEG changes are visible in the recording as compared to background activity and the patient has not exhibited any alterations of state (automatisms, loss of consciousness, or other 'abnormal' activity). The later is defined as the time when clinical changes or alterations of state have begun and the patient is experiencing the seizure state. For all analyses of EEG that we will be discussing we are always referring to the electrographic onset,

which always precedes or begins at the time of clinical onset. For the two individuals in our study, clinical onset always proceeded after electrographic onset.

2.2 Time-series Analysis

2.2.1 Peak Detection · Amplitude

RPT analysis is designed to extract temporal information from identified events (i.e. peaks) recognized to be neuronal population activity in electrophysiological recordings from brain slices and intracranial EEG. Population events are characteristically defined as sharp transients with amplitudes correlated to the number of neuronal units involved and the degree of synchrony between units, at the time of event generation. We developed a graphical-based software, Electrophysiological Signal Analysis Facility (ESAF), using Visual Basic (Microsoft) with Fortran (Compaq) math components (via DLL) to carry out the peak-detection and subsequent analysis of the time-series data[*]. The analysis was carried out on a Pentium III 850 MHz computer running the Windows2000 (Microsoft) operating system. Peak detection is kept general in nature and is based on two criteria: amplitude and width. In the case of the amplitude criterion, a threshold is selected using an automated procedure, autosigma (described below), and is followed by a 'moving' Signum function that checks for sign inversion between successive pairs slopes for data points that satisfy the threshold. As a first step, it is desirable for recordings to have a stable baseline, this allows for preferential peak detection either above or below this 'line' of reference. This is relevant since both field responses and EEG (when considered negative down) typically have a sharp early component (appearing below baseline, BB), followed by a slower, more wave-like component that appears inverted relative to the initial (above baseline, AB). These distinct response components have different physiological mechanisms and by electing for them, one allows for their independent temporal investigation. When detecting

---

[*] ESAF © 2002 developed and coded (1998-2002) by Houman Khosravani, please write h.khosravani@utoronto.ca for authorized copy.

features above baseline, only positive-to-negative slopes are considered to be peaks and vice versa for below baseline detection runs. For sensitivity, slice field recordings were typically analyzed AB for the interictal/pre-ictal period and BB for the SLE due to the polarity inversion that is characteristic at onset. However, AB detection overall serves generally well for a mixed recording. The extracellular field for the pre-ictal segment is composed of EPSP-like waveforms with overriding population spikes. The ictal stage is characterized by negative-deflecting population spike waveforms. Analysis of EEG was typically performed BB since negative deflecting sharp transients are associated with epileptiform activity. Nevertheless, rather small differences in results were obtained between analyses results (AB vs. BB) due to the generality of detection criteria and the nature of recordings.

EEG has a robust Gaussian amplitude profile for artefact free recordings (e.g. without electrode drift and movement artefact). Intracranial depth-electrode EEG, as compared to scalp, allows for much cleaner recordings, especially when electrodes are placed in deep, closed field, structures such as the hippocampus. Extracellular field recordings in general do not posses a Gaussian amplitude distribution due to the morphological diversity of recorded waveforms. However, the amplitude profile for these recording becomes more Gaussian-like upon DC-shift (and other putatively non-physiological slow-waves) subtraction using a high-pass filter between 0.2-0.3 Hz (depending on drift severity). Gaussian-like profile was achieved for slice recordings by subtracting DC-shifts using a "moving-average" filter (Press *et al.*, 1992) with a window length corresponding to ~ 0.05% of data segment duration and ¼ window-length overlap. In half of the cases, a finite impulse response (FIR) filter (Filter Design Toolbox, Matlab, MathWorks) of high order (> 500) with hamming window and a cut-off of 0.3 Hz was used. The moving average is more susceptible for introducing some nonlinearity at the window edges, however our peak-detection was always above this level and detection results were fully comparable with the FIR filtered traces. Filtering should generally be avoided when possible – however, we found these filters to work well by preserving the waveforms while approximating the baseline linearly.

2.2.2 Peak Detection · Autosigma

Given a stable signal baseline, the software then performs an automated computation in order to select an optimal amplitude threshold for peak detection. For the Gaussian-like distribution of amplitudes present in our signals, the mean absolute deviation (MAD, *m*) was calculated and used as a robust estimate of the width of the signal's amplitude distribution (Press *et al.*, 1992). This width is corresponds to baseline 'noise' for signals of adequate duration that have been over-sampled. This notion further supports the use of a 'moving average' filter as a good estimate of baseline drift. In our case, the baseline is mainly electrical or chamber 'noise' introduced by the recording process. A multiple of the MAD value (referred to hereafter as sigma, $s = mp$, where *p* is some real number) was used to express the amplitude threshold used for peak detection. Events that satisfied this threshold criterion, in addition to exhibiting the appropriate sign of slope inversion, were marked as preliminary identified peaks. The optimal sigma was determined by constructing a 'growth plot' in a procedure here referred to as *autosigma*. This is accomplished by performing successive peak detection runs on a time-series, while keeping track of the number of events detected at each sigma increment. The resulting 'curve' approximates the true amplitude profile of the signal about one side of the baseline. For example, if a signal is over-sampled and possess noise that is strictly Gaussian in distribution of amplitudes and there exists an event that satisfies a $s = 2.0$ threshold, then that event can be considered to differ from noise with ~ 95% confidence. Rather, ~ 95% of the signal's amplitude distribution may be ignored since it is at the level of 'noise' due to the fact that peaks compose a very small fraction of the data points in an over-sampled signal. Thus, our events of interest (peaks) must occur on a time-scale that is ~ 5 to 10 times slower than the sampling rate in order to provide practical over-sampling. Detection starts at a small step value (s_s) that is incremented linearly until sigma is equivalent to the largest signal amplitude (AB or BB) in that recording. The signal's approximate amplitude profile (see Fig. 2.2) is plot of number of events detected vs. sigma. It is evident that extremely small values of sigma over-sample the signal by identifying too many peaks, while large sigma result in under-sampling. The optimal sigma for peak detection lies in the intermediate region and can be

estimated using two geometrical methods for attaining lower and upper bounds on an 'ideal' sigma value. The lower limit of sigma is determined by calculating the slope of the secant subtending the end-points of the amplitude profile curve; followed by a running slope calculation that compares the local slope to the secant slope starting at low sigma and ending at local slope greater than or equal to secant slope (marker 2, Fig. 2.2). Starting at the largest sigma explored and performing a running local least-square fit toward lower sigma values, the y-intercept is continuously calculated.

The upper bound for sigma is the point on the curve when the y-intercept equals or is greater than the largest number of event detections (equal 1 when normalized, marker 1, Fig 2.2). The ideal sigma is set to the average between the upper and lower bounds (marker 3, Fig. 2.2).
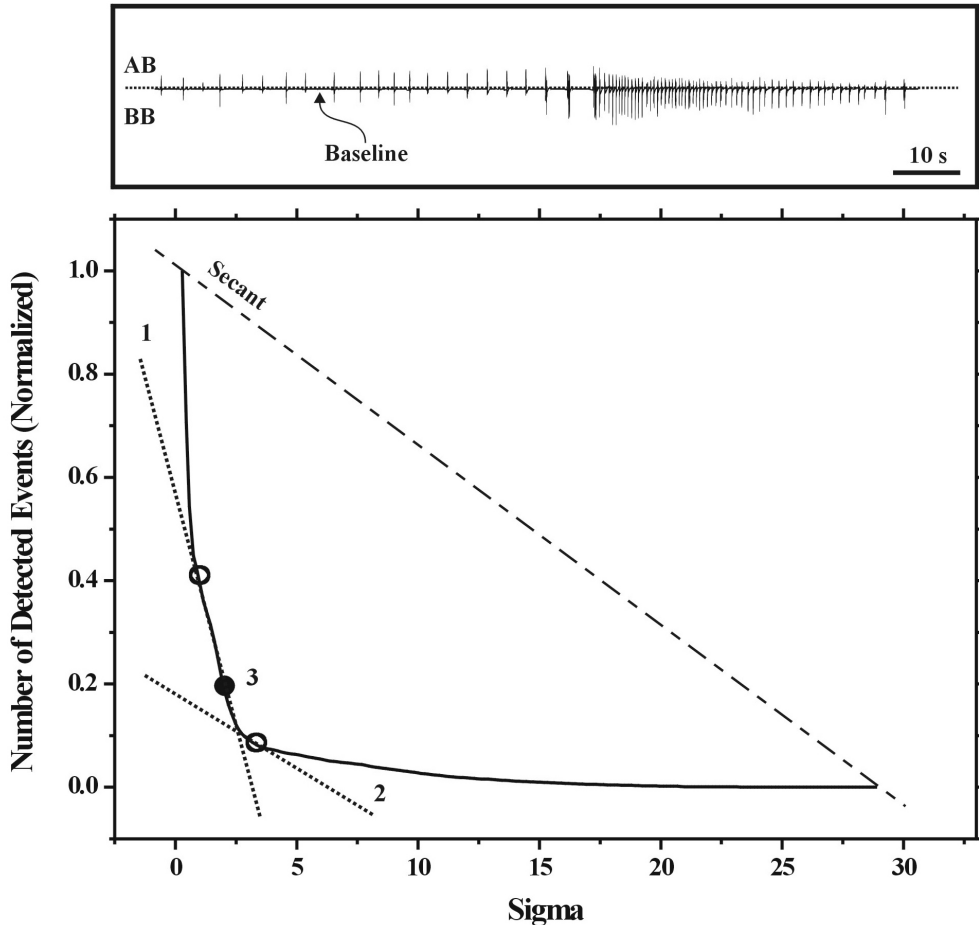
Figure 2.2. Successive peak detections at incremental values of sigma (amplitude threshold) for fixed width criterion value. The solid curve is a sample autosigma analysis of a slice recording (upper panel). The curve, events detected vs. sigma, is an estimate of signal's amplitude distribution or profile. Two methods used for optimal sigma (3) selection: (1) Lower bound ∕ y-intercept method - the point where local y-intercept of curve exceeds maximum number of events detected. (2) Upper bound ∕ Secant method – local slope on curve greater than or equal to secant subtending curve. Average of (1) and (2) is considered to be the optimal sigma threshold (3). Number of events detected is normalized to the maximum number for the signal undergoing analysis.

2.2.3 Peak Detection · Width

Upon determination of a suitable amplitude cut-off, peaks are then detected at that optimal threshold, by a second pass through the data; this time inspecting the time interval (Dt) between successive pairs of identified peaks. If this time interval is less than a specified width criterion (expressed in terms of frequency, $w = 1/Dt$), then the two peaks are averaged into one feature at the average time. This revised peak location is then compared with the time location of the next identified peak event. This aids in preventing the detection of excess false-positives from low amplitude, fast transients that ride on top of large amplitude features. This step is analogous to a frequency cut-off for the detected responses. We can define w in terms of the sampling frequency, f_s , which corresponds to a time point every sampling period T (where $T = 1/f_s$). Thus, we impose the following restriction: detected peaks identified as lying closer in time than Dt ($Dt = cT$, where c is a user selected constant), are fast, low amplitude noise or artefacts that should not be made resolvable into distinct events. In our analysis ($n = 27$ slice recordings, $n = 20$ EEGs, and also in Perez Velazquez *et al.*, 1999) it was observed that values for c in the general range of $c = 5 – 10$, generated highly reproducible results in terms of the final visualization plots. In the case of slice recordings we typically fixed w between   250 Hz $< w <$ 300 Hz depending on the quality of the recording. In the case of EEG we fixed $w = 45$ Hz. These rough boundaries were determined by spectral analysis of several sample signals. The exact value of c, which can be considered as $c = f_s / f_w$ (f_w , desired upper frequency cut-off) is at the discretion of the user and warrants consideration based on experimental conditions and limitations imposed on data by the sampling frequency and acquisition instrumentation.

2.2.4 Influence of Noise on Peak Detection

RPT analysis is used to visualize the temporal dynamics present in the recordings. Practical identification and visualization of these dynamical states depends fundamentally on the relation between inherent signal characteristics and detection parameter values. In order to assess the influence of noise on our most sensitive detection criteria, the amplitude threshold, a template file was analyzed with incremental levels of 'noise'. This study was performed on a sample slice recording, since the *in vitro* data exhibit the greatest deviation from a Gaussian-like amplitude profiles and have diverse waveforms, making them more challenging to investigate and susceptible to noise. With respect to intracranial EEG recordings as noted previously; these signals have amplitude profiles that are closely Gaussian and hence there is a strong tendency for the autosigma procedure (described previously) to select sigma values within a confined range.

A signal template file, representing a typical complete slice recording containing interictal, pre-ictal, and ictal segments was selected in addition to a baseline-only template (see Fig. 2.3a). Equivalent amount of baseline noise was then added to signal and baseline template pair with incremental magnitude. In order not to introduce a bias in the type of noise added (in the context of the amplitude distribution of the noise itself), a baseline-only file was used. This file was six times the length of the signal template and was composed by piecing together of several baseline segments from the same slice that the template was obtained from, i.e. identical experimental conditions. The signal template and baseline-only template MAD values were within 5% of each other. Using an appropriate random number generator (Press *et al.*, 1992), random samples from the baseline-only file were selected, thereby composing a subset baseline file with duration matching that of the templates. To review, we now have a signal template and a baseline-only template with equal durations and similar MAD values – MAD of a signal appropriately describes the width of the distribution of amplitudes in that signal (Press *et al.*, 1992). Also, we have a baseline-only sample file that is much longer in duration than the template files. A procedure was then repeated where random samples were taken, such that their length matched the template files, from the

baseline-only sample file, scaled by a decimal multiple (*a*, dimensionless), and added to the template pair. Noise was added to both signal and baseline-only templates since the signal template itself has a baseline component within it. Recall, our aim is to isolate the effect of increased noise levels on the number of events detected in pure signal template. Results of noise addition are pairs of new template files with a specific level of added baseline noise. Next, peak detection was performed using the autosigma procedure on pairs of template files. Number of detected events, computed as the difference in detected events between signal and baseline-only templates, was plotted at each noise level (see Fig. 2.3b). Peak detection runs were performed for both AB and BB settings and revealed only a slight difference in the overall observed trend (see Fig. 2.3b), with more events detected overall for BB at any particular noise level. This analysis demonstrates that given the distribution of amplitudes in our recordings and the method of peak detection, the greatest difference between signal and noise (in events detected) occurs at approximately *s* = 2.0. Further, this near optimal value for peak detection decreases in magnitude by e^{-1} at *s* ~ 3.91 (1° exponential fit, R^2 = 0.99). This suggests that the range over which sigma is functional in extracting relevant peaks spans the range from ~ $1.5 \leq s \leq 3.9$, with an optimum value near *s* = 2.0.

Baseline Only File – [6 times the duration of template files]
Description: A file with no electrophysiological activity recording containing baseline equipment + electrical noise. Long duration provides adequate reservoir for random samples.

Baseline Only Template
Description: File with exact length of *Signal Template* file and a MAD value within 5% of the *Signal Template*. MAD is the approximate measure of baseline (noise) spread.

Signal Template
Description: File containing electrophysiological recording of complete interictal, preictal, and seizure activity. Signal contains noise due to instrumentation.

+

a * RND sample

a * RND sample

+

Scaled (a) Noise
Description: Noise file with exact template duration and approximate MAD value of *Baseline Only* file. Obtained by taking random samples from the *Baseline Only* file and scaling them with decimal parameter α and adding result to the template. Note, *Scaled Noise* random samples here are different for *Signal Template* as would be for true noise.

Scaled (a) Noise
Description: Noise file with exact template duration and approximate MAD value of *Baseline Only* file. Obtained by taking random samples from the *Baseline Only* file and scaling them with decimal parameter α and adding result to the template. Note, *Scaled Noise* random samples here are different for *Baseline Only Template* as would be for true noise.

Increment a

ESAF – AB & BB
Analysis by ESAF using *Autosigma* for incremental level of added noise, counting number of peaks detected AB and BB at each α level.

ESAF – AB & BB
Analysis by ESAF using *Autosigma* for incremental level of added noise, counting number of peaks detected AB and BB at each α level.

Results Displayed in **Figure 2.3b**
NE_{α} = Number of peaks detected for given α
$NE_{AB,\alpha} = NE_{AB,Baseline\ Only,\alpha} - NE_{AB,Signal,\alpha}$
$NE_{BB,\alpha} = NE_{BB,Baseline\ Only,\alpha} - NE_{BB,Signal,\alpha}$

Figure 2.3a. Flow diagram of how the influence of noise on *autosigma* peak detection was investigated on sample *in vitro* recordings. See Methods 2.2.4 and Figure 2.3b.

Figure 2.3b. Effect on number of peaks detected with increased magnitude of baseline 'noise'. Two templates, one signal (upper panel, a = 0, dimensionless, see 2.2.4) and one baseline-only (not shown) were selected and analyzed for incremental levels of baseline noise. Template files had similar MAD values (see methods). For each added increment a 'noise-series' was generated from random samples taken from a baseline-only signal ~ 6 times longer than the template duration. Added noise was then scaled in amplitude by a decimal factor (a) and added to both signal and baseline-only templates. Peak detection was performed on both signal and baseline-only template pairs with incremental 'baseline noise' (e.g. upper panel, a = 5 and 15). Number of events detected was subtracted for each signal/baseline-only pair with above baseline (AB) and below baseline (BB) analysis. Solid curve spline fit of averaged value. Maximal difference between signal and baseline-only templates, the optimal sigma for peak detection threshold, occurs for $s \cong 2$.

2.2.5 IPI Plots and the Frequency Potential

A well-described visualization and analytical tool for complex data is the first-return plot (Berge *et al.*, 1984; Kantz and Schreiber, 1997). This entails recursive plotting of a data series, in our case, extracted *IPI* values, such that IPI_n is plotted versus IPI_{n+t} , where *t* , is referred to as a delay and represents an integer displacement (index) value between points plotted (see Takens theorem in Methods). Recursive plots essentially display the distribution of successive intervals between peaks, in effect folding the dataset onto itself, revealing internal temporal trends. Dynamically, first-return maps (*t = 1*) offer the simplest projection (Poincaré section) of a system occupying higher-dimensional state-space . From a time-series perspective, the return plots are discretized version of the the actual multidimensional (multivariate) state-space, which preserve critical information about dynamics (Kantz and Schreiber, 1997). Further, invariant measures, which remain the same under state-space transformations, may be calculated directly from the return maps, although some with discretion due to the peculiarities of biological datasets (Berge *et al.*, 1984; Paluš, 1996; Thelier and Rapp, 1996). This brings focus to the importance of accurate representation of state variables for state-space reconstruction – in this case detection of peaks their and computation of IPIs. Recursive plots (see Fig. 2.4a) display the distribution of IPIs calculated for a segment of data, yet they are incapable of quantitatively visualizing the temporal evolution of successive IPIs as obtained from the time-series. This is of importance since what is actually occurring is a time-evolving, low-dimensional, projection (Poincaré section) of the system's trajectory in state-space. In order to visualize the temporal-evolution of successive IPIs, one can plot 3-dimensionaly, IPI_n vs. IPI_{n+1} vs. time (e.g. Fig. 2.4c). However, this method of visualization, although insightful, is not easily quantifiable in a practical sense. As a means of visualizing the low-dimensional projection trajectory of the system in state-space we devised a quantifier for representing each *(IPI_n , IPI_{n+1})* pair – the Frequency Potential. Plotting of this measurement versus time allows for direct visualization and quantification of projected state-space trajectories along time.

Frequency potential (FP) is obtained by mapping pairs of IPI values in a 2D projection space, onto an adaptable nonlinearity as manifested by a geometrical surface (see Fig. 2.4c). The surface (defined by Eqn. 4) acts as a nonlinear 'response mapper' that amplifies the relative distance between points near the origin, which is the region of high frequencies or short intervals. This allows visualization of IPI coordinate pairs, in time, such that their sequence in series may be 'stretched out'. The surface does not provide a unique mapping and was selected based on the observed topography (distribution of IPI pairs) in return plots during interictal, pre-ictal, and ictal states. The topography of the surface defines larger FP values as corresponding to higher frequencies and small FP values to lower frequency events. The following analogy may prove useful; the surface represents a kind of landscape, one whose most elevated point corresponds to successive high frequency events; assumed to be associated with greater seizure propensity. In contrast, the lower 'foothills' of this surface correspond to successive low frequency events and are associated with non-seizure and/or interictal activity (Fig. 3a).

$$FP = (s * IPI_n * IPI_{n+1})^{-k} \equiv (s\,xy)^{-k} = z \qquad \text{(Eqn. 4)}$$

Although the mapping is not unique, a degree of distinction between paired-IPIs may be imposed. We defined a signum-like variable s, which can take on values of either *1* or *–1* depending on which side of the identity line the IPI pair is mapped (see Fig. 2.4a). This exploits an asymmetry that we have observed in our return plots with relation to changes in IPI distribution, which take place pre-ictally during transition to the seizure state. If the variable s is simply ignored we can define aFP as the absolute Frequency Potential (aFP). This later quantity is general and not sensitive to the position of IPIs about the identity line; only to successive high frequency events and/or fast transients. The functional form of the surface was chosen arbitrarily due to its intrinsic 'response topography' to the observed distributions of recursive IPI plots. In principle, alternative functional forms may be selected in order to enhance or suppress specific signals or signal components that of interest for time-series processing.
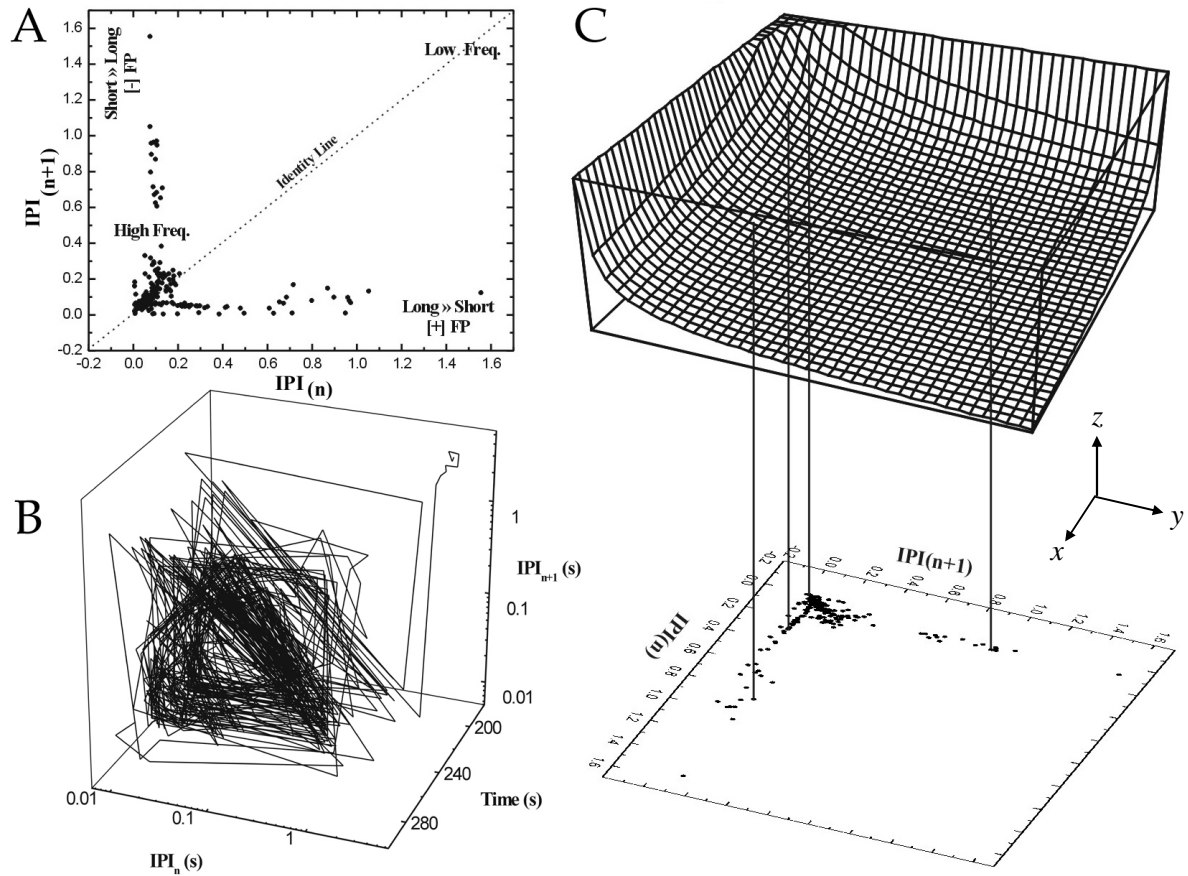
Figure 2.4. Recursive Interpeak-interval (IPI) plot and its relation to the Frequency Potential (FP) surface. **(A)** A first-return map of successive IPIs for a segment of slice recording ictal activity. The distribution of points allows for direct visualization of frequently occurring IPI (clusters of points). Regions of plot are labeled as corresponding to frequency and FP values. Points above the identity line obtain negative FP values and positive FP for IPIs below. Recursive plots can provide analytical solutions to dynamics and can be used to measure state-space invariants. Temporal evolution of successive IPIs is not visualized or quantified. **(B)** A 3D IPI recursive plot. This is identical to the plot made in (A) but it includes the time-axis, which captures the sequence of the IPIs as computed from the raw voltage trace. Note the IPI interval axes are in logarithmic scale and once again have units of time (in seconds). The sequence plotted corresponds to an ictal event. **(C)** The absolute value Frequency Potential surface is an adaptive nonlinearity onto which pairs of IPIs can be mapped (vertical lines from IPI plot onto surface). This allows for direct visualization of their position on the IPI plot over time. The function of the FP surface is to distinguish between positions of IPI coordinate pairs over time, with emphasis on the high frequency region corresponding to epileptiform fast transients. The steepness of the surface can be altered by a single parameter (see methods) and the shape of the surface itself may be changed to enhance or suppress specific regions on the IPI plot.

The shape of the FP surface, the nonlinear mapper (Eqn. 4), depends critically on the exponent k that is used to 'tune' the surface's response to differing states. A large value results in a surface that rapidly declines about the (origin) high frequency region, resulting in decreased sensitivity in discriminating trajectories created by large successive IPIs – low frequencies (see Fig. 2.5). Comparatively, small values of k are poor at resolving the high frequency region, but have an overall better sensitivity to the position of IPI pairs. In an attempt to extract maximal information using the FP, we devised a scheme to optimize the value of k so that the FP surface exhibits optimal sensitivity to trajectories for a given recording. FPs were calculated for all points in a given IPI plot with some initial surface exponent close to zero. The interpolated FP values were plotted vs. time (see Fig. 2.5) and the length of the resulting trace was calculated in Cartesian form. Note that a small value for k results in a surface that is less 'steep' about the origin and more sensitive to low frequencies as compared to high. FP-time traces are significantly longer in length for smaller values of k than for larger ones. As k increases, the length of the FP-time trace goes to the limit of a straight line subtending the duration of the recording. Using this relation, we repeat the interpolation process for incremental values of k starting from near zero and proceed up to $k \sim 2$, thereby generating a series of FP-time (or aFP-time) plots, such as in figure 2.5. Note that since the surface is a power function (Eqn. 4) evaluated at different parameter values (i.e. k's), FP is normalized to the absolute maximum FP for a given data segment as evaluated for a specific k value. This scale correction ensures that the trace length provides an accurate measure of variation amongst FPs as calculated for different k values. An 'optimal' value for k was approximated using a 'growth plot' approach similar to the one used for sigma (see Fig. 2.2). The resulting curve (not shown) for *trace length* vs. k value is generally very smooth in appearance, which facilitates a more accurate determination of an optimal k value.
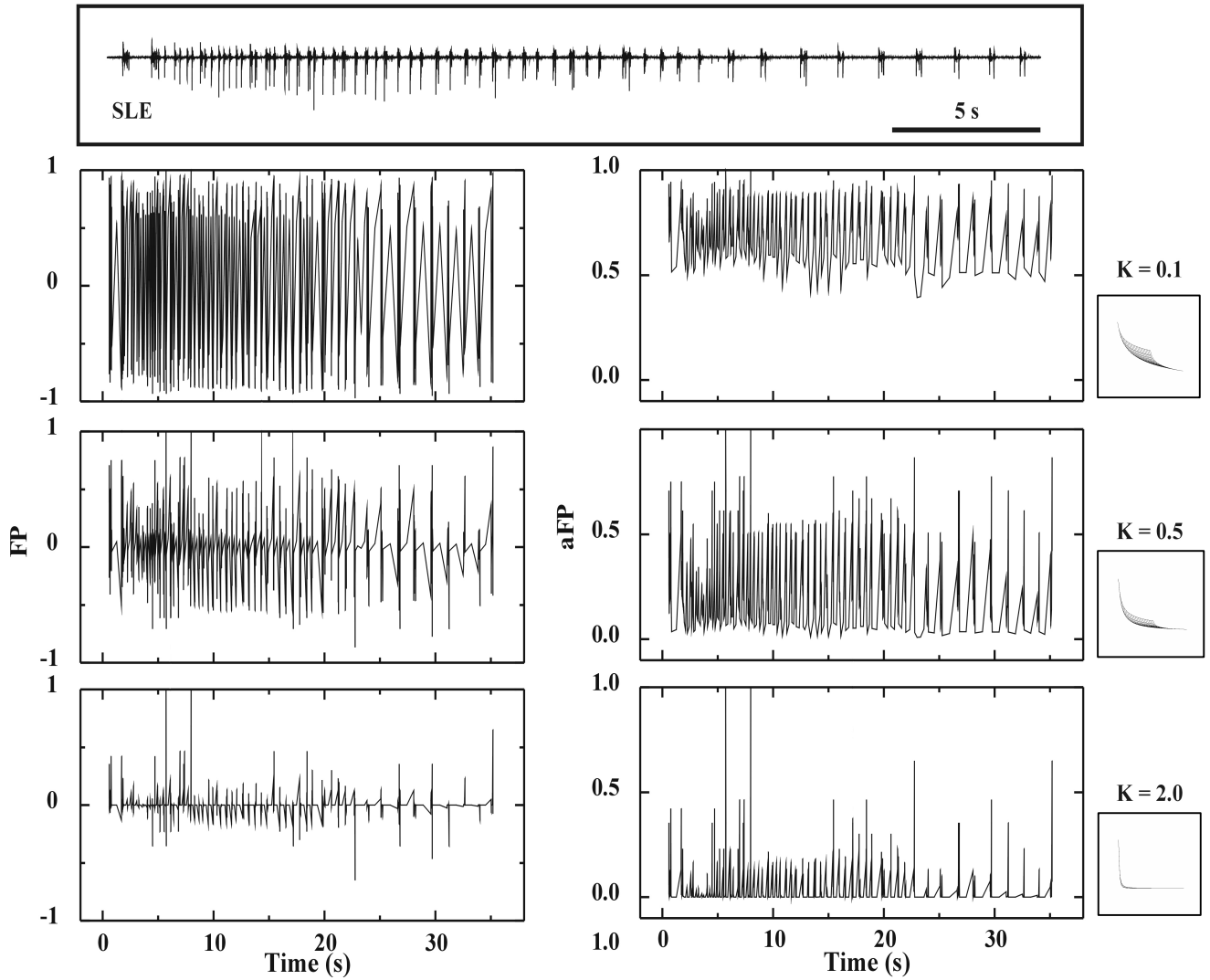
Figure 2.5. Effect of altering the shape of the FP surface on mapped IPI values from a seizure-like event (SLE) *in vitro* recording (upper panel) for two quantifiers: Frequency Potential with identity discrimination (FP, left panels), and absolute-valued Frequency Potential (aFP, right panels). The functional form of FP surface (see Eqn. 4, methods) allows shape manipulation using the parameter *k*. For small values of *k* (e.g. *k* = 0.1) the surface performs poorly at resolving short IPIs and is very sensitive to all IPIs. Large values of *k* (e.g. *k* = 2.0) result in a surface that rapidly declines about the high frequency region, resulting in decreased overall sensitivity and poor resolution for long intervals. The x-z projection of the surface with corresponding *k* value can be seen in insets below each *k* value. Optimal value for *k* is determined by constructing a plot of Cartesian trace-length (for above such plots) at incremental values of *k* and performing a similar estimation procedure as used for optimal amplitude threshold (see Fig. 2.2). FP and aFP values were normalized relative to their maximum value respectively, as calculated for each *k*.

2.2.6 First-return Maps & Fixed Point Analysis

We have already outlined the mathematical analysis that is performed on the voltage traces, specifically, the detection of peaks, computation of interpeak-intervals, and composition of a Poincaré recursive plot (see Introduction and Methods). Briefly, our peak detection algorithm that is used to construct a time series of IPIs is a graphical-based software that identifies peaks based on amplitude and width criteria. These criteria depend on and are optimised for the dataset undergoing processing. Baseline drift (DC shift) was subtracted using windowed moving-average or high-order FIR (with hamming window) filters. Scatter plots, equivalent to Poincaré sections, were constructed by plotting one IPI versus the next. Implicitly in our presentation and discussion, all IPIs have units of time expressed in seconds.

Recall that our first-return plot is a Poincaré mapping, in this case using intervals as a state variable. Thus, the system's 'flow' through state-space is only monitored through a slice or plane that intersects many trajectories (see Fig. 1.8). This allows us to understand the dynamics in the context of a difference equation (the map), representing a discretized version of the dynamics on the Poincaré section, and not a differential equation that describes continuous change in state-variables *via* a trajectory. We used an inverted second-order (nonlinear) polynomial to approximate the return plot constructed from the sequence of IPIs plotted against one another with $t = 1$ (see Eqn. 5). The function was selected empirically based on the common observation that the distribution of points in our return plots always resembled an L-shaped figure. Interestingly, this pattern is commonly observed in many return plots of nonlinear systems theoretical, physical, and biological.

$$IPI_{n+1} = \left[a(IPI_n)^2 + b(IPI_n) + c\right]^{-1} \equiv x_{n+1} = \left[ax_n^2 + bx_n + c\right]^{-1} \qquad \text{(Eqn. 5)}$$

A one dimensional-mapping function was obtained by approximating the scatter plot with our nonlinear equation. Fitting of the function we accomplished by using a standard nonlinear least-squares approximation, the Levenberg-Marquardt method (Press *et al.*, 1999), which attempts to minimize a least-squares-type of function though

successive iterations. Specifically, the value of χ^2, which represents the sum of the squares of the deviations of the theoretical curve from the experimental data points, is minimized. Thus, the scatter IPI plots were then approximated by the best fit to an algebraic equation (one-dimensional map). Once obtained, fixed-point and stability analyses of the mapping function were performed analytically according to classical methods in nonlinear dynamics as applicable to one-dimensional maps (Guckenheimer and Holmes, 1983; Berge *et al.*, 1984; Hoppensteadt and Izhikevich, 1997). Maple V software (Waterloo Maple Inc.) was used to solve differential and algebraic equations. Matlab (MathWorks Corp.) and Origin (Microcal Inc.) software packages were used for data conversion and analyses.

Given an analytical model for the return maps, we can now proceed to investigate specific dynamical behaviour within the state-space representation (Poincaré section) of the system. This is based on Takens' delay embedding theorem (Takens, 1981), as discussed previously, which briefly states that the attractor reconstructed by a time-delay plot of an observable (such as the IPI in our case) is equivalent to the original multi-dimensional attractor that portrays the system's dynamics. In other words, the time-delay map provides us with the basic information of the underlying dynamical regimes of the original system. The functional fit to the return map, where $IPI_{n+1} = f\ (IPI_n)$, where f is the selected inverted polynomial function that determines the one-dimensional map (see Results), can be considered to be a global nonlinear model of the dynamics (Decroly & Goldbetter, 1987; Hoppensteadt & Izhikevich, 1997). These maps are valuable tools because they allow for a discrete representation of the original time series that simplifies the mathematical study, in addition to providing a solid theory background that exists for the analysis of one-dimensional maps (Berge *et al.*, 1984; Pomeau & Manneville, 1980; Collet & Eckmann, 1980; Guckenheimer & Holmes, 1983; Hoppensteadt & Izhikevich, 1997).

The state-space of a system can undergo different kinds of topological changes based on alterations in critical parameters that influence state variables and bring about significantly different behaviours. Further, within the full state-space of a system there can exist more than one attractor and the nature of each attractor can change based on alteration of critical control parameters. Fundamentally, dissipative systems, such as the

brain, can possess four different kinds of attractors: (1) fixed point or equilibrium points, (2) periodic points, also known as limit cycles, (3) quasi-periodic attractors, and (4) chaotic or "strange" attractors. Note that the word "strange" refers to the deterministic nature of the chaotic behaviour – thus, reflecting on the meaning of chaos, which is different from random. Fixed points are states from which the system does not move, but these points can be stable or unstable. In the former case, perturbations will die out after some time, in the later case, they will grow due to the system's nonlinearity. Limit cycles are periodic in the time domain and are visualized as closed curves (i.e. orbits) in full state-space representations (see Fig. 1.8, e.g. epochs of highly rhythmic neuronal activity during seizures) – this form of behaviour is fundamentally linked to the 'evolution' of fixed points based on control parameter modification. Quasi-periodic points display more complex patterns in Poincaré sections and are visualized as a torus-shaped collection of non-intersecting trajectories in the full state-space. Strange attractors have a fixed, complicated, and highly characteristic geometry, where nearby trajectories on the chaotic attractor move apart or together at exponential rates – a measure of this rate is the Lyapunov exponent.

There are many analyses and applications for return maps. These include but are not restricted to, analysis of stability for fixed points, searching for so-called Unstable Periodic Orbits (UPOs) of greater than period-1 order, and quantification of state-space invariants such as Lyapunov exponents. In this study, we restrict our analysis to stability of fixed points in $t = 1$, or first-return maps, whose fixed points correspond to period-1 orbits. We are particularly interested in these fixed points, firstly, due to their ease of identification and check for stability (see Fig. 2.6). Secondly, from their relevance to seizure-like activity, which can be considered as transient stabilization of periodic meta-stable states. Finally, their identification and analysis have demonstrated practical usefulness for control of complex systems behaviour: in cardiac systems (Christini & Collins, 1996; Garfinkel *et al.*, 1992; Christini & Collins, 1997), and mammalian brain (Schiff *et al.*, 1994; Le Van Quyen *et al.*, 1997; Di Mascio *et al.*, 1999). For a demonstrated application of fixed-point stability analysis on exclusively EEG recordings in the context of seizures and transient stabilization of meta-stable states, see Perez Velazquez *et al.* (1999).
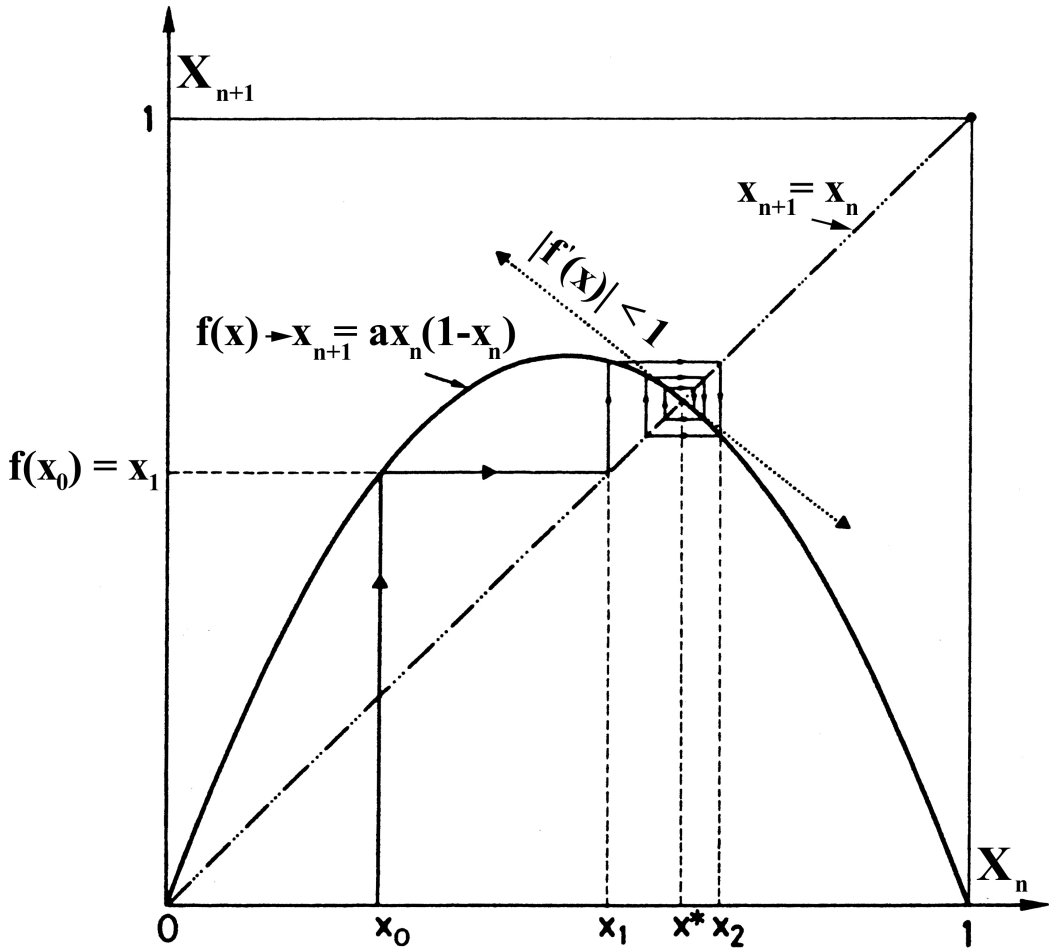
Figure 2.6. Illustration of fixed point stability analysis for the logistic function, $f(x) \circ x_{n+1} = ax_n (1-x_n)$, for $a = 0.7$. It is evident that any point on $f(x)$ that intersects with the identity line ($x_{n+1} = x_n$) is a fixed point of f – thus, its own iterate. With this description, both the origin and the point x^* are fixed points. However, for any given initial starting point on the map (e.g. x_0), subsequent iterates (i.e. x_1, x_2,...,x_n) , move away from the fixed point at the origin, deeming it to be an unstable fixed point. Note the arrowed lines represent iterations of the map. Graphically, this is accomplished by starting at an initial value, (x_0), and drawing a line to the value of the function at that point $f(x_0)$. This value is now the next x-coordinate and for this reason we draw another line from this point to the identity line, from where we repeat the process monitoring for convergence of solutions. In this case, there is an attracting fixed point at x^* and the iterations ultimately converge there for any initial starting value. Note that this behaviour is completely governed by the system's dynamics, which sensitively depends on the value of the control parameter [a] due to the nonlinear nature of the system. For other larger values of [a], for example $a = 4.0$, iterates do not converge to a single value and indeed result in chaotic behaviour. The stability of the fixed point, x^*, is determined by the absolute value of the slope at that point. If $|f'(x^*)| < 1$, then x^* is stable, if $|f'(x^*)| > 1$, then x^* is unstable.

In Figure 2.6 we illustrate the method by stability of fixed points on first-return maps (limit cycles as viewed from Poincaré sections) can be determined. In essence, this technique makes use of a linear stability analysis, which is limited to terms of a first-order perturbation analysis (Berge *et al.*, 1984). The basis of this stability analysis lies in Floquet Theory, which states that in order to determine the stability of a periodic solution (e.g. limit cycle), we need to look at how the system responds to small initial displacements away from the fixed point (P_0) after one-period. Consider a nonlinear (autonomous, no direct dependence on time in equations describing system) flow in an m-dimensional state-space, which has a periodic solution of period T – after one period one returns to the same initial point:

$$\bar{X}(t+T) = \bar{X}(t) \qquad\qquad \text{(Eqn. 6)}$$

In order to find out if this solution is stable or not, we need to consider what happens when a small displacement $\boldsymbol{d}\bar{X}$ away from the solution is caused. This is achieved by linearizing the flow about the periodic trajectory; we can consider this operation for an explicit state-space (representation) such as a Poincaré section, although it need not be limited to any particular larger number of dimensions.

$$M = \left[\frac{\partial T}{\partial x_i}\right]_{x_i^0} \quad i = 1,2. \qquad\qquad \text{(Eqn. 7)}$$

Where, M is the so-called Floquet matrix that approximates the Poincaré section, T, to first order. The eigenvalues of the matrix M determine stability of the trajectory after m periods, for the case we are discussing this would mean for $m = 1$.

$$T^m(P_0 + \boldsymbol{d}) - P_0 \cong M^m\boldsymbol{d} \qquad \|\boldsymbol{d}\| \to 0 \qquad \text{(Eqn. 8)}$$

Thus, the result can be approximated as the product of the matrix and the perturbation $\boldsymbol{d}$. If the result of the displacement (perturbation) results in an exponential decrease in

time, eigenvalues of M are all modulus less than one and contained in unit circle of complex plane, then the periodic trajectory is linearly stable about the fixed point P_0. The case in contrast would be when M has at least one eigenvalue with modulus greater than one – then the displacement will grow exponentially in time and the limit cycle can be considered to be unstable. It is important to note that this exponential divergence does not continue without bound and is limited by the nonlinear deterministic nature of the system under study. Further, the matrix M always has an eigenvalue equal to one, which is the trivial solution that corresponds to a displacement d along the direction of the trajectory $\bar{X}$ resulting in a return to the initial point in one period. This case does not tell us anything about stability. Aside from the Floquet method, an alternative method that has some practical value in a heuristic-type experimental scenario is a variation of parameters approach. Once a fixed point has been identified, we can cause a variation of parameters to obtain a neighbouring flow. The argument here is that if a stable flow exists, any closely neighbouring flow will also have a limit cycle. This property, overall, increases the probability of finding periodic activity in nonlinear systems. It is important to again note the dependence and relation between the value of system control parameters and the existence and stability of fixed points (see Fig. 2.7).

A periodic solution that becomes unstable is accompanied by a bifurcation that sensitively depends on the value(s) of critical control parameters governing the system. In other words, whenever the solution to an equation or system of equations changes qualitatively at a fixed value of critical system parameter(s), then it can be regarded as a bifurcation. If we now consider a two dimensional space, with one dimension being the incremental values of a control parameter and the other axis, the number of solutions at that control parameter, such a plot is referred to as a bifurcation plot. Simply stated, bifurcation points represent sudden changes in dynamics as caused by alterations in control parameter values at critical points. The concept of bifurcations is a powerful one in that it allows for direct interpretation of system behaviour, in terms of control parameters and solution of system dynamics, with association to the fixed points in the system and their evolution to other attractor types with changing parameters.
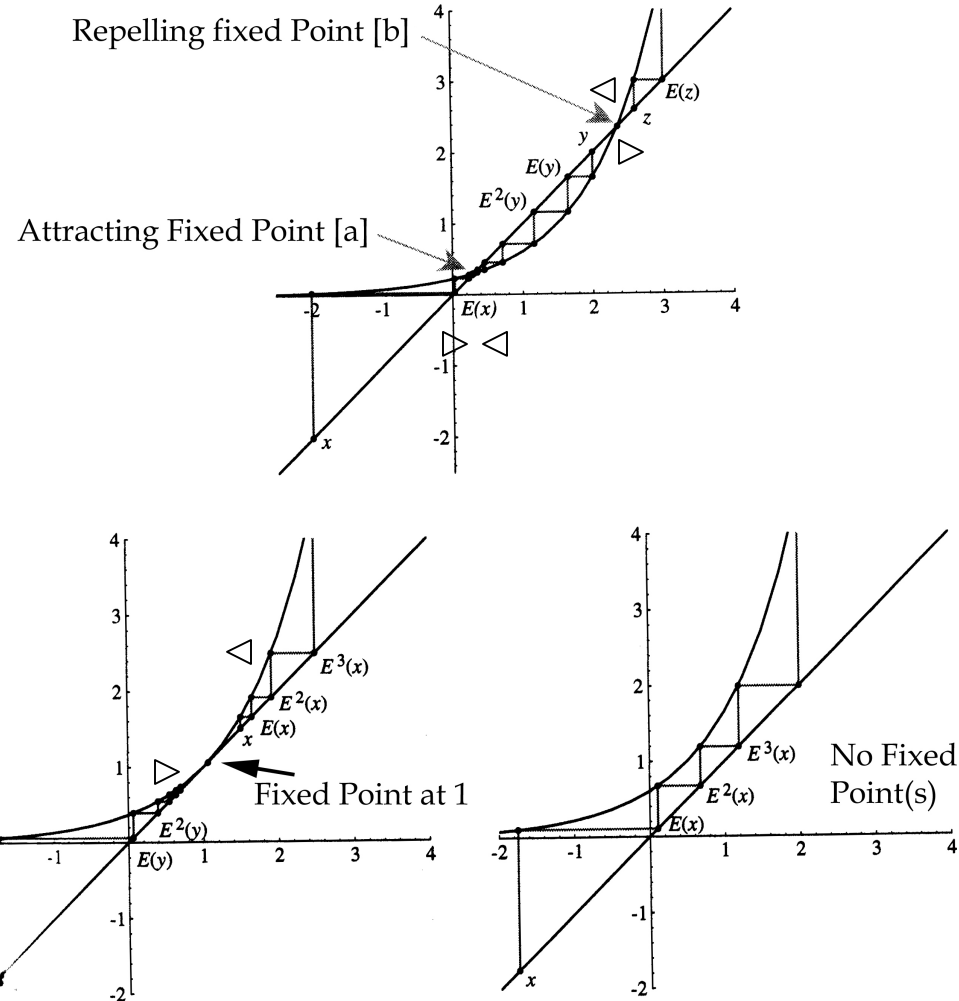
Figure 2.7. Illustration of changes in system parameters and their influence on state-space behaviour and dynamics. For all the above figures, the curves represent a function, from the family of functions with the form $E_c(x) = e^{x+c}$, where c is the control parameter. Specifically, there exists a bifurcation point at $c = -1$, where the system as defined by the equation experiences sudden change in dynamics with different solutions. (Top) For $c < -1$, there are two fixed points, one stable (attracting), the other unstable (repelling). (Left) For $c = -1$, both fixed points are fused into one fixed point at $x = 1$. (Right) For $c > -1$, no fixed points exists in the system. Note that in each plot, the graphical technique of iterating the map, as explained in Fig. 2.6, clearly illustrates the behaviour of the system under the influence of fixed points given some initial starting value. The hollow arrowheads point to the direction of convergence (inspired in part from Holmgren, 1996).

We previously discussed the stability of identified fixed points. We proceed to further investigate the role of these fixed points in the context of specific dynamical regimes, in the context of bifurcations. Fixed points whose derivatives are not equal to one in the absolute value, $|f'(x_c)| <> 1$, are important and have specific names – they are referred to as *hyperbolic* fixed points. For reasons explained earlier, fixed points whose derivates are, $|f'(x_c)| < 1$, in value are said to be attracting, and those fixed points with, $|f'(x_c)| > 1$, are said to be repelling. If the derivative of the map at a fixed point is 1 or −1, then it is called a *non-hyperbolic* or *neutral* fixed point (Guckenheimer & Holmes, 1983). In our study of the pre-ictal period leading to seizures, and based on our past-experience with EEG recordings (Perez Velazquez *et al.*, 1999), we are most interested in the phenomenon of intermittency. There are three types of intermittency, each representing, fundamentally, forms of dynamical regimes that provide a route for transition between periodic and chaotic states and back again – with all transitions governed by changes in control parameters at bifurcations points. Only specific types of bifurcations lead to the different types of intermittencies : (1) saddle-node bifurcation → Type I intermittency, (2) sub-harmonic {supercritical} bifurcation → period doubling cascade, also, sub-harmonic {subcritical} bifurcation → Type III intermittency, and (3) Hopf {supercritical} bifurcation → Quasi-periodicity, also, Hopf {subcritical} bifurcation → Type II intermittency. Detailed reviews of the explicit meaning and tests for identifying each of these bifurcations and their consequences can be found in Berge *et al.* (1984) and Guckenheimer & Holmes (1983).

In order to maintain a focused description of the methodologies employed in the context of the results (to discussed in section III), we will limit our discussion to the identification and characterization of *sub-harmonic* or so-called *flip bifurcations* as described by Guckenheimer & Holmes (1983). Such a bifurcation evolves from a non-hyperbolic fixed point, at $x = x_c$ for some control parameter value $I = I_c$ that satisfies,

$$\frac{\partial f}{\partial x}(x_c, I_c) = -1 \qquad \text{(Eqn. 9)}$$

In our case, we have obtained *f* from our one-dimensional mapping function, x_c, from the intersection of the map with the identity line, and we assume that our Poincaré section is 'stationary' for whatever system control parameter (a non-experimental observable) that is governing the dynamics. Equation 9 refers to a condition that must be met for the slope on the map at the fixed point. We can then evaluate for the type of flip bifurcation, supercritical (normal) or subcritical (reverse), by evaluating the Taylor expansion of the mapping function about the fixed point. Specifically, we can determine the stability and direction of bifurcation (see Fig. 2.8) using orbits of period-2. This was accomplished by composing the mapping function with itself $(f \circ f)$, and looking for a non-zero cubic term at the bifurcation point, equivalent to stating,

$$a = \frac{1}{6}\frac{\partial^3 (f \circ f)}{\partial x^3} \neq 0 \qquad\qquad at\,(x_c,\boldsymbol{I}_c) \qquad\qquad \text{(Eqn. 10)}$$

which is further equivalent to the following expression,

$$a = \left(\frac{1}{2}\left(\frac{\partial^2 f}{\partial x^2} \right)^2 + \frac{1}{3}\left(\frac{\partial^3 f}{\partial x^3} \right) \right) \neq 0 \qquad\qquad at\,(x_c,\boldsymbol{I}_c) \qquad\qquad \text{(Eqn. 11)}$$

If the value for *a*, as evaluated at $(x_c,\boldsymbol{I}_c)$ is *a < 0*, then the bifurcation is subcritical and will lead to Type III intermittency. If *a > 0*, then the bifurcation is supercritical and will result in a sub-harmonic cascade.

In summary: (1) we construct a first-return map (equivalent to a Poinecaré section) using interpeak-intervals with specific interest in the pre-ictal epoch, approximately 20 – 60s before start of SLEs, (2) next, we approximate the map using an inverted polynomial, (3) we then solve analytically for fixed points and use linearization to check for stability and further identify the type of bifurcation with the aim of characterizing the dynamic regimes which underlie the observed behaviour.
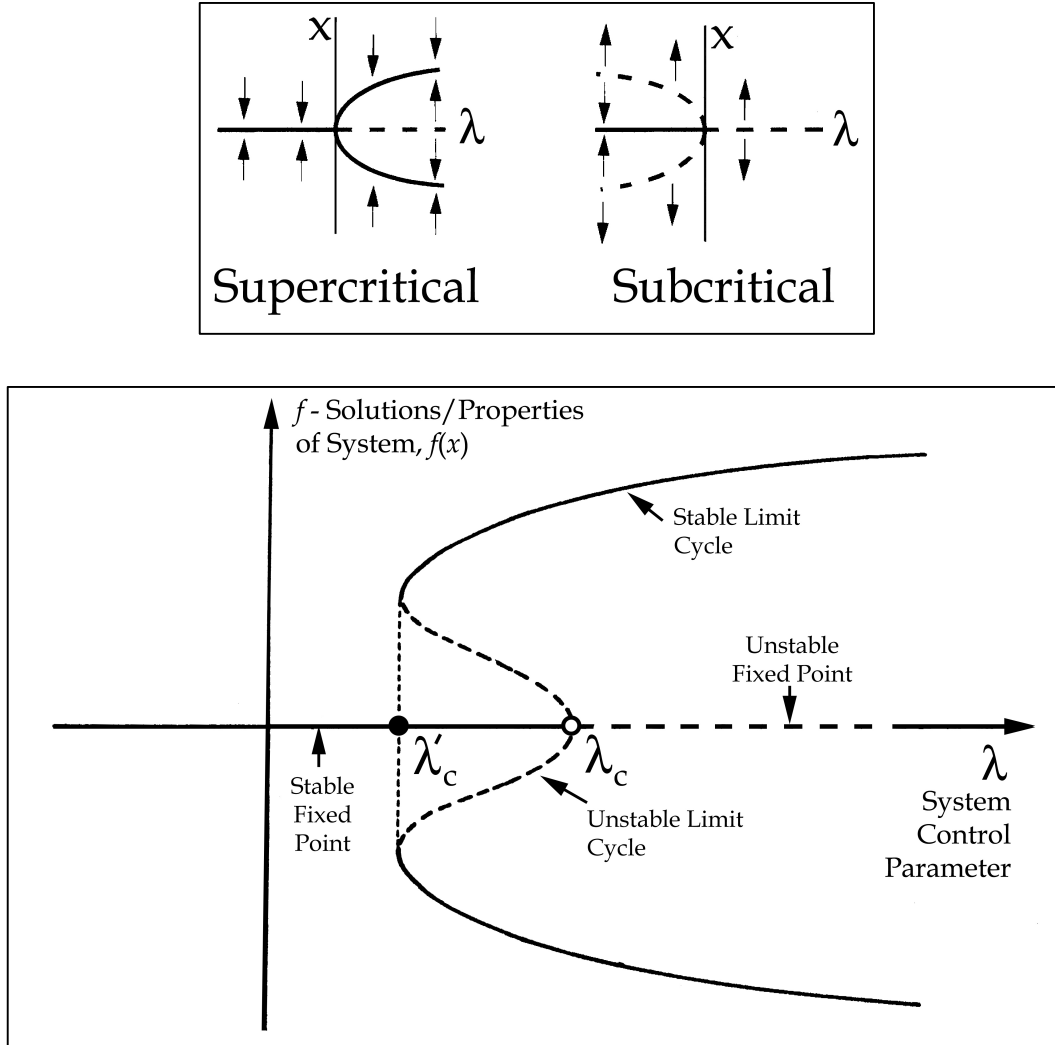
Figure 2.8. Schematic diagrams of supercritical and subcritical bifurcations. Bifurcation plots: the x-axis corresponds to the change of the control parameter, λ, and solutions to the system's dynamical differential/difference equation are plotted on the y-axis. This allows for direct visualization of state-space topological changes as governed by control parameters. (Below) An example of a subcritical or reversed bifurcation. In this case, the system's nonlinearity amplifies instabilities, which becomes unstable a finite distance from the stable solution at the bifurcation point (hollow circle), at control parameter λ_c. In a subcritical bifurcation, the system, once unstable as defined by the unstable fixed point, gives rise to an unstable limit cycle along with a stable fixed point (see vertical dashed line, area covering λ'_c to λ_c). Thus, stability gives rise to an unstable periodic solution along with a stable fixed steady-state solution. Practically, both solutions are not observable at the same time. (Inset, above) Simple examples of supercritical and subcritical bifurcation points. Note the axes and the direction of the arrows indicating the stability of the different solutions for range of control parameters. In the case of a supercritical bifurcation, a stable limit cycle loses stability and gives birth to another stable limit cycle – having approximately double its period. Due to this, the supercritical bifurcation is often referred to as the period-doubling bifurcation.

III Results

3.1 Visualization, Detection, and Anticipation

3.1.1 RPT Analysis of Brain Slice Recordings

Our data set comprises of a selection of 27 complete seizures, recorded from the CA1 cell layer of the hippocampus. These recordings were obtained from 8 brain slices (~ 3 seizures/slice) exhibiting spontaneous recurrent seizure-like events (SLEs) in low [Mg^{+2}] ACSF. A complete record is considered to included interictal, preictal, and ictal periods (Fig. 3.1). The epoch following the end of the ictus is considered to be the interictal period of the next complete record. In this model of epileptogenesis, an SLE is manifested through putative network-driven mechanism(s) that transform the epileptiform field event (EPSP-like, see panel 1, Fig. 3.1), to a preictal state where multiple population spikes override the field EPSP (see panel 2, Fig. 3.1), culminating with the SLE. The ictal state as defined by the start of SLEs, marked by increase in the frequency of field events, typically faster than 2 Hz, with waveforms that are negative deflecting, sharp in morphology, believed to be population spikes reflecting synchronous firing of many neurons (see panel 3, Fig. 3.1). Records were selected in a manner to represent the observed diversity in the duration of different signal components (i.e. preictal, ictal). A typical complete record was ~ 3 min. (range = 4.7 min.) in duration, with an average duration 1.8 min (range = 4.2 min.) for the combined interictal/preictal period. The SLE or ictal period was on average 0.8 min. (48s, range = 2 min.).
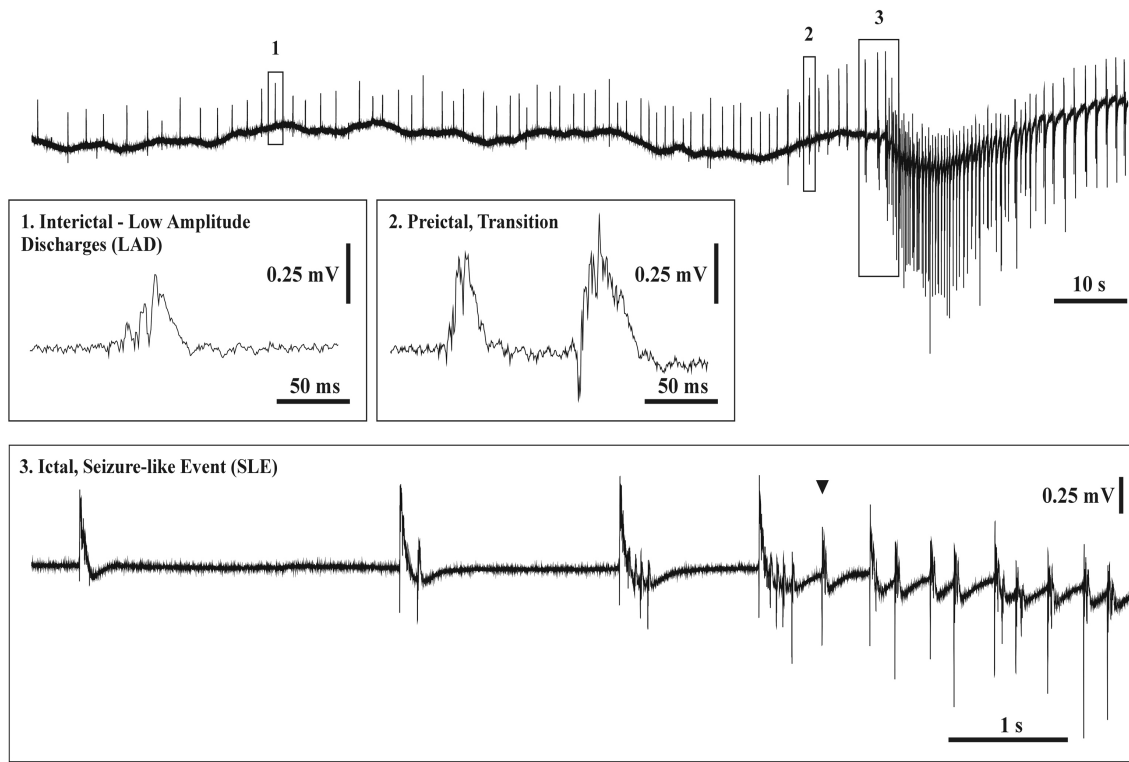
Figure. 3.1. Extracellular field recording from CA1 layer of a horizontal hippocampal slice in low [Mg^{+2}]. Seizure-like events (SLEs) occur spontaneously and reoccur every 3 to 10 min. A typical recording is composed of distinct interictal, preictal, and ictal epochs. **(1)** The interictal period is characterized by ~ 0.5 Hz activity with EPSP-like fields with some overriding fast population activity. Typically, there exists a period of quiescence (baseline-only) before the appearance of LADs as part of the interictal period (not shown). **(2)** The preictal or transition epoch is characterized by a prolonged, often multiple, broad EPSP-like events with overriding polymorphic sharp-waves. **(3)** The SLE begins (▼) with a characteristic polarity flip of the EPSP-like field activity with a frequency generally faster than 2 Hz. Increased number of overriding fast transients are also observed with frequencies up to ~ 300 Hz.

RPT analysis was performed on the field recordings (see Fig. 3.2). The range of durations recorded for interictal/preictal periods allows for a thorough analysis of differences between these two 'states' and the SLE. For a particularly long duration of continuous interictal activity, lasting ~ 4.7 min. (see Fig. 3.2a), three visualizations are provided: (see left panel, Fig. 3.2a) recursive map of successive IPIs reveals 4 periodicities of the interictal activity with two period-1 clusters along the diagonal representing short-short *(IPI$_n$, IPIn+1)* and long-long recursive IPI values. The long-short and short-long clusters represent transitions into and out of the fast events (up to ~ 200 Hz). These events override the interictal waveforms (see panel 1, Fig. 3.1). FP and aFP analysis results of the long-duration interictal activity reveal subtleties in the manner in which successive IPIs evolve in time. The FP vs. time plot (see top right panel in Fig. 3.2a) displays two characteristic features that are consistently observed during the interictal period: (1) most of the FP values are near zero and hence represent IPI pairs that map onto high magnitude regions of the FP surface. This re-enforces the choice of the selected surface in order to amplify fast transient events corresponding to neuronal population events. (2) The asymmetry along the diagonal (identity) line of the return plot (see left panel in Fig. 3.2a) is visualized in time by a slightly larger number of positive FP deflections relative to negative; this relation is reversed during the preictal period. The plot of aFP vs. time (see lower right panel in Fig. 3.2a) shows that in general, the interictal period is quantified by small persistent magnitudes of aFP with very few large amplitude transients. The dark line is a 15-point smoothing of raw aFP values (shown as grey line) over time and the plot's logarithmic range is limited to 0.1 – 1 for clarity of display. Both FP and aFP plots have a threshold limit (dashed line), which is set to the average FP and aFP values as calculated for the ictal state that follows this preictal trace. Figure 3.2b is an example of analysis performed on an ictal segment. This particular sample recording was selected due to an interesting epoch within the SLE, between $t = 50 – 71$ s, where the ictal waveform transiently begins to resemble preictal activity in frequency and waveform (marked by double-ended hollow arrows, see Fig. 3.2b). A plot of IPI vs. time (see left panel in Fig. 3.2b) visualizes the rapid changes that occur in successive IPIs during an ictal event. The initial segment of seizure is characterized by a logarithmic shortening of successive IPI as marked by the top solid

arrow in lower-left panel of Figure 3.2b. This is followed by the appearance of many successive short IPIs with multiple periodicities, visualized by a dense cluster of points and marked by the lower solid arrow. This progresses into the epoch that resembles preictal-like activity. Note that both FP and aFP plots (double-ended hollow arrows, right panels in Fig. 3.2b) decrease markedly during this epoch, thereby exemplifying their sensitivity as quantifiers to successive high frequency IPI transients that are epileptiform. Ahead of this epoch, the recorded activity returns to more ictal-like waveforms and both the FP and aFP plots increase abruptly in value as expected for a seizure-like event. The plot of IPI vs. time (see lower left panel in Fig. 3.2b) suggests the presence of at least three different periodicities that are confirmed visually by constructing a return map of IPIs with $t = 3$. In this visualization, period-3 points align themselves along the identity line. Since the IPI data are extracted from a biological system and not from an analytical solution there is considerable scatter for all visualized periodicities as inherent in life-system that are know to posses intrinsic variability.
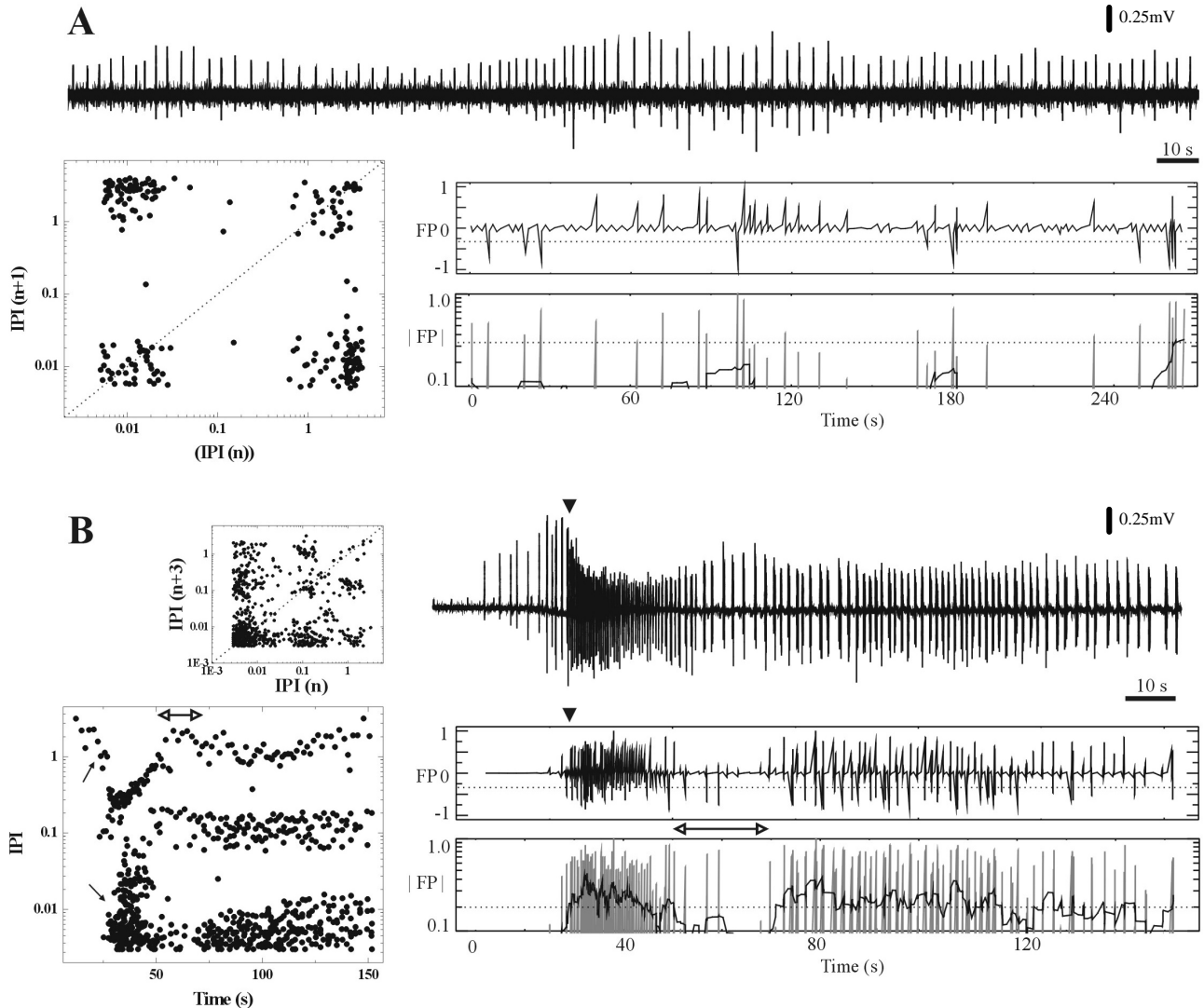
Figure 3.2. RPT analyses of interictal and ictal extracellular field recordings. **(A)** A long segment of spontaneous interictal activity. (left panel) Recursive IPI plot displays the existence of four distinct periodicities. (top right panel) FP values are generally small in magnitude, including multiple long duration intervals with some transient short intervals visualized as peaks. Note the asymmetry of large amplitude FP events about the zero line. Threshold line (dashed line) set to average FP/aFP value of seizure that followed the interictal activity. (lower right panel) aFP plot with brief transients. No prolonged elevated aFP above threshold is observed. **(B)** Transition into a seizure-like event (SLE, ▼) both FP and aFP plots (right panels) display frequent, large amplitude transient activity with prolonged elevated aFP values throughout the SLE. Between $t = 50 - 71s$ (š, left and right panels) the ictal activity resembles interictal/preictal activity resulting in decreased amplitude of both FP and aFP quantifiers. (arrows, lower left panel) Transition to the SLE is characterized by logarithmic shortening of successive IPI values – semilog for visualization. (upper left panel) Recursive log-log plot shows the presence of higher order, period 3 periodicities as clusters of points about identity line, using $t = 3$. All IPIs in units of seconds.

RPT analysis is also useful for visualizing and quantifying the transition to seizure. The FP vs. time plot (see Fig. 3.3a) visualizes the time-varying projected trajectory of the slice towards an SLE. A brief interictal period develops to a preictal state at which point a detected asymmetry in successive IPI pairs (relative to the identity line) is visualized as recursive, downward deflecting, and large amplitude FP values. Enhanced frequency of downward deflecting, large amplitude FP events during the immediate preictal period is consistently observed in slice recordings with variation in number of events and their time of occurrence relative to SLE onset – deviations are greatest among different slices. In this case, these characteristic FP features appeared with persistence ~26 s (s) before SLE onset (▼). The threshold marker (see dashed line, Fig. 3.3a) is set at the average FP/aFP value during the ictal event (onset at solid arrow, see Fig. 3.3a). An aFP plot was constructed for another seizure of greater duration. A relatively active interictal period (postictal state of a prior seizure) progresses to the preictal state and into seizure (see Fig. 3.3b). The gray line represents actual aFP values while the solid line corresponds to a 15-point smoothing. The progressive rise in aFP is seen at the initial, exceptionally active, interictal segment of the record, which becomes persistent in the moments leading up to the seizure event. The smoothed aFP curve (see solid line, Fig. 3.3b) quantifies the increase in frequency of fast transient waveforms that become recurrently present during the preictal state. The horizontal threshold line corresponds to the average aFP value for the ictal segment (starting at solid arrow, see Fig. 3.3b). The smoothed aFP trace (solid curve) surpasses this threshold ~ 22 s before (s) the onset of seizure (▽). Large amplitude deviations in aFP (or FP) correspond to short-short IPIs that are mapped on to the 'peak-region' of the FP surface (see Figs. 2.4 and 3.3).

In order to quantify possible range of detection sigmas (thresholds) as calculated automatically by the described algorithm for slice extracellular recordings, above baseline (AB, $n = 97$) and below baseline (BB, $n = 88$) detections were performed on a large number of complete recordings (i.e. interictal to ictal). For AB, autosigma was calculated to be $s = 2.4 \pm 0.7$ (avg:stdev, range = 3.9) and BB sigma $s = 3 \pm 1$ (range = 5). Greater degree of variation was observed for BB detections as a result of analyzing complete records, where most interictal/preictal waveforms are maximal AB resulting

in total events detected BB to be more variable. In order to improve sensitivity in cases where IPIs are used as input to other NTSA methods, interictal/preictal recordings should be analyzed AB and BB for ictal segments. Nonetheless, when considering real-time implementation, an overall AB detection exhibits adequately sensitivity in detecting electrographic signal changes (see Fig. 3.3).
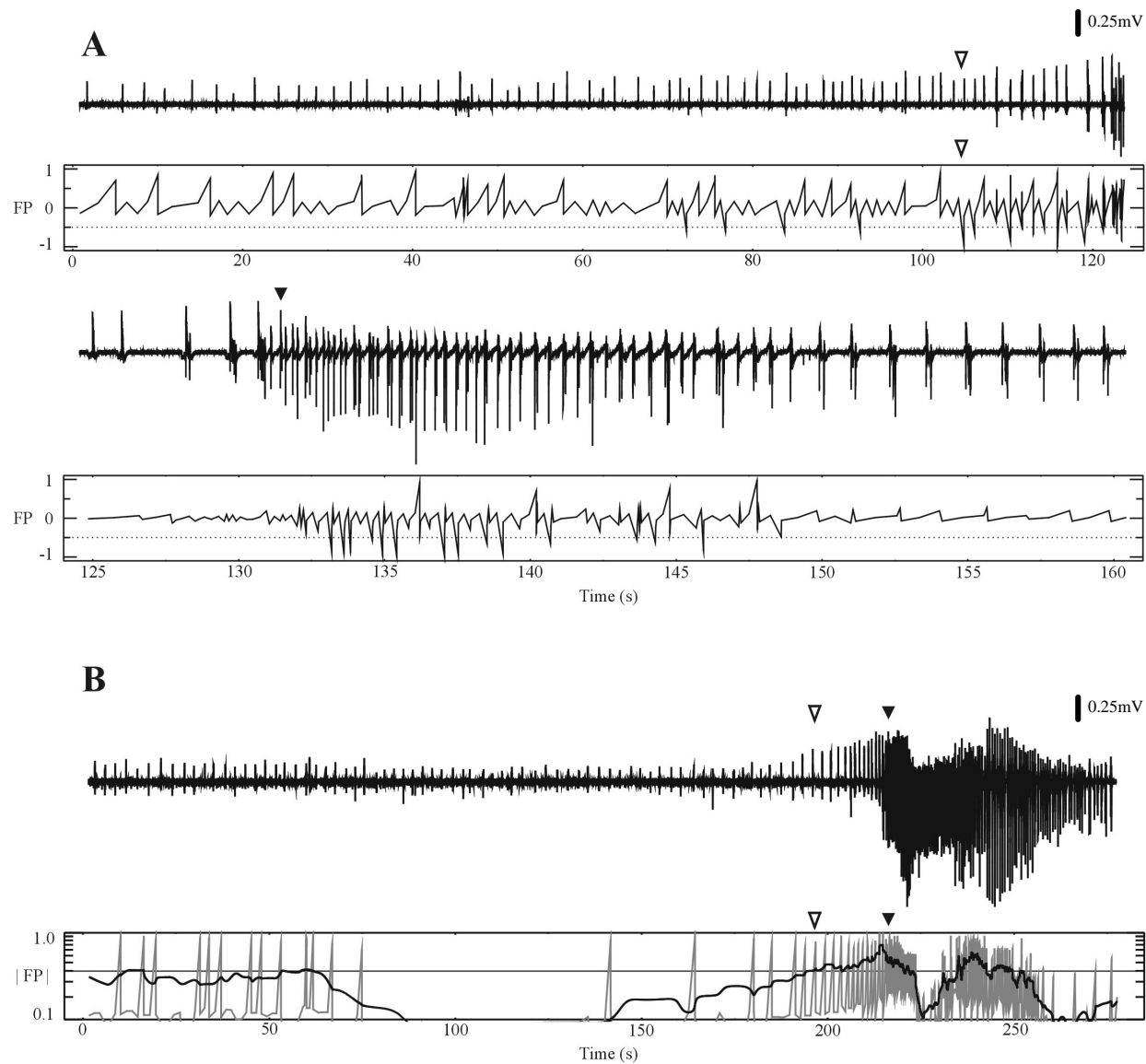
Figure 3.3. RPT analyses of two complete extracellular field recordings with transitions from interictal, to preictal, and ictal states. **(A)** FP plot of temporal development of successive IPIs towards the seizure state (▼). Note the revealed asymmetry in the temporal sequence of IPIs (greater number below identity line) that results in upward deflecting large amplitude FPs. These become recurrent downward deflections in an epoch (~ 26 s, ▽) before SLE manifestation (▼). This is observed in 70% of slice recordings. SLEs are always characterized by predominately downward, large amplitude, and recurrent FP deflections. Threshold (dashed line) set to average during the ictal period. **(B)** aFP plot of interictal period progressing to an SLE. The early component of this recording is moderately active, possessing multiple fast transient field activity, giving rise to elevated aFP values ($t \sim 0 - 75s$). Smoothed aFP values (solid line) show electrographic changes as early as $t = 150s$, surpassing the SLE threshold (average aFP during SLE) at approximately $t \sim 22$ s (▽) before SLE onset (▼).

3.1.2 RPT Analysis of Intracranial EEG Recordings

We contrasted analysis performed on brain slice recordings with EEG in order to explore possible similarities in temporal evolution of seizure activity and to characterized limitations of the analysis. Intracranial EEG recordings of seizures were obtained from implanted depth electrodes in two patients; $n_1 = 16$, $n_2 = 4$ respectively. Recordings from the first patient (P1) were mainly seizure recordings with the interictal/preictal period lasting ~1.4 min. (range = 0.81 min.). Typical seizure epochs lasted ~2.6 min. (range = 1.5 min.). Long duration continuous interictal recordings were mainly obtained from the second patient (P2) (mean ~ 6 min.). A typical depth-electrode recording of interictal activity developing into a seizure is shown in Figure 3.4. Start time of seizures were determined by visual inspection of the EEG (Dr. Wennberg) for consistency. A long-duration recording of interictal activity was recorded and analyzed using RPT. Recursive plot was generated for the entire record (hollow circles, left panel, Fig. 3.5a) with one half of the record visualized by FP and aFP plots (see solid circles left panel and two right panels, Fig. 3.5a). A recursive IPI plot, with $t = 5$, was generated in order to emphasize the distribution of successive IPIs (mostly long-long intervals) and also the existence of higher order quasi-periodicities (cluster of points on identity line, left panel, Fig. 3.5a). The right panels of Figure 3.5a display small amplitudes for both FP/aFP quantifiers. The interictal state is characterized by an overall absence of frequent fast transients. Smoothed aFP values (see solid line, bottom right panel, Fig. 3.5a) display very little responsiveness to the detected events. This record (from P1) is strictly an interictal data segment and emphasizes the technique's ability to discriminate between interictal/preictal, and ictal waveforms. In the case of human data, it is more difficult to define a definite preictal epoch since there is considerable heterogeneity amongst patients and their seizure phenomenology. In Figure 3.5b, the transition from interictal/preictal to ictal is visualized by a recursive plot (left panel) and FP/aFP quantifiers (right panels). The recursive IPI plot, with $t = 3$, displays a shift in the distribution of successive IPIs and reveals an overall more periodic signal. This is visualized by clustering of points about the identity line, suggesting period-3 regularities.
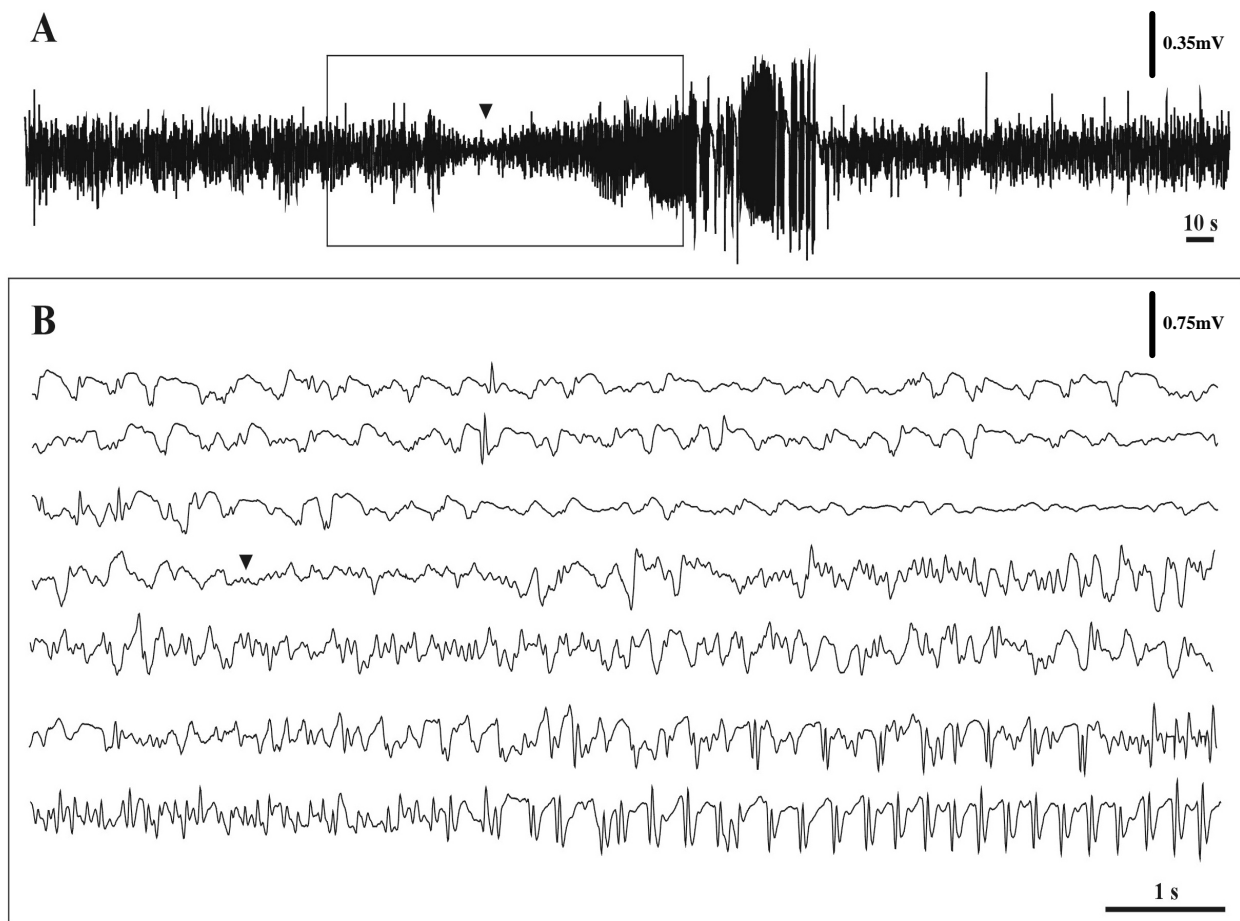
**Figure 3.4.** Intracranial depth-electrode EEG recording from a patient with mesial-temporal lobe epilepsy. **(A)** An Electroencephalographer identified electrographic seizure onset for comparison with RPT analysis. **(B)** Electrographic onset (▼) is manifest by an initial dampening of background activity, followed by the emergence of low amplitude, high frequency activity that develops to polymorphic spike and wave discharges.

The FP-time plot, as in the case for slice recordings, exploits potential asymmetries in the distribution of successive IPIs relative to the identity line. Retrospective analysis reveals definite electrographic changes ~ 30s before (marked by flat-ended line, see Fig. 3.5b) the start of the seizure (▼). Note that a similar asymmetry is detected, as in the slice data, with regards to the temporal evolution of successive IPIs; a plot of aFP visually exemplifies this observation. Elevated aFP values are present persistently close to the beginning of the record, suggesting that electrographic changes had already occurred (see lower right panel, Fig. 3.5b). This further demonstrates the difficulty in declaring a particular section of data as clearly preictal; especially in the case of patients with active focal/multi-focal seizure disorders. The threshold (dotted line, right panels, see Fig. 3.5b) level was set to the average FP and aFP values during seizure-only epochs respectively. Analysis results for four seizures recorded in the same day from P1, with very similar durations and waveform morphology were superimposed to reveal any consistent temporal trends leading seizure onset (see Fig. 3.5c). The upper panel does not display a significant or persistent alteration of the FP value preictally. A plot of aFP reveals a persistent increase in magnitude ~ 40 s before the average start time of seizure. This suggests that the frequency of short interval IPIs does exhibit a persistent change pre-seizure, but that the asymmetry in the distribution of IPIs does not follow a reproducible temporal order.
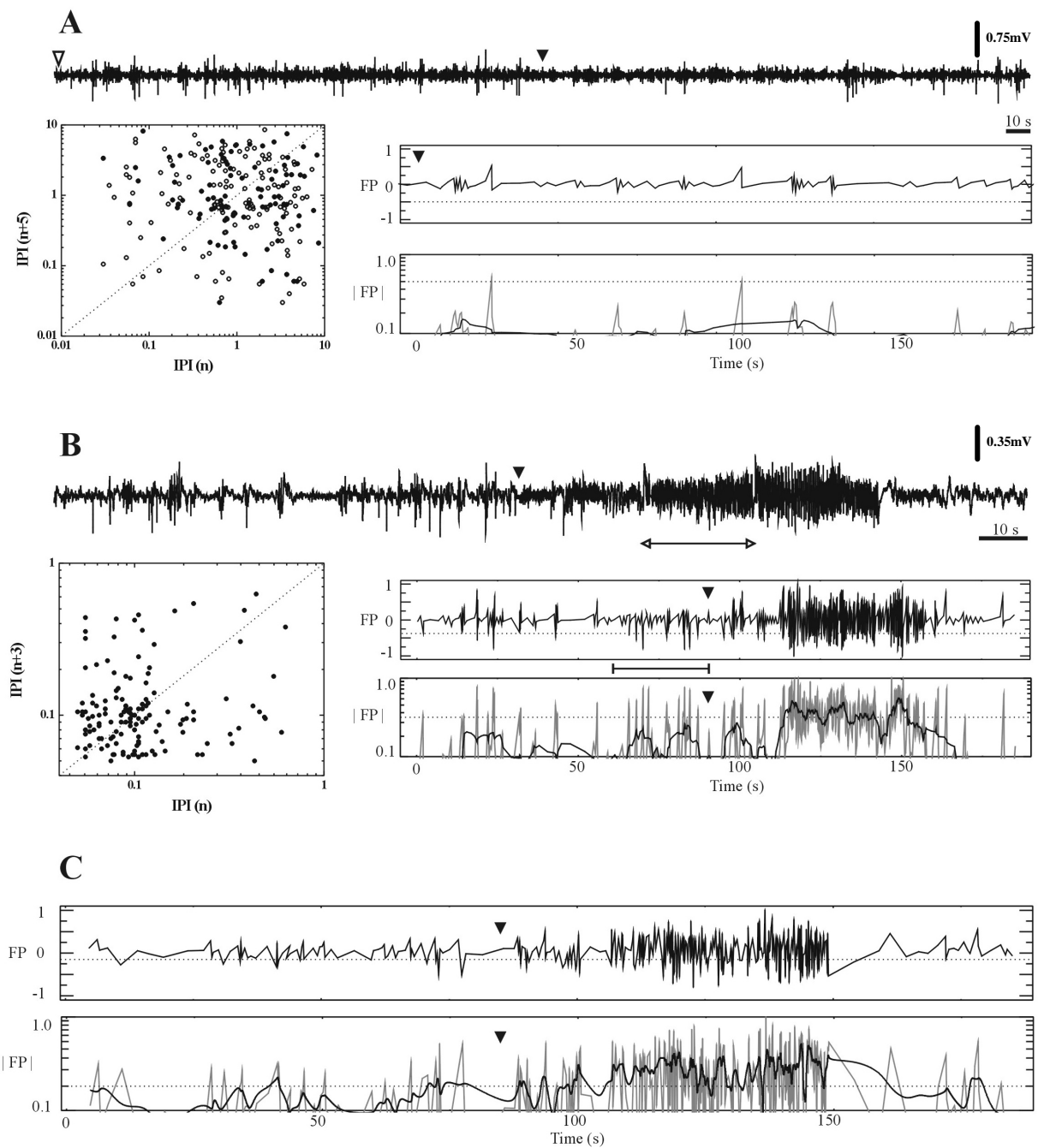
Figure 3.5. RPT analyses of depth-electrode EEG recordings: interictal (patient 1) and preictal-to-ictal transitions (patient 2). **(A)** (left panel) Recursive plot ($t = 5$) of a long-duration interictal segment. The overall distribution of IPIs (O, starting at ▽) reveals predominantly long intervals with high-order periodicities visualized as a cluster of points about the identity line. A segment of the recording (●, starting at ▼) is visualized and is also quantified by FP/aFP plots. Both FP and aFP display low magnitudes during interictal/preictal periods with few, un-sustained, large amplitude FP/aFP transients. **(B)** Transition from preictal activity to an ictal event. (left panel) recursive IPI plot of a segment within the ictus (marked by š) with short-short period-3 intervals. (right panels) FP plot reveals persistent asymmetry in successive IPIs with short durations ($t = 60\text{-}95s$) ~ 35s before electrographic onset (▼). Plot of aFP exhibits greater sensitivity to fast transients that appear greater in number before the seizure. **(C)** FP and aFP plots of four superimposed recordings. Asymmetry in FP plot (upper panel) is lost through averaging due to variations between seizures. Using aFP quantifier, which does not discriminate about the identity line, sustained aFP values occur ~ 30 s before seizure onset (▼). FP and aFP magnitudes normalized relative to max value in each trace.

3.1.3 Possible Anticipation of Seizures

The detected peak events that correspond to short-short IPIs do not necessarily originate from large amplitude features in the original recording. In fact, they mainly correspond to low-amplitude fast transients that override the preictal EPSP-like field response (e.g. panel 2, Fig. 3.1), satisfying both amplitude and width peak detection criteria. For 27 complete field recordings from 8 slices, starting interictally and proceeding to an SLE, FP/aFP quantifiers were able to detect electrographic changes, 44 ± 33 s (avg:stdev) in anticipation of the actual seizure-like event (Fig. 3.6). Approximately 75 % of detected anticipatory events occurred within 50 s of SLE onset.

For 16 complete depth electrode recordings FP/aFP quantifiers were able to detect electrographic changes ~ 29 ± 13 s (avg:stdev) in anticipation of electrographic onset (Fig. 3.6). Approximately 75 % of detected anticipatory events occurred within 30 s of electrographic onset. For the EEG records analyzed, sigma was auto-selected on average to be $s = 2.06 ± 0.28$ (n = 20). This value is much closer (relative to the slice data) to the 'theoretical' expectation ($s = 2$) from a Gaussian distributed signal that is over-sampled.
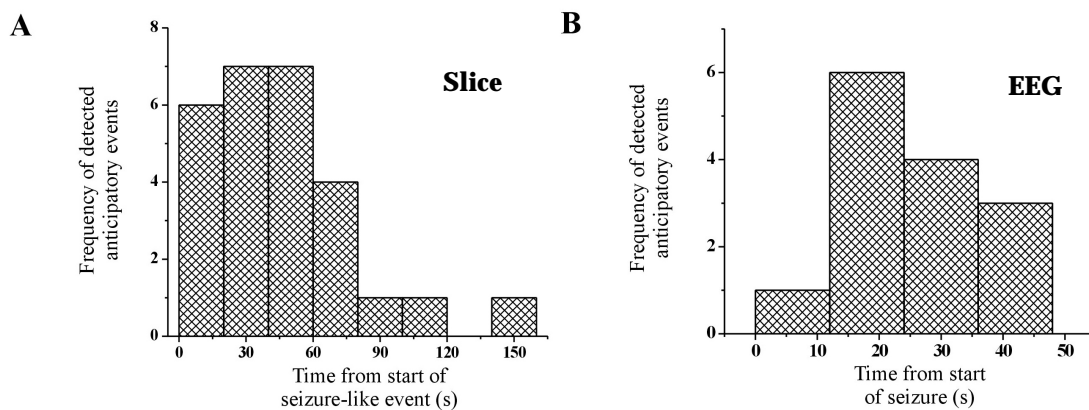
Figure 3.6. Distributions of seizure anticipation time determined using RPT analysis performed on extracellular brain slice and patient EEG recordings. In this retrospective study, seizure anticipation was defined as the time when FP/aFP quantifiers took on persistent, large amplitude (negative for FP) values that satisfied a threshold defined as the average value during the ictal epoch **(A)** Anticipation for slice recordings occurred ~ 44 ± 33 s (avg:stdev, sem = 6 s) with ~ 75% of the anticipatory events occurring within 50 s to the SLE. **(B)** Anticipation in human EEG recordings resulted in times of ~ 29 ± 13 s (sem = 3 s) with ~ 75% of events occurring within 30 s of electrographic onset.

3.2 Dynamical Regimes of Spontaneous Activity in Hippocampal Slices: Implications for Control

Under our recording conditions, > 90% of the hippocampal slices display spontaneous interictal activity (see Fig. 3.7), and in 47.6% (30/63) of those, this activity develops into SLEs (see Fig. 3.8). The SLEs in these slices are characterized by high frequency bursts (10-30 Hz) with relatively high interburst frequency (2-8 Hz) at the start, which becomes lower towards the end of the SLE (see Figs. 3.8 - 3.10). The bursting activity suddenly disappears for a few minutes, possibly representing post-ictal depression, and then interictal activity resumes, which will eventually result in another SLE (see Fig. 3.11 for consecutive recordings).

To determine the dynamics of the transition to seizure, we use recursive or first-return plots, a time-delay embedding technique (Berge *et al.*, 1984; Takens, 1981; Sauer, 1994, also see Introduction), where the system's dynamics is simplified by reducing its dimension. This is achieved by constructing one-dimensional return maps (Berge *et al.*, 1984). The time-delay embeddings extract information about the topological structure of the attractor and the underlying dynamics (Packard *et al.*, 1980).

We measured extracellular field potentials in the CA1 or CA3 areas and used the time interval between successive peaks as our state-variable (Sauer, 1994), and constructed the first-return interpeak-interval (IPI) scatter plots by plotting IPI_{n+1} versus IPI_n (See Fig. 3.7 - 3.10 and 3.12), as described previously (Perez Velazquez *et al.*, 1999). These plots can be considered as Poincaré sections (Le Van Quyen *et al.*, 1997), and rests on the fundamental principles of Takens embedding theorem as discussed previously (see Introduction). This method allowed for the identification of the dynamical regime involved in the transition to the SLE and facilitated the selection of an appropriate perturbation (electrical stimuli described below) in order to avoid the transition from interictal to seizure development. In this time-delay representation, periodic behaviour appears as a fixed point (or steady state) located on the bisectrix, or identity map where $IPI_{n+1} = IPI_n$.
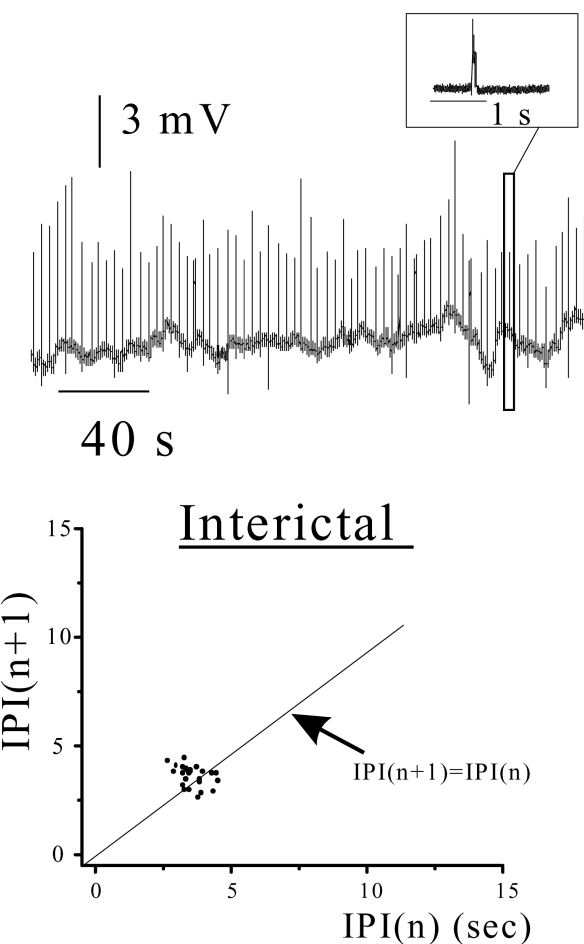
Figure 3.7. Spontaneous interictal-like activity in the hippocampal slice. The trace corresponds to a field recording in the CA1 layer, in a slice that did not exhibit SLEs. The first-return inter-burst interval plot of spontaneous interictal activity is shown below. Note the cluster of points at ~0.3 Hz (3-4 seconds), indicating that the activity in this slice had a periodic low-frequency firing steady state. This periodic activity persisted throughout the recording period (~1 hour).

Inspection of the interictal activity, observed in slices that did not exhibit spontaneous SLEs (52.4% of the slices, 33/63), revealed a low frequency component with an average frequency of 0.35 ± .15 Hz (range 0.13-0.55 Hz) representing the dominant population rhythm with some high frequency components (10-25 Hz) present within each population event. This regular, periodic activity, is represented as a cluster of points near the identity map (See Fig. 3.7), and is termed limit cycle in dynamical terminology. While ideally only one point on the diagonal would be expected for the rhythmic population activity, the cluster of points is due to variability in the biological preparation, as opposed to solutions obtained by solving a system composed of precise analytical expressions.

The cluster of points indicates that the activity of these slices has a stable limit cycle, also inferred from the sustained, long-term bursting activity at the specific frequency, as shown in the field potential recording of Figure 3.7. However, the transition to the SLE is characterized by a more continuous plot with short-to-long intervals (See Fig. 3.8 and 3.10), long between the bursts and short between the peaks on each burst (see inset in Fig. 3.8 for details of ictal events during an SLE). Multiple peaks (normally 2) were also observed on the interictal bursts and hence the short-long sequence that is evident, for example, in return plots of Figures 3.9 and 3.12a and 3.12c. The IPIs for the pre-ictal state preceding the SLE are distributed along an underlying L-shaped curve (see Figs. 3.8 and 3.10). This distribution can be modelled by a recursive relation, that produces a return map $IPI_{n+1} = f [IPI_n]$, where f is the function that determines the one-dimensional map (Fig. 3.10) and can be considered to represent a global nonlinear model (see Methods). The nature of the scatter plot corresponding to the transition from interictal activity to the SLE is suggestive of the presence of low-dimensional dynamics (Garfinkel *et al.*, 1992; Braun *et al.*, 1997). The obtained plot can be best approximated by a nonlinear least-squares fit of the scatter plot (Perez Velazquez *et al.*, 1999) as described in Methods, to an inverted polynomial, $y = \left(ax^2 + bx + c\right)^{-1}$, where *x=IPI*, which best represents the one-dimensional mapping function *f* and defines the difference equation $IPI_{n+1} = \left(aIPI_n^2 + bIPI_n + c\right)^{-1}$.
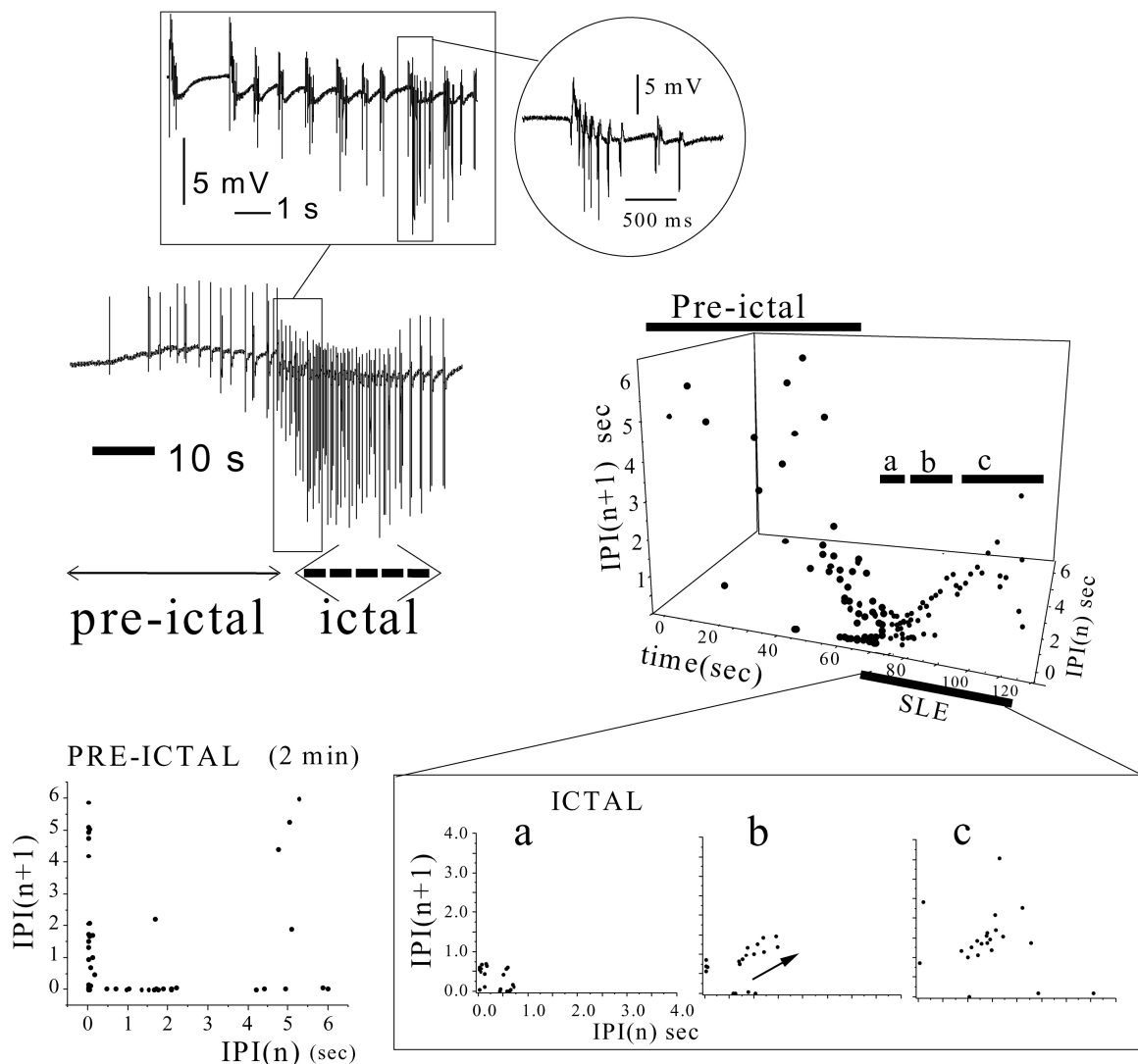
Figure 3.8. Spontaneous transition from interictal to ictal (seizure-like) activity *in vitro*. (Above) Field potential recording in the CA1 layer showing the transition between pre-ictal activity and the spontaneous SLE (ictal). Insets depict details of ictal burst events. (Below) First-return interpeak interval (IPI) scatter plots of 2 minutes of pre-ictal activity (left graph), and the SLE ("ictal", each graph corresponds to the labelled epochs within the SLE, *a*, *b* and *c*, each about 12 seconds of activity). Note the progression of the IPIs on the diagonal in b and c, marked by an arrow, characteristic of intermittency. The three-dimensional scatter plot reveals the temporal evolution of the successive IPIs.
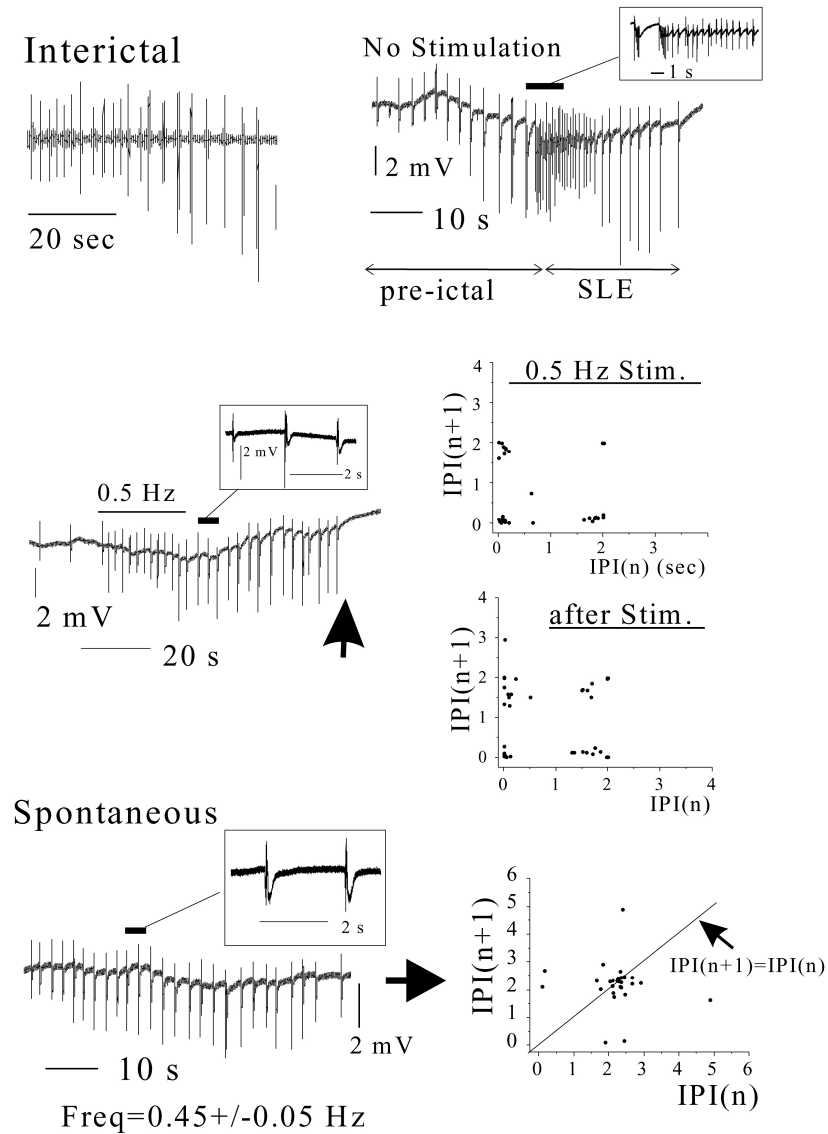
Figure 3.9. Perturbation of the spontaneous activity in hippocampal slices. Periodic forcing at 0.5 Hz stops the transition to seizure. (Top traces) Field potential recording in the CA1 layer displaying the interictal activity at the beginning of the recording, that lasted 6-7 minutes before the recurrent appearance of SLEs. Note that the interictal activity started at low-frequency, 0.3-0.5 Hz, suggesting that this state could be forced to stabilize, as shown below. Right trace shows the spontaneous transition from pre-ictal to the SLE, in the absence of control stimulation. (Inset) Depicts the initial 8 seconds of the SLE, at ~3 Hz. (Middle traces) A 20-second 0.5 Hz control stimulation applied to the mossy fibres prevents the transition to the SLE, and the activity finally ceases (arrow at the end). The IPIs plots (right-hand side) show the clusters of points during periodic forcing (upper plot, clusters at ~2 seconds), and after the perturbation (Lower part). Notice that the activity continues at ~0.5 Hz after the 20-second perturbation. The points are not all situated on the diagonal because the peak detection algorithm detected two peaks in each field potential event (see inset traces), hence the sequence of intervals long-short-long (2 seconds-0.1 seconds). (Lower Plot), 5-7 minutes after the low-frequency perturbation, the spontaneous activity resumed in this slice, oscillating near the forced frequency (average 0.45 Hz). This slice did not have any other spontaneous SLE during the 1-hour recording period, even though these could be evoked by high-frequency trains.

One-dimensional maps have been used in other systems to study the dynamical regimes (Roux, 1983; Glass *et al.*, 1983; Decroly & Goldbeter, 1987). These maps are valuable tools because they allow for a discrete representation of the original time series that simplifies the mathematical study, in addition to the solid theory behind one-dimensional maps (Berge *et al.*, 1984; Pomeau & Manneville, 1980; Collet & Eckmann, 1980; Guckenheimer & Holmes, 1983; Hoppensteadt & Izhikevich, 1997). The 3-dimensional plots (see Figs. 3.8 and 3.12) allow for an appreciation of the temporal evolution of successive IPIs.
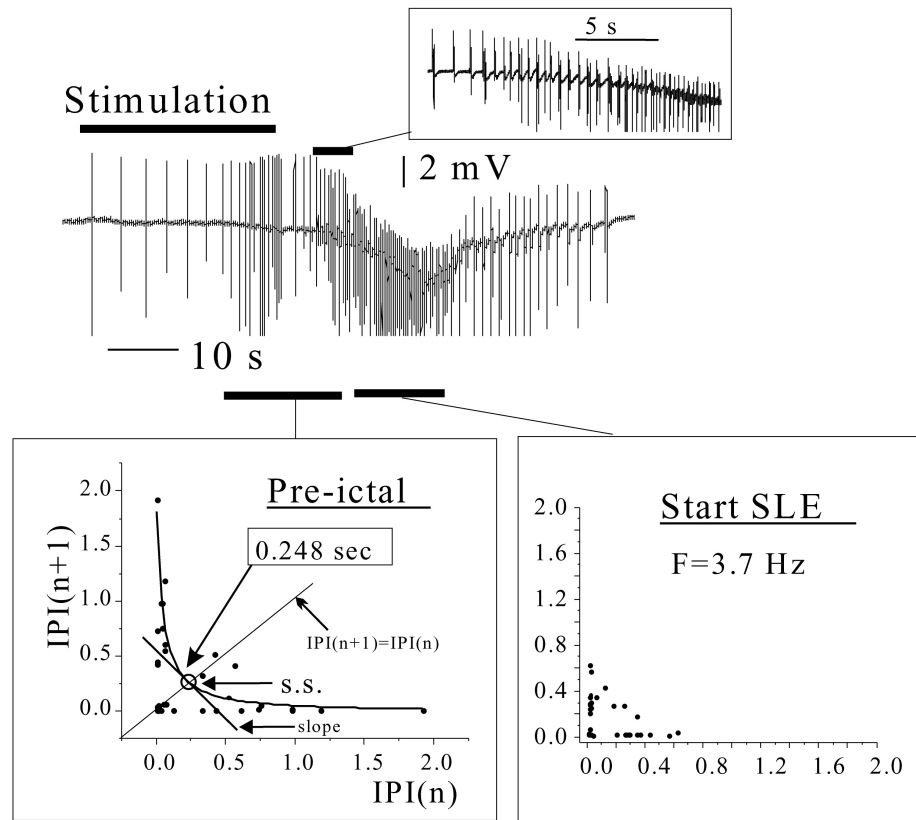
Figure 3.10. Induction of SLEs by mimicking the pre-ictal burst dynamics. (Top) Trace shows the perturbation in a slice that did not present spontaneous SLEs. In this case, reproducing the first-return IPI scatter plot of the transition to the SLE (as seen in slices that showed spontaneous SLEs) by a 25-second extracellular stimulation to the mossy fibres (notice this time the stimulation is aperiodic as we tried to simulate the spontaneous pre-ictal activity), the activity triggered an SLE. Note that the ictal event started after the stimulation was turned off (inset shows the beginning of the SLE). (Below) The pre-ictal IPI plot (using the IPIs for the 12 seconds preceding the SLE, shown by the black horizontal bar) shows the fitting of the scatter plot to an inverted polynomial $y = [ax^2+bc+c]^{-1}$, where $x = IPI_n$, $y = IPI_{n+1}$, and $a = 7.5$, $b = 12.3$, and $c = 0.58$. The steady state (S.S) is the crossing with the diagonal, at 0.248 sec (~4.0 Hz), and the slope at this point is ~ -1 (-0.98), indicating a meta-stable (flip bifurcation) state. The start of the SLE (right IPI plot, initial 15 seconds of the SLE) shows the high-frequency activity, with average of 3.7 Hz, that can be interpreted as the transient stabilization of the preictal flip point at ~4 Hz.

The stability analysis of the features of this mapping function reveals, initially, the presence of a fixed point, or steady state, representing high-frequency hypersynchronous neuronal firing, the SLE. As depicted in Figure 3.10, this fixed point can be determined geometrically by the intersection of the map with the bisectrix, or it can be obtained analytically from the mapping function: $x_{n+1} = \left(ax_n^2 + bx_n + c\right)^{-1}$, solving for $x_{n+1}=x_n$, which yields $x = 0.248$ seconds for the parameter values (*a*, *b*, and *c*) that best approximated the plot, shown in the figure legend. The slope of the map at this fixed point determines its stability (Berge et al, 1984) and in this case is close to -1 (-0.98), indicating the presence of a meta-stable state. A fixed point with these features is termed a sub-harmonic or flip bifurcation (see Methods). The concept of bifurcation is central in nonlinear dynamical systems theory, and can be interpreted as a change in the qualitative properties of the dynamics. This particular type of flip (sub-harmonic) bifurcation leads to type III intermittency or to a period doubling cascade, depending on a condition satisfied by the first terms of the Taylor series expansion of the map (see Methods). Specifically, if the expression $a = (\P^2 f / \P x^2)^2 / 2 + (\P^3 f / \P x^3) / 3$, results in, a < 0, then the flip is called subcritical and leads to type III intermittency (Hoppensteadt and Izhikevich, 1997). It was determined that type III intermittency is the dynamical regime underlying some human seizures (Perez Velazquez *et al.*, 1999). For the parameter values shown in Figure 3.10, the value of the above expression is less than 0 (*a = -0.69*), and therefore the flip bifurcation is subcritical, indicating that intermittency is the dynamical regime underlying these specific SLEs. Note also the progression of ictal IPIs on the bisectrix, in Figure 3.8, which is again suggestive of intermittency (Berge *et al.*, 1984; Hoppensteadt and Izhikevich, 1997). For other parameter values the flip may be supercritical. The main point to stress here is the presence of the bifurcation point that determines a change in the system's behaviour that could be responsible for the transition to the SLE. Thus, according to our interpretation, the SLE is seen as the transient (SLEs last 30-60 seconds under our conditions) stabilization of the meta-stable flip bifurcation point.

3.3 Periodic Pacing: Control of the Transition to the SLE

With the preliminary knowledge, mentioned above, about the dynamics of the transition to seizure, we explored the possibility that the transition to the ictal event could be perturbed and hence prevented. In this framework, seizures, or SLEs, can be thought of representing the transient stabilization of steady states of high frequency hypersynchronous firing of large neuronal populations. Hence we hypothesized that, by stabilizing another steady state, for example low-frequency firing as occurs during interictal activity (see Fig. 3.7), the occurrence of the SLE could be avoided. As mentioned, an almost equal number of hippocampal slices (53%) exhibited spontaneous interictal activity (0.35 ± 0.15 Hz) that did not develop into an SLE. This strongly suggested to us the presence of a low-frequency interictal-like stable state, that could be forced to stabilize, thereby altering the activity away from SLEs in hippocampal slices under these conditions. We therefore endeavoured to stabilize the putative interictal-like steady state, using brief periodic forcing stimuli, in order to avert the transition to the SLE in slices capable of spontaneous seizure-like activity. We performed an empirical study, where we systematically evaluated the efficacy of several different perturbation paradigms in their ability to disrupt SLE development by enforcing interictal-like activity. The effectiveness of perturbations was evaluated with both spatial and temporal considerations. We evaluated these paradigms at two different locations in the hippocampal circuitry; mossy fibers and Schaffer collaterals. Further, we investigated the timing of the stimulation in relation to 'natural' progression of the spontaneous activity from interictal to ictal. Specifically, we compared (1) early perturbation, upon observing interictal activity, (2) perturbation during the transition to SLE, versus (3) late perturbation, at a time when transition to SLE has been established.

Considering all this information, we applied, in slices that had SLEs, brief (20-50 seconds) low-frequency (0.5 Hz) electrical stimuli to the mossy fibres, in order to force the interictal-like state (see Fig. 3.9). The intensity of the extracellular stimulation was the minimal needed to evoke a population spike recorded in the CA1 area. The result of this perturbation is shown in Figs. 3.9, 3.11, and 3.12. The transition from interictal to ictal activity was aborted by a 0.5 Hz perturbation in 7 of 9 slices, in 68% (19/28) of the times (significantly different with a 99.9% confidence level, $p < 0.001$, as compared with unperturbed slices, χ^2-test). The success rate was lower when other frequencies were tried: 22.2% at 0.3-0.4 Hz ($p < 0.05$), and no control was achieved using less than 0.3 Hz. Similarly, higher frequencies, in the range 0.8-20 Hz, had no effect (4% success rate, 1/25, $p = 0.78$) or triggered SLEs. Random or white noise stimulation was equally ineffective (10%, 4/37, $p = 0.56$). When the stimulation/perturbation was applied to other hippocampal areas (Schaffer collaterals, entorhinal cortex), no control was ever achieved ($n > 25$). Another important variable is the intensity of the stimulation applied to the mossy fibres (range 200-800 μA), that had to be the minimal sufficient to evoke a field potential in the CA1 area, otherwise no control could be accomplished ($n = 20$). In general, the evoked synaptic responses were not attenuated by our short low-frequency stimulation: the average amplitude of the evoked response at the end of the perturbation (20 to 50 seconds) was 96.6 ± 4.7% of that measured at the start. Hence, synaptic depression may not account for the observed effects.
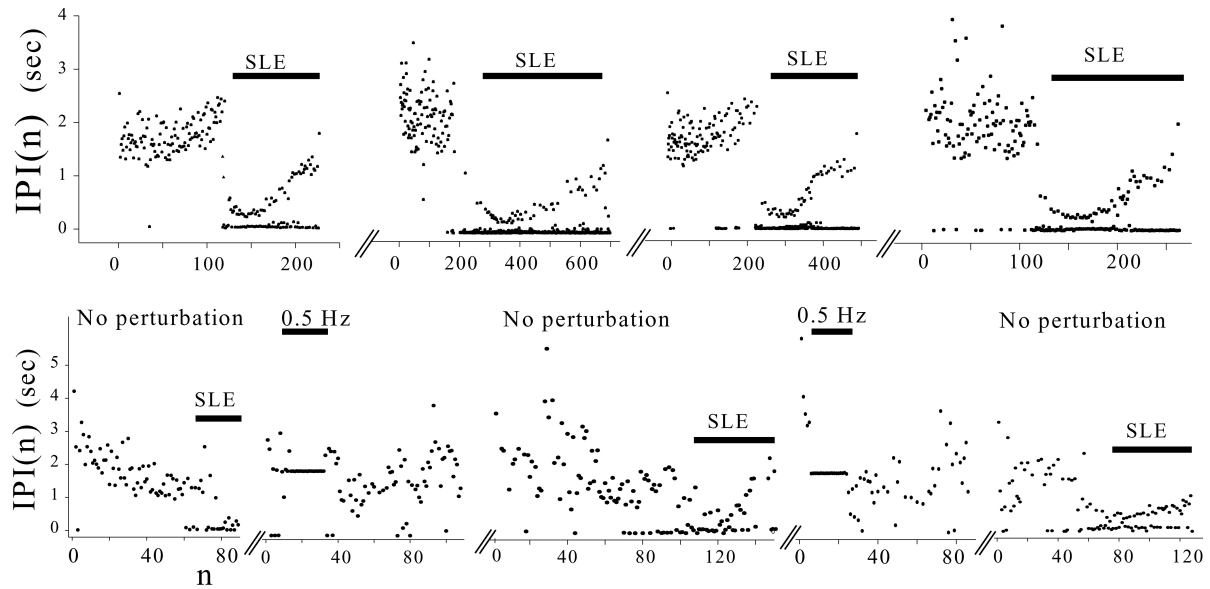
Figure 3.11. Control of the transition to the SLE by low-frequency periodic forcing. Graphs represent IPIs versus the peak number (n), corresponding to the continuous spontaneous activity in a slice that had SLEs. (Upper row) Shows four successive transitions from pre-ictal to SLEs. Note that the IPIs become smaller at the start of the SLE and gradually increase during its progression. (Lower row) Five successive recordings in another slice demonstrating that 0.5 Hz periodic forcing stimulation stops the transition to the SLE. Left plot ("No perturbation"), typical transition to the SLE, the IPIs becoming shorter. Next, stimulation at 0.5 Hz aborts the transition to the SLE. No perturbation following the previous success results in another SLE. Periodic, low frequency (0.5 Hz) stimulation, aborts again the transition. Following this, no perturbation results in another SLE.

Successful control was also a function of the timing of the perturbation. Specifically, during the time when the spontaneous pre-ictal activity had a frequency ~0.5 Hz (see Fig. 3.12) control was achieved more predictably. The effect we have described can be called periodic forcing of the neuronal activity. We interpret it as the forced stabilization of a meta-stable state representing low-frequency interictal activity, thereby successfully avoiding the transition to the SLE, which without perturbation, occurs *via* the stabilization of the flip fixed point. Indeed, the first-return IPI scatter plot of slices that presented interictal activity without spontaneous SLEs (see Fig. 3.7) had similar features as those corresponding to the successful "control" by our perturbation shown in Fig. 3.9 and 3.12a. It is important to stress the point that, by "adequately timed" perturbation, we mean that the start of the perturbation should be when the spontaneous interictal activity is close to the frequencies around 0.5 Hz, as it does not seem to be related to the timing relative to the start of the SLE. For example, in unsuccessful attempts, the timing of the start of the low frequency forcing relative to the SLE onset had a wide range, between 12 and 110 seconds (average 46 ± 27 s, $n = 40$).

While brief low-frequency forcing was able to halt the transition to the SLE, we could also trigger SLEs in slices that did not present them spontaneously, by re-creating the first return IPI plots as observed in slices with spontaneous SLEs, corresponding to the pre-ictal activity leading to the SLE (as in Fig. 3.8). This is demonstrated in Figure 3.10, where the scatter IPI plot during and immediately after the stimulation is approximated to the mapping function mentioned above. Analysis of this one-dimensional map reveals the existence of a flip bifurcation point at ~ 4Hz, as described above. The SLE starts with an inter-burst interval near 4Hz. Hence, by re-creating the dynamics of the transition to seizure we were able to trigger the SLE.
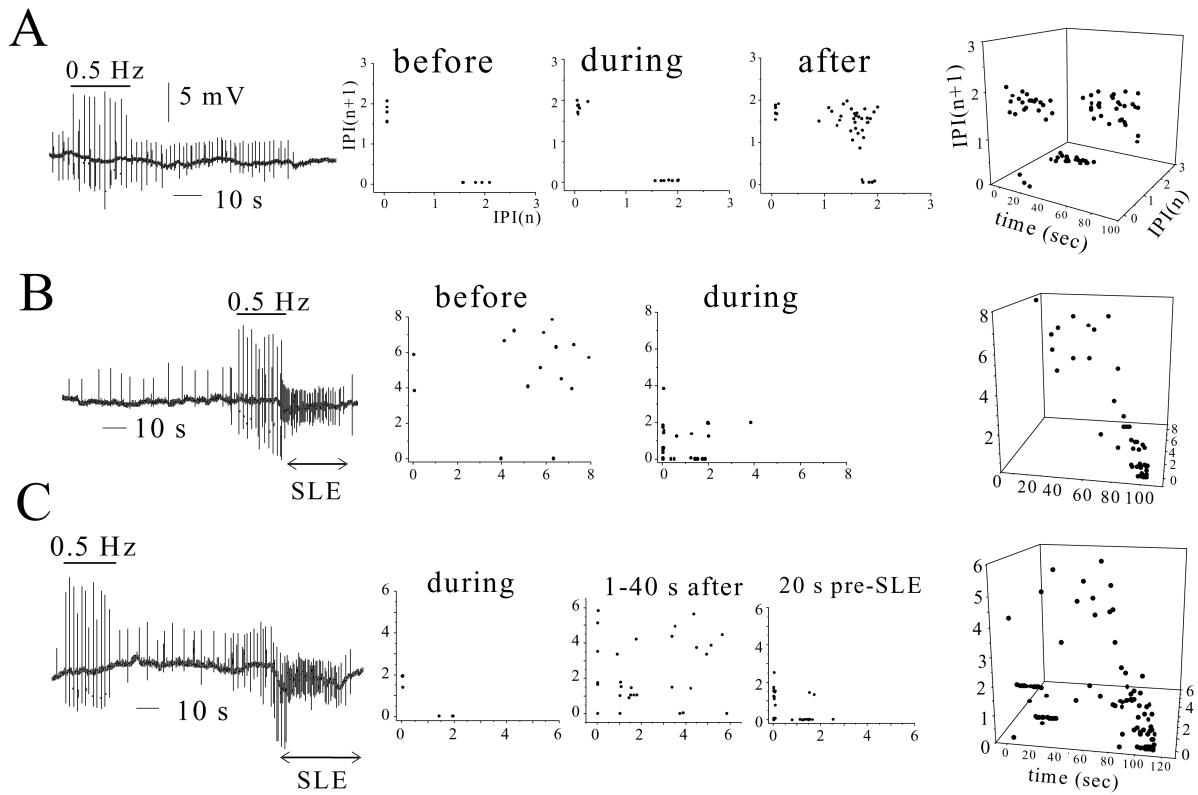
Figure 3.12. Timing of the low-frequency perturbation is crucial to stop the transition to seizure. **(A)** Field potential recording in the CA1 layer showing that low-frequency forcing (0.5 Hz) stops seizure occurrence if applied at the time when the spontaneous pre-ictal activity is near that state, as depicted in the left-hand side IPI scatter plot ("before"), just prior to the perturbation. Middle plot, forced activity during the 20-second stimulation, delivered to mossy fibres (clusters at 2 seconds). The activity continued after the perturbation at the forced frequency (right plot), with the cluster of IPIs around 2 seconds. The spontaneous activity ceased 50-60 seconds after the perturbation, as shown in the field recording on the left. The three-dimensional plot shown at the right-hand side depicts the time evolution of the IPIs. **(B)** Applying similar perturbation in the same slice when the pre-ictal activity was irregular and far from 0.5 Hz did not stop the occurrence of the SLE. The recursive IPI plots correspond to the activity before and during the stimulation. The three-dimensional graph depicts the appearance of the high-frequency activity that marks the beginning of the SLE. **(C)** Applying the 0.5 Hz perturbation (20 seconds, same location and intensity as in A and B) before the appearance of the pre-ictal activity does not stop the progression towards the SLE.

IV Discussion

4.1 RTP Analysis : Applications & Limitations

We used recordings obtained from an *in vitro* low-magnesium seizure model and depth-electrode EEG recordings, as time-series for the evaluation of a peak-detection method (RPT), which detects events based on amplitude and width (frequency) criteria. A methodology was developed for optimizing the trial-by-trial value of the detection parameters for any particular dataset. First-return plots were generated by plotting successive interpeak-intervals (IPIs), such that IPI_n is plotted vs. IPI_{n+1}. A method was developed for extracting the temporal evolution of successive IPIs by interpolating their position on the first-return map onto a three dimensional surface. A geometrical optimization strategy was used to 'tune' the responsiveness of the surface to different distributions of IPIs on a return map. This surface acts as a 'nonlinear amplifier' of IPI values, with greatest sensitivity to high frequencies or short intervals. It was observed that the occurrence of high frequency events, as detected by interpeak-intervals, had some anticipatory value with regards to impending seizures for both *in vitro* and EEG recordings. Further, these transient-high frequency events appeared to become more persistent during the pre-ictal period leading to seizure. Our study, although retrospective due to off-line analysis, found RPT to be a useful tool in complement of other methods, and conceptually it is simple with a non-intensive computationally load, thereby allowing for real-time implementation.

Nonlinear time-series analysis (NTSA) is an integral component of methodologies being applied to seizure-related electrophysiological signals with the aim of describing observables in the context of relevant quantifiers (Da Silva and Pijn, 1999; Lehnertz, 1999). Fundamental to NTSAs are concepts of embedding (state-space reconstruction), state-space stability, and invariant measures (see Introduction). When dealing with electrographic data in this context, much of the science is focused on space reconstruction from raw voltage values, with some studies using inter-event intervals as

state variables. In the later case, it is of critical importance that relevant events are detected using robust methods that are quantitative, optimization enabled, and not computationally intensive. This will facilitate application of such methods in clinically relevant environments to allow for further evaluation of electrographic changes that may exist in the epochs (both short and long timescales) leading to seizures.

A fundamental component of RPT analysis is the methodology used to identify 'relevant' peaks, which putatively represent population events. The occurrence of peaks in a recording is a variable parameter with great dependency on the type of recording, subject undergoing recordings, magnitude of 'noise', and sampling interval. Event detection in a signal is typically performed relative to some reference 'template event' or underlying assumption with regard to the data's amplitude distribution. In reality, we rarely have an accurate model for distributions of complex signals and typically impose a distribution on data with the aim that it is an adequate approximation. In this work we attempt to measure the amplitude profile of the signal, in the context of detected events, by successive peak detection runs at increasing threshold values from a zero baseline; a process we refer to as autosigma detection. We were then able to evaluate the differences and similarities between the approximated amplitude profile and a Gaussian assumption. In a real-time environment, sigma selection would be a learning algorithm, possibly in the form of an Artificial Neural Network (ANN) that would continually analyze a buffered window of data, with feedback to the detection parameters. Offline, for complete slice recordings, autosigma detection resulted in averaged $s = 2.4 \pm 0.7$ and $s = 3 \pm 1$ for detections performed AB and BB respectively (recall, amplitude threshold = $s = mp$, real number multiple p, multiplied by, mean absolute deviation, m). In the case of EEG, autosigma yielded a threshold value of $s = 2.06 \pm 0.28$. The case for a approximate $2s$ assumption is stronger for (complete) intracranial EEG recordings, since those data adhere more closely to a Gaussian assumption (in our records typically with $R^2 = 0.99$, $n = 20$). Overall, we found that even though our signals were not absolutely Gaussian in amplitude profile, events can be effectively detected (95% confidence) by thresholds that would be used for an over-sampled signal with Gaussian distribution. Over-sampled in this case means that the time scale of events of interest (e.g. field EPSPS, sharp waves, and other fast transients) are much shorter, by at least a factor of 5

– 10, than the time scale at which the signal is being sampled. Our subsequent analysis of a template slice recording at incremental levels of noise (see Fig. 2.3) demonstrates that even for slice recordings the optimal threshold, in the context of signal-to-noise, is maximal at approximately $s \sim 2$. Recall that the detection curve in response to baseline noise (see Fig. 2.3) was generated without assuming any particular type of distribution or absolute value for s but simply utilized the signal's own characteristics to measure the effect of noise. The observed peak difference between signal and baseline-only templates, suggesting optimality, at $s \sim 2$ is brought on by the fact that both signal and baseline-only templates had almost exact MAD values. Therefore, the amount of noise added was numerically correlated to multiples of MAD – the quantity by which all threshold detections (autosigma or other) are performed. It was observed for greater than 95% of the signals analyzed, that the sigma suggested by autosigma agreed with that selected by visual inspection. The width criteria was typically selected for a specific type of recording (i.e. intracranial EEG vs. slice fields) and maintained for almost all of the recordings analyzed within that category. Many trial runs displayed excellent agreement between analysis results and a range of values for $c \sim 5$ - 10, ($Dt = cT$, see methods). Moreover, this methodology can be used to generate a robust series of IPIs that can be used as input for other nonlinear time-series analyses (e.g. UPO identification), in real-time, to characterize and alter system dynamics (Schiff *et al.*, 1994; Christini and Collins, 1997).

The frequency potential surface (Eqn. 4, see Fig. 2.4c) was arbitrarily selected due to its topology and capacity to 'amplify' temporal relations between successive IPIs, mainly the short-short variety that correspond to fast transients. This concept is powerful for signal quantization since the surface can be made to be static or variable and can be of a different topography by selecting other functional forms (or numerical matrices). This flexible technique can be used to amplify and/or suppress different components of the IPI return plot in relation to experimental goals. The use of a nonlinear mapper is not limited to interpeak-intervals and may be applied to other time-series in a recursive sense (Akay, 2000). Note that a simple plot of time vs. IPI_n would not allow for such visualization or the quantification of positional relations to the

identity line. Moreover, the high frequency region of an IPI plot (e.g. see upper left panel, Fig. 3.2b) is typically very cluttered, rendering it almost impossible to quantify.

Several plotting strategies were employed for visualization of slice (see left panels, Fig. 3.2b) and EEG recordings (see Fig. 3.5). For slice recordings, a plot of IPI vs. time (Fig. 3.2b) clearly demonstrates the appearance of at least three quasi-periodicities that become manifest in the mid-to-late stages of seizure-like event. The pre-ictal state (see Fig. 3.2a) clearly differs from the ictal mainly due to the presence of multiple high frequency transients, visualized by extensive clustering of IPI pairs near the origin (see upper left panel, Fig. 3.2b). Quantification of continuous recordings with transition from interictal/pre-ictal states to SLE, using FP/aFP demonstrated two consistent findings: (1) In ~ 70% of slice recordings frequent, large amplitude negative deflections were observed in FP plots in an epoch near to the time of SLE onset (see Fig. 3.3a). (2) For all recordings, aFP values increase progressively over time towards an SLE. In this retrospective study, a threshold corresponding to the average FP/aFP value during the seizure-only segment of a complete recording was used to discriminate for electrographic changes relevant to seizure anticipation. Events relevant to seizure anticipation were declared to occur at an epoch corresponding to sustained or frequent FP/aFP values above the threshold level (see Fig. 3.3). Using these criteria SLEs were anticipated by ~ 44 ± 33 s (avg:stdev, see Fig. 3.6). A putative explanation for the observed deviation in anticipation times is due to the slices themselves. During horizontal sectioning few slices retain full hippocampal-parahippocampal circuitry and can incur differing levels of tissue damage, affecting intact circuitry, which can affect network properties and alter SLE dynamics. Analysis of depth-electrode EEG was able to distinguish clearly between interictal/pre-ictal and ictal states. Plots of aFP revealed clear electrographic changes before the seizure's electrographic onset with consistency (see Fig. 3.5b). Although recurrent, large amplitude negative deflecting FP values were observed before seizure onset it was deduced that their temporal sequence pre-ictally was not a general phenomenon as revealed by their disappearance upon averaging. Overall, use of aFP is endorsed when attempting to quantify electrographic signal changes leading to seizure. For depth electrode recordings FP/aFP quantifiers were able to detect electrographic changes ~ 29 ± 13 s (avg:stdev) in anticipation of electrographic

onset (see Fig. 3.6). The anticipation period is notably shorter than the case for slice recordings. Most of the complete EEG recordings were obtained from P1 who has an active interictal seizure disorder causing FP/aFP values to be elevated only by large deviation from an already active baseline. Aside from the methodology, distinction between interictal and pre-ictal states in human EEG recordings is challenging mainly due heterogeneity across patient-specific electrographic seizure patterns and lack of current understanding of the pre-ictal state (Litt and Lehnertz, 2002).

Overall, this methodology is inherently simple without a requirement of knowledge about specific signal characteristics and no templates. Computationally, it can be performed relatively quickly and can easily be adapted for real-time implementation. In that scenario, a continuous data stream would be buffered with a small lag, where 'locally optimized' peak detection would be performed for that data segment in real-time with direct visualization and FP/aFP mapping. The system would have to monitor a few seizure epochs in order to tune the parameters involved (e.g. FP surface, k) and obtain a practical approximation to a threshold for FP and aFP quantifiers for ictal states. Prolonged, frequent, large amplitude values of FP (negative) and aFP quantifiers above a determined threshold would serve to anticipate seizures (see Figs. 3.3 and 3.5). Robustness of this implementation is exemplified by the observation that small variations in detection and mapping parameters do not translate into vastly different results.

RPT method does suffer from a few constraints. Its main limitation is a reliance on the existence of 'viable' peaks with amplitudes above the noise level. This is not as much of concern for *in vitro* cellular and extracellular recordings as it is in the case of EEG recordings. Not all epileptic patients display frequent 'spikes' in advance of electrographic seizures and there exists great heterogeneity of interictal activity amongst patients. In the case of EEG, intracranial recordings are typically required to provide adequate signal-to-noise characteristics and minimal artefacts (e.g. movement, etc.). Nevertheless, many of today's powerful filtering and signal processing algorithms can be utilized to enhance/de-noise signals (e.g. scalp recordings) so that they may be used for direct input into this form of analysis. Like all time-series techniques, care must be taken in order to extract meaningful results, which usually requires one to have a clear

understanding of the limitations of both data and analyses. IPI recursive plots in conjunction with nonlinear theory for recursive maps offer a simple and robust method for the characterization of dynamical regimes. The theory and direct application of nonlinear trend-fitting and trajectory identification for 2D recursive plots (modestly addressed in this report) are well represented in several excellent sources (Guckenheimer and Holmes, 1983; Berge *et al.*, 1984; Eckmann *et al.*, 1987; Ott *et al.*, 1990; Christini and Collins, 1997; Garfinkel *et al.*, 1992; Shinbrot *et al.*, 1993; Schiff *et al.*, 1994; Perez Velazquez *et al.*, 1999).

We present RPT analysis as a concise method suitable for the analysis of electrophysiological recordings in the context of seizures. The analysis procedure and subsequent visualization tactics are able to extract meaningful information about temporal relations in time-series data. It is important to emphasize that the visualization technique, FP and aFP, are arbitrary quantifiers reflecting the state-space compactness of time-depended trajectories in a projected space. The demonstrated purpose of RTP is the ability to detect electrographic signal changes using simple rules for peak-detection, coupled to straightforward visualization strategies. Further, repeatable return-plots generated by the quantitative signal-based detection parameters can be used for input to other established nonlinear time-series measures (e.g. correlation dimension, entropy, state-space eigen analysis, etc.). RPT is simple yet robust in quantitatively detecting electrographic signal changes, which make it useful for real-time implementation in clinical and research environments.

4.2 Dynamics of the Transition to SLEs & Period Forcing for its Aversion

We have used an in vitro model of status epilepticus (Rafiq *et al.*, 1993, 1995), to gain insight into the dynamics of the transition to seizure and used the system's own dynamics to stop seizure generation. The dynamical regimes derived from the IPI recursive, or first-return, plots, suggest that the spontaneous activity in these slices exhibits several steady states. Two of these are most prominent, one representing periodic, or limit-cycle, behaviour at relatively low frequencies, during interictal activity. The other represents high-frequency hypersynchronous firing that marks the start of the SLE. Periodic forcing by short-duration electrical perturbations arrested the transition to the SLE by stabilizing the interictal-like firing pattern.

The self-sustained epileptiform activity in this in vitro model resembles human status epilepticus. Charateristic of status epilepticus is the short interval between recurrent ictal events, and the transition from simple to complex epileptiform discharges preceding the seizure onset, phenomena observed in this in vitro slice model (see also Rafiq *et al.*, 1995). However, because the slice obviously simplifies the whole cortical-limbic neuronal circuitry involved in epileptic patients, the in vitro observations have to be interpreted with caution.

As opposed to model-based classical feedback control methods (Wiener, 1961), which require a detailed analytical model of the system under study, in model-independent chaos control techniques one studies the nonlinear dynamical structure and then uses this knowledge to develop ways of directing the system's activity towards the desired state by acting on a variable. The lack of a requirement for accurate analytical models of the systems under control has obvious advantages, since they are difficult to develop for complex biological phenomena. Model-independent chaos control methods (Ott *et al.*, 1990) have been applied to alter the behaviour of physical (Shinbrot *et al.*, 1993) and physiological (Christini and Collins, 1996, 1997; Christini *et al.*, 2001; Garfinkel *et al.*, 1992; Schiff *et al.*, 1994; Hall *et al.*, 1997) complex systems. Variants of these methods have been designed to stabilize flip-saddle unstable fixed points (Christini and Collins, 1997b). Our modest goal in this study was to stabilize one possible unstable (or

meta-stable) steady state of the system, while ignoring the complex stable or unstable manifold calculations needed in other control paradigms (Ott *et al.*, 1990). Hence, by empirical study of the effects of the perturbations near the desired steady state (in our case the frequency of bursting that is present during interictal activity) we attempted to stabilize what can be considered a periodic orbit of the possibly complex (chaotic?) attractor for the ensemble activity.

We assume that the time series of spikes (peaks) is an expression of the process that governs network activity (Sauer, 1994). Therefore the study of IPI plots provides insights into population dynamics, as has been shown for studies of the dynamics of electroreceptor activity in fish (Braun *et al.*, 1997), in mammalian brain (Schiff *et al.*, 1994; Di Mascio *et al.*, 1999) and in cardiac tissue (Christini and Collins, 1996; Garfinkel *et al.*, 1992; Christini and Collins, 1997). The IPI scatter plot corresponding to the transition from pre-ictal to ictal activity has structure (e.g. is not space-filling), which is indicative of chaos or low-dimensional dynamics, as shown in other physiological systems (Garfinkel *et al.*, 1996; Braun *et al.*, 1997). However, determination of chaotic dynamics from time series is a controversial issue (Rapp, 1994) and was not the purpose of our study. By approximating the first-return plot to an algebraic equation, the one-dimensional map, one can obtain further quantitative insights into the dynamical regimes as these maps represent the essential dynamic properties. This is a common method that has been applied to a large number of physical, chemical (Roux, 1983) and biological systems (Glass *et al.*, 1983; Berge *et al.*, 1984; Perez Velazquez *et al.*, 1999). The dissipative nature of brain activity justifies the use of one-dimensional maps. An interesting practical application of these maps has been shown recently in the control of cardiac arrhythmia in humans using an adaptive nonlinear control method (Christini *et al.*, 2001). Dynamical characteristics are extracted from the geometry of the fixed points (i.e. steady states) in these maps, as proposed by other investigators (Kelso & Fuchs, 1995), which then can be analyzed for their stability and bifurcation characteristics. We find that flip, or sub-harmonic, bifurcations occur in human seizures (Perez Velazquez *et al.*, 1999) and in the in vitro slice preparation shown here. Bifurcations are conceptualized as qualitative changes in the system's dynamics (Hoppensteadt & Izhikevich, 1997; Titcombe *et al.*, 2001). Specifically, the unravelling of the possible

bifurcations that take place in epileptiform activity may add fruitful insights to understand (and control) the transition from interictal to ictal activity (Lopes da Silva & Pijn, 1999).

In general, to stop seizure occurrence we must know where, how, and when to apply the perturbation. In our experiments, the location of the stimulating electrode was chosen to be the mossy fibres based on previous observations that the CA3 neurons pace the interictal firing, leading to the recruitment of more cells that bring about the SLE (Perez Velazquez and Carlen, 1999). Low frequency forcing was selected by inspection of the activity in slices with no spontaneous SLEs (see Fig. 3.7), suggesting the presence of an interictal-like stable state. The timing of the perturbation was inferred from the proximity to the low-frequency interictal-like firing stable state (see Fig. 3.12). When the system is close to that steady state (or near the stable manifold for the fixed point, in dynamical language) our perturbation effectively forces the system to stabilize into that low-frequency state, aborting its transition to the hypersynchronous high-frequency seizure. Periodic forcing can link weakly coupled oscillators (Hoppensteadt and Izhikevich, 1997), and many brain areas are periodically or stochastically forced (septum-hippocampus, thalamus-cortex). In support of our observations we note that evidence exists that low-frequency electrical stimulation (1 Hz) inhibits the development of amygdala kindled seizures in rats (Weiss *et al.*, 1995; Velisek *et al.*, 2002), and low-frequency transcranial magnetic stimulation (0.33 Hz) also alleviates seizure disorders in human patients (Tergau *et al.*, 1999). Also using in vitro preparations, low-frequency periodic pacing stimulation has been shown to suppress the tonic phase of SLE generation in the high-potassium seizure model (Jerger & Schiff, 1995), and in the 4-aminopyridine seizure-like model (Barbarosie & Avoli, 1997). However, it is possible that, in other seizure models, different stimulation paradigms are effective, as demonstrated in the suppression of epileptiform events by high-frequency sinusoidal fields in hippocampal slices bathed in low-calcium or in the presence of picrotoxin (Bikson *et al.*, 2001). Adaptive electric fields have also been successfully applied to induce or ameliorate seizure-like events in the hippocampal slice (Gluckman *et al.*, 2001).

Our electrical perturbations and the collective phenomena here reported should be reflected at the cellular level. A possible cellular mechanisms that could account for the halting of the SLEs following short periodic forcing is the phenomenon of synaptic depression. However, our successful perturbations were too short (20-50 seconds) to induce depression of synaptic responses, for which longer times are needed, for example 1Hz for 15 minutes (Chen *et al.*, 2001). The investigation of these more specific mechanisms was not the purpose of our study.
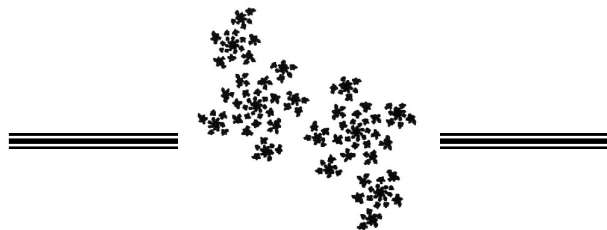
Our results provide a framework to understand the dynamics of the transition to seizure and for the possible control of this progression and may shed light on possible dynamical mechanisms for the activity of neuronal circuits, specifically transient stabilization of metastable states (Lopes da Silva and Pijn, 1999). A set of coupled nonlinear oscillators has an infinite number of ways of performing, but within certain conditions it tends to stabilize into specific states of activity (attractor), and remains there until perturbed. Switching from one to another attractor is called a bifurcation, which requires a parametric change in the system. Our study does not point directly to specific cellular or molecular targets, altered by the perturbations, that may be involved in the transition to seizures. We submit the idea that the epileptic brain, while may be displaying complex dynamics (e.g. chaotic) during non-seizure epochs, can stabilize transiently into a variety of meta-stable periodic orbits, which exist as part of the dynamical repertoire in the system's attractor. The particular sequence of orbits or transitions therein can achieve intermittent stability through intrinsic mechanisms (e.g. population synchronization, Rafiq *et al.*, 1993,1995; Perez Velazquez and Carlen, 1999) or via an external perturbation as we have illustrated.

The transient synchronous stabilization of unstable states is a concept that has also been inferred from experiments using sympathetic neuronal networks possessing many metastable states (Chang et al, 2000), where transient phase-lock states become stable at the population level. These metastable states in the neuronal population are achieved through linear and nonlinear interactions. These investigators propose that this metastability affords a variety of the network responses to distinct stimuli. During dynamical regimes governed by intermittency, transient stabilization of several metastable states occurs without the need of strong external stimuli. Indeed, transitions

to periodic behaviour (such as that found during seziures) are often realized via intermittency in chemical and physical systems (Kiss and Hudson, 2001). Hence, we propose that similar transitions via intermittency are involved in the generation and termination of seizures. The notion that electrical stimulation changes the stability of brain oscillations has also support in other studies where deep brain stimulation is used to treat Parkinsonian tremor, specifically the network dynamics were found to change via a Hopf bifurcation (Titcombe *et al.*, 2001). As opposed to equilibrium dynamics where functions (such as free energy, entropy) can be optimized, in non-equilibrium systems (such as the brain) a fundamental concept is the stability of discrete steady states. We propose that, in some simple cases such as the brain slice preparation shown here, it is possible to take advantage of this idea and alter the stability of specific steady states. The use of nonlinear analyses provides additional insights that classical time-series analyses are incapable of providing since the tend not to be sensitive to nonlinear temporal trends (Kantz & Schreiber, 1997). Application of linear methods to signals generated by nonlinear systems may result in spurious conclusions; such as a time-series may appear random (noise-like) when indeed determinism is present (Vandenhouten *et al.*, 2000).

In general, Fourier decomposition and similar methods are not adequate to reveal, for example, chaotic dynamics, and the exact nature of the bifurcations and stability of fixed points is much harder to grasp by looking at power spectra, for example. The simple IPI plots used here provide a more dynamic view and can be exploited to uncover specific dynamical regimes and the nature of dynamical bifurcations, by detailed analysis of the mapping function (Perez Velazquez *et al.*, 2001).

While it was shown several decades ago that brainstem stimulation can alter the rhythms of the cortical EEG (Moruzzi and Magoun, 1949), the possibility that seizures can be arrested by electrical stimulation has been explored *in vivo* only in the case of vagus nerve stimulation (Takaya *et al.*, 1996), deep brain stimulation (Velasco *et al.*,1995), and recently, trigeminal nerve stimulation (Fanselow *et al.*, 2000). In conclusion, our work indicates that direct electrical perturbation, with proper spatio-temporal application in the area where seizures are being generated, can abort the onset of SLEs. These methods, coupled to seizure-predicting algorithms (Elger and Lehnertz, 1998; Jerger *et al.,* 2001; Litt *et al.,* 2001), may provide a framework for the development of automated devices capable of halting the transition to seizures in patients with intractable epilepsy.

Bibliography

1. Abarbanel H.D.I., Frison T.W., Tsimring L.S. Obtaining order in a world of chaos: Time-domain analysis of nonlinear and chaotic signals. IEEE Sig. Proc. Mag. 1998. May:49-65.

2. Aitken P.G., Sauer T, Schiff S.J. Looking for chaos in brain slices. J Neurosci Methods. 1995. Jun;59(1):41-8.

3. Akay M., Nonlinear Biomedical Signal Processing: Volume II. IEEE Press, 2000.

4. Babloyantz A., Destexhe A. Low-dimensional chaos in an instance of epilepsy. Neurobiol 1986. 83:3513-3517.

5. Barbarosie, M., Avoli M. CA3-driven hippocampal-entorhinal loop controls rather than sustains in vitro limbic seizures. J Neurosci. 1997. 17: 9308-9314.

6. Bardakjian B., Courville A. Chaosmakers: Rhythm breakers, Proc. ICSC Symp. On Neural Computation (NC'2000) 2000. No. 1402, pp. 121i-v.

7. Benabid A.L., Koudsie A., Pollak P., Kahane P., Chabardes S., Hirsch E., Marescaux C., Benazzouz A. Future prospects of brain stimulation. Neuro. Res. 2000. 22: (3) 237-246.

8. Bergé P., Pomeau Y., Vidal C. Order within chaos: towards a deterministic approach to turbulence. John Wiley & Sons, New York. 1984.

9. Bikson M., J. Lian P.J., Hahn W.C., Stacey C., Sciortino S., Durand D.M. Suppression of epileptiform activity by high frequency sinusoidal fields in rat hippocampal slices. J Neurophysiol. 2001. 53:181-191.

10. Braun H.A., Schafer K., Voigt K., Peters R.,Bretschneider F., Pei X., Wilkens L., Moss F. Low-dimensional dynamics in sensory biology 1: thermally sensitive electroreceptors of the catfish. J. Computational Neurosci. 1997. 4:335-347.

11. Casdagli M.C., Iasemidis L.D., Savit R.S., Gilmore R.L., Roper S.N., Sackellares J.C. Non-linearity in invasive EEG recordings from patients with temporal lobe epilepsy. Electroencephalogr Clin Neurophysiol. 1997 Feb;102(2):98-105.

12. Castro R., Sauer T. Correlation dimension of attractors through interspike intervals. Phys Rev E. 1997. 55(1):287-290.

13. Chang H.S., Staras K., Gilbey M.P. Multiple oscillators provide metastability in rhythm generation. J. Neurosci. 2000. 20: 5135-5143.

14. Chen Y.L., Huang C-C, Hsu K-S. Time-dependent reversal of long-term potentiation by low-frequency stimulation at the hippocampla mossy fibre-CA3 synapses. J. Neurosci. 2001. 21:3705-3714

15. Christini D.J. Collins J.J. Real-time, adaptive, model-independent control of low-dimensional chaotic and nonchaotic dynamical systems. IEEE Trans Circ Sys 1997. 44(10):1027-1030.

16. Christini D.J., Collins J.J. Control of chaos in excitable physiological systems: a geometric analysis. Chaos. 1997. 7:544-549.

17. Christini D.J., Collins J.J. Using chaos control and tacking to suppress a pathological nonchaotic rhythm in a cardiac model. Phys. Rev. E. 1996. 53:R49-R52.

18. Christini D.J., Stein K.M., Markowitz S.M., Mittal S., Slotwiner D.J., Scheiner M.A., Iwai S., Lerman B.B. Nonlinear-dynamical arrhythmia control in humans. Proc. Natl. Acad. Sci. 2001. 98: 5827-32.

19. Da Silva F.H, Pijn J.P. Epilepsy as a dynamic disease of brain systems. Adv Neurol. 1999. 81:97-104.

20. Decroly O., Goldbeter A. From simple to complex oscillatory behaviour: analysis of bursting in a multiply regulated biochemical system. J. Theor. Biol. 1987. 124: 219-250.

21. Di Mascio M., Di Giovanni G., Di Matteo V., Esposito E. Reduced chaos of interspike interval of midbrain dopaminergic neurons in aged rats. Neurosci. 1999. 89: 1003-1008.

22. Ditto W.L., Spano M.L., Lindner J.F. Techniques for the control of chaos. Physica D. 1995. 86:198-211.

23. Dreier J.P., Heinemann U. Regional and time dependent variations of low Mg2+ induced epileptiform activity in rat temporal cortex slices. Exp Brain Res 1991. 87(3):581-596.

24. Eckmann J.P., Olifson Kamphort S., Ruelle D. Recurrence plots of dynamical systems. Europhys Lett 1987. 4:973.

25. Elbert T., Ray W.J., Kowalik Z.J., Skinner J.E., Graf K.E., Birbaumer N. Chaos and physiology: deterministic chaos in excitable cell assemblies. Physiol. Rev. 1994. 74:1-47.

26. Elger C.E., Lehnertz K. Seizure prediction by non-linear time series analysis of brain electrical activity. Euro. J. Neurosci 1998;10:786-789.

27. Faber D.S, Korn H. Electrical field effects: their relevance in central neural networks. Phys Rev 1989. 69(3):821-863.

28. Fanselow E.E., Reid A.P., Nicolelis M.A.L. Reduction of pentylenetetrazole-induced seizure activity in awake rats by seizure-triggered trigeminal nerve stimulation. J. Neurosci. 2000. 20: 8160-8168.

29. Franaszczuk P.J., Bergey G.K., Durka P.J., Eisenberg H.M. Time-frequency analysis using the matching pursuit algorithm applied to seizures originating from the mesial temporal lobe. Electroenceph. Clin. Neurophysiol 1998. 106: 513-521.

30. Gabor A.J., Leach R.R., Dowla F.U. Automated seizure detection using a self-organizing neural network. Electroenceph. Clin. Neurophysiol. 1996. 99:257-266.

31. Garfinkel A., Spano M.L., Ditto W.L., Weiss J.N. Controlling cardiac chaos. Science 1992. 257:1230-1235.

32. Glass L., Guevara M.R., Shrier A. Bifurcation and chaos in a periodically stimulated cardiac oscillator. Physica D. 1983. 7:89-101.

33. Gluckman B.J., Nguyen H., Weinstein S.L., Schiff S.J. Adaptive electric field control of epileptic seizures. J. Neurosci. 2001. 21:590-600.

34. Gong Y., Xu J., Ren W., Hu S., Wang F. Determining the degree of chaos from analysis of ISI time series in the nervous system: a comparison between correlation dimension and nonlinear forecasting methods. Biol Cybern. 1998. Feb;78(2):159-65.

35. Gotman J. Automatic detection of seizures and spikes. J Clin Neurophysiol 1999. 16(2):130-140.

36. Gotman J. Automatic recognition of epileptic seizures in the EEG. Electroenceph Clin Neurophysiol 1982. 54:530-540.

37. Guberman A., Bruni J. Essentials of clinical epilepsy. Butterworth-Heinemann. 1999.

38. Guckenheimer J., Holmes P. Nonlinear oscillations, dynamical systems, and bifurcations of vector fields. Springer, New York. 1983.

39. Hall K., Christini D.J., Tremblay M., Collins J.J., Glass L., Billette J. Dynamic control of cardiac alternans. Phys. Rev. Lett. 1997. 78:4518-4521.

40. Hallet M. Transcranial magnetic stimulation and the human brain, Nature. 2000; 406:147-150.

41. Holmgren R.A. A first course in discrete dynamical systems. Springer, 1996.

42. Hoppensteadt F.C., Izhikevich E.M. Weakly Connected Neural Networks. J.E. Marsden, L. Sirovich and F. John, editor. Applied Mathematical Sciences, volume 126, Springer. 1997.

43. Hoyer D., Bauer R., Conrad K., Galicki M., Doring A., Hoyer H., Walter B., Witte H., Zwiener U. Specific monitoring of neonatal brain function with optimized frequency bands. IEEE Eng. Med. Biol. Mag. 2001. Sep-Oct;20(5):40-6.

44. Iasemidis L.D., Sackellares .JC., Zaveri H.P., Williams W.J. Phase space topography and the Lyapunov exponent of electrocorticograms in partial seizures. Brain Topogr. 1990 Spring;2(3):187-201.

45. Iasemidis L.D., Sackellares C.J. Chaos theory and epilepsy. The Neuroscientist 1996. 118-126.

46. Jefferys J.G., Borck C., Mellanby J. Chronic focal epilepsy induced by intracerebral tetanus toxin. J. Ital. J. Neurol. Sci. 1995. Feb-Mar;16(1-2):27-32.

47. Jerger K.K., Schiff S.J. Periodic pacing an in vitro epileptic focus. J. Neurophysiol. 1995. 73:876-879.

48. Kant H., Schreiber T. Nonlinear time series analysis. Cambridge University Press: New York, 1997.

49. Kelso J.A.S., Fuchs A. Self-organizing dynamics of the human brain: critical instabilities and Silnikov chaos. Chaos. 1995. 5:64-69.

50. Kennel M.B., Brown R., Abarbanel H.D.I. Determining minimum embedding dimension using a geometrical construction. Phys. Rev. 1992. 45:3403-3411.

51. Kiss I.Z., J.L. Hudson. Phase synchronization and suppression of chaos through intermittency in forcing of an electrochemical oscillator. Phys. Rev. E. 2001. 64:1-8.

52. Kugiumtzis D., Lillekjendlie B., Christophersen N.. Chaotic time series part I: Estimation of some invariant properties in state space. Modeling, Identification and Control. 1994. 15(4):205 -- 224.

53. Le Van Quyen M., Martinerie J., Navarro V., Baulac M., Varela F. Characterizing neurodynamic changes before seizures. J. Clin. Neurophys. 2001. 18(3):191-208.

54. Le Van Quyen M., Martinieri J., Adam C., Varela F.J. Unstable periodic orbits in human epileptic activity. Physical Rev. E. 1997. 56:3401-3410.

55. Lehnertz K. Non-linear time series analysis of intracranial EEG recordings in patients with epilepsy--an overview. Int J Psychophysiol. 1999. Oct;34(1):45-52.

56. Lehnertz K., Elger C.E. Can epileptic seizures be predicted? Evidence from nonlinear time series analysis of brain electrical activity. Phys. Rev. Lett. 1998. 80(22):5019-5022.

57. Lehnertz K., Elger C.E. Spatio-temporal dynamics of the primary epileptogenic area in temporal lobe epilepsy characterized by neural complexity loss. Electroencephalogr. Clin. Neurophysiol. 1995. 95:108-117.

58. Lian J., Shuai J., Hahn P., Durand D.M. Nonlinear dynamic properties of low calcium-induced epileptiform activity. Brain Res. 2001. Feb 2;890(2):246-54.

59. Litt B., Esteller R., Echauz J., D'Alessandro M., Shor R., Henry T., Pennell P., Epstein C., Bakay R., Dichter M., Vachtsevanos G. Epileptic seizures may begin hours in advance of clinical onset: a report of five patients. Neuron. 2001. Apr;30(1):51-64.

60. Litt B., Lehnertz K. Seizure prediction and the preseizure period. Curr Opin Neurol. 2002. Apr;15(2):173-7.

61. Lopes da Silva F.H., Pijn, J.P.M. Epilepsy as a dynamic disease of brain systems. Advances in Neurology. 1999. 81:97-104.

62. Mañé R. On the dimension of the compact invariant set of certain nonlinear maps, Lecture notes in mathematics Vol. 898, p. 230-242. Springer-Verlag: New York, 1981.

63. Martinerie J., Adam C., Le Van Quyen M., Baulac M., Clemenceau S., Renault B., Varela F.J. Epileptic seizures can be anticipated by non-linear time analysis Nature Med. 1998. 4(10):1173-1176.

64. McNamara J.O. Cellular and molecular basis of epilepsy. J. Neurosci. 1994. 14:3413-3425.

65. McNamara J.O. Emerging insights into the genesis of epilepsy. Nature 1999. 399:A15-A22.

66. Miller R. Time and the Brain. Harwood Academic Publishers: Amsterdam, 2000.

67. Moruzzi G., Magoun H.W. Brainstem reticular formation and activation of the EEG. Electroencephalogr. Clin. Neurophysiol. 1949. **1**:455-473.

68. Osorio I., Frei M.G., Wilkinson S.B. Real-time automated detection and quantitative analysis of seizures and short-term prediction of clinical onset. Epilepsia 1998. 39(6):615-627.

69. Ott E., Grebogi C., Yorke J.A. Controlling chaos. Phys. Rev. Lett. 1990. 64(11):1196-1199.

70. Packard N.H., Crutchfield J.P., Farmer J.D., Shaw R.S. Geometry from time series. Phys. Rev. Lett. 1980. 45:712-716.

71. Palus M. Nonlinearity in normal human EEG: cycles, temporal asymmetry, nonstrationarity and randomness, not chaos. Biol. Cybern 1996. 75(5):389-96.

72. Pauri F., Pierelli F., Chatrian G-E., Erdly W.W. Long-term EEG-video-audio monitoring: computer detection of focal EEG seizure patterns. Electroenceph. Clin. Neurophysiol. 1992. 82:1-9.

73. Perez Velazquez J.L., Khosravani H., Lozano A., Bardakjian B.L, Carlen P.L, Wennberg R. Type III intermittency in human partial epilepsy. Euro. J. Neurosci. 1999. 11:2571-2576.

74. Perez Velazquez, J.L. and P.L. Carlen. Synchronization of GABAergic interneuronal networks in seizure-like activity in the rat entorhinal-hippocampal slice. Eur. J. Neurosci. 1999. 11:4110-4118.

75. Perez Velazquez, J.L., Khosravani H., Cortez M.A., Carlen P.L., Snead III O.C., Wennberg R. The transition in and out of the seizure: a nonlinear dynamical approach. Epilepsia. 2001. 42 (suppl.)7:116.

76. Petrosian A., Prokhorov D., Homan R., Dasheiff R., Wunsch D. (II), Recurrent neural network based prediction of epileptic seizures in intra- and extracranial EEG. Neurocomputing. Volume: 30, Issue: 1-4, January, 2000, pp. 201-218.

77. Pijn J.P., Neerven J.V., Noest A., Lopes da Silva F.H. Chaos or noise in EEG signals: dependance on state and brain site. Electroenceph. Clin. Neurophysiol 1991. 79:371-381.

78. Pijn J.P., Velis D.N., van der Heyden M.J., DeGoede J., van Veelen W.M., Lopes da Silva F.H. Nonlinear dynamics of epileptic seizures on basis of intracranial EEG recordings. Brain topography 1997. 9(4):249-270.

79. Pijn, J.P., van Neerven J., Noest A., Lopes da Silva F.H. 1991. Chaos or noise in EEG signals: dependence on state and brain site. Electroencephalogr. Clin. Neurophysiol. 79:371-381.

80. Press W.H., Teukolsky S.A., Vetterling W.T., Flannery B.P. Numerical recipes in fortran 77 (2edn). Cambridge University Press : Massachusetts, 1997.

81. Qin D. A comparison of techniques for the prediction of epileptic seizures. In Eighth IEEE symposium on Computer-Based Medical Systems (Lubbock, TX: IEEE Computer Society Press). 1995. 151-157.

82. Qu H., Gotman J. A patient-specific algorithm for the detection of seizure onset in long-term EEG monitoring: possible use as a warning device. IEEE Trans. Biomed. Eng. 1997. 44(2):115-122.

83. Rafiq A., DeLorenzo R.J., Coulter D.A. Generation and propagation of epileptiform discharges in a combined entorhinal cortex/hippocampal slice. J. Neurophys. 1993. 70(5):1962-1974.

84. Rafiq A., Zhang Y., DeLorenzo R.J., Coulter D.A. Long-duration self-sustained epileptiform activity in the hippocampal-parahippocampal slice: a model of status epilepticus. J Neurophys 1995. 74(5):2028-2042.

85. Rapp, P.E. A guide to dynamical analysis. Integrative Physiol. Behav. Sci. 1994. 29:3111-327.

86. Roux, J-C. Experimental studies of bifurcations leading to chaos in the Belousof-Zhabotinsky reaction. Physica D. 1983. 7: 57-68.

87. Sauer T. Interspike interval embedding of chaotic signals. Chaos 1995. 5, 127.

88. Sauer, T. Reconstruction of dynamical systems from interspike intervals. Phys. Rev. Lett. 1994. 72:3811-3814.

89. Schiff S.J., Jerger K., Duong D.H., Chang T., Spano M.L., Ditto W.L.. Controlling chaos in the brain. Nature 1994. 370(25):615-620.

90. Shinbrot T., Grebogi C., Ott E., Yorke J.A. Using small perturbations to control chaos. Nature 1993. 363:411-417.

91. Slutzky M.W., Cvitanovic P., Mogul D.J. Deterministic chaos and noise in three in vitro hippocampal models of epilepsy. Ann. Biomed. Eng. 2001. 29(7):607-18.

92. Steriade M., The intact and sliced brain. MIT Press. Massachusetts, 2001.

93. Takahiro T., Inaba N., Miyamichi J. Mechanisms for taming chaos by weak harmonic perturbations. Phys. Rev. Lett. 1999. 83:3824-3827.

94. Takaya M., Terry W.J., Naritoku D.K. Vagus nerve stimulation induces a sustained anticonvulsant effect. Epilepsia 1996. 37:1111-1116.

95. Takens F. Detecting strange attactors in turbulence, Lecture notes in mathematics Vol. 898 366-381. Springer-Verlag: New York, 1981.

96. Tergan F. Low frequency repetitive transcranial magnetic stimulation improves intractable epilepsy. The Lancet 1999. 353:2209-2210.

97. Tergau F., Naumann U., Paulus W., Steinhoff B.J. Low-frequency repetitive transcranial magnetic stimulation improves intractable epilepsy. The Lancet. 1999. 353:2209-2210.

98. Theiler J., Rapp P.E. Re-examination of the evidence for low-dimensional, nonlinear structure in the human electroencephalogram. Electroenceph. Clin. Neurophysiol 1996. 98:213-222.

99. Titcombe M.S., Glass L., Guehl D., Beuter A. Dynamics of Parkinsonian tremor during deep brain stimulation. Chaos. 2001. 11: 766-773.

100. Vandenhouten R., M. Lamberts, Langhorst P., Grebe R. Nonstationary time-series analysis applied to the investigation of brainstem system dynamics. IEEE Trans. Biomed. Eng. 2000. 47:729-737.

101. Velasco F., Velasco M., Velasco A.L., Marquez I., Jimenez F., Marquez I., Rise M. Electrical stimulation of the centromedian thalamic nucleus in control of seizures: long-term studies. Epilepsia. 1995. 36 : 63-71.

102. Webber W.R.S., Lesser R.P., Richardson R.T., Wilson K. An approach to seizure detection using an artificial neural network (ANN). Electroenceph Clin Neurophysiol 1996. 98:250-272.

103. Weiss S.R.B., Li X-L., Rosen J.B., Li H., Heynen T., Post R.M Quenching; inhibition of development and expression of amygdala kindled seizures with low frequency stimulation. Neuroreport. 1995. pp. 2171-2176.

104. Wiener N. Cybernetics. Cambridge, Massachusetts. MIT Press. 1961.

105. Winfree A.T. When time breaks down: the three dimensional dynamics of electrochemical waves and cardiac arrhythmias. Princeton University Press. 1987.